Forschungsbericht 2023-14

Climate Impact of Contrail Cirrus

Marius Bickel

Deutsches Zentrum für Luft- und Raumfahrt
Institut für Physik der Atmosphäre
Oberpfaffenhofen

Dissertation
an der Fakultät für Physik
der Ludwig-Maximilians-Universität
München

Deutsches Zentrum
DLR für Luft- und Raumfahrt

Forschungsbericht 2023-14

Climate Impact of Contrail Cirrus

Marius Bickel

Deutsches Zentrum für Luft- und Raumfahrt
Institut für Physik der Atmosphäre
Oberpfaffenhofen

Dissertation an der
Fakultät für Physik
der Ludwig-Maximilians-Universität
München

133 Seiten
31 Bilder
9 Tabellen
183 Literaturstellen

Deutsches Zentrum
DLR für Luft- und Raumfahrt

Herausgeber:

Deutsches Zentrum
für Luft- und Raumfahrt e. V.
Wissenschaftliche Information
Linder Höhe
D-51147 Köln

ISSN 1434-8454
ISRN DLR-FB-2023-14
Erscheinungsjahr 2023

DOI: 10.57676/mzmg-r403

Kondensstreifen-Zirren, Klimawirkung, Strahlungsantrieb, Bodentemperaturänderung, Rückkopplungen

(Veröffentlicht in Englisch)

Marius BICKEL
DLR, Institut für Physik der Atmosphäre, Oberpfaffenhofen

Klimawirkung von Kondensstreifen-Zirren

Dissertation, Ludwig-Maximilians-Universität, München

Kondensstreifen-Zirren beeinflussen durch ihre physikalischen und optischen Eigenschaften sowohl die Atmosphäre als auch den Strahlungshaushalt der Erde und tragen damit zur globalen Erwärmung bei. Im Rahmen dieser Dissertation wurde die Klimawirkung von Kondensstreifen-Zirren mit Hilfe globaler Klimamodellsimulationen durch die Bestimmung von konventionellen und effektiven Strahlungsantrieben und die dadurch induzierte Bodentemperaturänderung quantifiziert. Um ein besseres Verständnis der verschiedenen physikalischen Prozesse zu erlangen, welche zur Bodentemperaturänderung beitragen, wurden mittels der Methode der Feedbackanalyse sowohl die schnellen als auch die langsamen Strahlungsrückkopplungen bestimmt. Als Ursache der im Vergleich zu einem CO_2-Strahlungsantrieb deutlich verminderten Klimawirkungseffizienz von Kondensstreifen-Zirren (im Hinblick auf die bodennahe Erwärmung) konnten damit die dafür verantwortlichen Rückkopplungen, als Konsequenz auf unterschiedliche Reaktionen der natürlichen Wolken, bestimmt werden.

Contrail cirrus, climate impact, radiative forcing, surface temperature change, feedbacks

(Published in English)

Marius BICKEL
German Aerospace Center (DLR), Institute of Atmospheric Physics, Oberpfaffenhofen

Climate Impact of Contrail Cirrus

Doctoral Thesis, Ludwig-Maximilians-Universität, München

Contrail cirrus affect the Earth's atmosphere and radiation budget through their physical and optical properties, and thus contribute to global warming. In the present thesis, the climate impact of contrail cirrus was quantified using global climate model simulations by determining conventional and effective radiative forcings and the hereby induced surface temperature change. To improve the understanding of the different physical processes contributing to the surface temperature change, both rapid radiative adjustments and slow feedbacks were determined using the feedback analysis method. As the origin of a – in comparison to CO_2 forcing – considerably reduced climate efficacy of contrail cirrus to warm the Earth's surface, differently acting natural cloud responses were identified to be the mainly responsible feedback mechanism.

Climate Impact of Contrail Cirrus

Marius Bickel

München 2023

Climate Impact of Contrail Cirrus

Dissertation
an der Fakultät für Physik
der Ludwig–Maximilians–Universität
München

vorgelegt von
Marius Bickel
aus Weißenburg

München, Mai 2023

Erstgutachter: Prof. Dr. Robert Sausen
Zweitgutachter: Prof. Dr. Mark Wenig
Tag der Abgabe: 3. Mai 2023
Tag der mündlichen Prüfung: 3. Juli 2023

Kurzfassung

Der Luftverkehr ist in den letzten Jahrzehnten exponentiell angewachsen und spielt deshalb eine wichtige Rolle in der Diskussion über zukünftige Strategien zur Reduzierung von Klimaänderungen. Basierend auf Strahlungsantrieben liefern Kondensstreifen-Zirren vermutlich den größten Beitrag zur Klimawirkung des Luftverkehrs und übertreffen damit die CO_2 Emissionen des Luftverkehrs. Während frühere Studien eine verringerte Wirksamkeit von linearen Kondensstreifen auf die Änderung der mittleren globalen Erdoberflächentemperatur gezeigt haben, wurde dies für die weitaus wichtigeren Kondensstreifen-Zirren noch nicht untersucht.

Im Rahmen der vorliegenden Arbeit wurden zahlreiche Klimamodellsimulationen durchgeführt, um ein besseres Verständnis über die Klimawirkung von Kondensstreifen-Zirren zu erlangen. Die Simulationen wurden mit den ECHAM5- und EMAC-Klimamodellen durchgeführt, welche mit einer Kondensstreifen-Zirren Parametrisierung nach dem neusten Stand der Wissenschaft ausgestattet sind. Die Simulationen wurden weitergehend mittels Rückkopplungsanalyse, nach der "partial radiative perturbation"Methode, untersucht um die physikalischen Ursachen der Temperaturänderung zu verstehen.

Zunächst wurde die Klimawirkung von Kondensstreifen-Zirren auf der Grundlage von Strahlungsantrieben bewertet, welche durch Simulationen mit fixierter Meeresoberflächentemperatur bestimmt wurden. Es konnte gezeigt werden, dass der effektive Strahlungsantrieb von Kondensstreifen-Zirren, im Vergleich zu den klassischen Strahlungsantrieben, deutlich reduziert ist. Im Gegensatz dazu weicht der effektive Strahlungsantrieb einer CO_2 Erhöhungssimulation, mit ähnlich großem klassischen Strahlungsantrieb, weniger stark ab. Im direkten Vergleich mit diesen CO_2-Experimenten ist der effektive Strahlungsantrieb von Kondensstreifen-Zirren im EMAC (ECHAM5) Modell um 45 % (58 %) reduziert, was bereits auf eine reduzierte Klimawirkung von Kondensstreifen-Zirren hindeutet. Die Simulationen wurden darüber hinaus mittels Rückkopplungsanalyse untersucht, um einen vollständigen Satz konsistenter schneller Strahlungsrückkopplungen zu bestimmen. Als Ursache für den reduzierten effektiven Strahlungsantrieb konnte eine negative Wolkenrückkopplung, aufgrund einer Abnahme der natürlichen Zirrus-Bewölkung, festgestellt werden.

Zur Bestimmung der tatsächlichen Klimawirkung wurde die durch Kondensstreifen-Zirren verursachte Änderung der mittleren globalen Bodentemperatur direkt, mit Hilfe des an einen interaktiven Ozean gekoppelten EMAC Modells, simuliert. Zum ersten Mal konnten damit die Klimasensitivität und Klimawirkungseffizienz von Kondensstreifen-Zirren bestimmt werden. Insgesamt fällt die Bodentemperaturänderung aufgrund von Kondensstreifen-Zirren deutlich geringer aus als für eine CO_2-Erhöhungssimulation mit ähnlich großem klassischen Strahlungsantrieb. Der auf dem effektiven Strahlungsantrieb basierende Wert der Klimawirkungseffizienz beträgt 0.38 und weicht damit erheblich vom zu erwartenden Wert 1 ab. Bezogen auf den klassischen Strahlungsantrieb beträgt die Klimawirkungseffizienz sogar nur 0.21. Somit fällt die durch Kondensstreifen-Zirren induzierte Änderung der mittleren globalen Bodentemperatur weitaus geringer aus als der effektive und der klassische Strahlungsantrieb vermuten lassen. Mit Hilfe der Rückkopplungsanalyse konnten Unterschiede im Verhalten der tiefen und mittelhohen Bewölkung, verglichen mit dem CO_2 Referenzfall, als wesentliche Ursache für die geringe Klimawirkungseffizienz identifiziert werden.

Zusammenfassend kann festgestellt werden, dass es neue und sehr deutliche Hinweise darauf gibt, dass die Verwendung von Strahlungsantrieben bei der Bewertung der Klimawirkung des Luftverkehrs zu einer erheblichen Überschätzung der relativen Bedeutung von Kondensstreifen-Zirren für die durch den Luftverkehr induzierte globale Erwärmung führen kann. Da mehrere zentrale Ergebnisse dieser Arbeit einzigartig und erstmalig sind, ist eine Bestätigung durch andere Klimamodelle, welche mit einer adäquaten Kondensstreifen-Zirren Parametrisierung ausgestattet sind, sehr wünschenswert.

Abstract

Air traffic has been growing exponentially over the last decades and thus plays an important role for future climate mitigation strategies. Contrail cirrus is regarded to be the largest contributor to aviation induced climate impact on the basis of radiative forcing estimates, exceeding aviation's CO_2 emissions. While previous studies revealed a reduced efficacy of linear contrails in forcing the global mean surface temperature, that has not yet been analyzed for the far more important contrail cirrus.

In the context of the present thesis, various climate model simulations were performed in order to gain a better understanding about the climate impact of contrail cirrus. The simulations were conducted with the ECHAM5 and EMAC climate models, equipped with a state-of-the-art contrail cirrus parameterization, and were further analyzed by feedback analysis after the partial radiative perturbation method in order to determine the rapid radiative adjustments and slow feedbacks.

First, the climate impact of contrail cirrus was assessed on the basis of radiative forcings, determined by fixed sea surface temperature simulations. The effective radiative forcing of contrail cirrus turned out to be largely reduced with respect to the conventional radiative forcings. In contrast, the effective radiative forcing of a CO_2 increase simulation, with a similarly sized conventional radiative forcing, deviates less strongly. If directly compared to those CO_2 reference experiments, the contrail cirrus effective radiative forcing is reduced by 45 % (58 %) for the EMAC (ECHAM5) model, which already indicates a reduced climate impact of contrail cirrus. The simulations were further analyzed by feedback analysis to determine a full set of consistent rapid radiative adjustments. A negative natural cloud adjustment due to a reduction of natural cirrus cover was found to be the main origin for the reduced effective radiative forcing of contrail cirrus.

To determine the actual climate impact, the global mean surface temperature change, induced by contrail cirrus, was directly simulated with the EMAC model coupled to an interactive ocean. For the first time, the climate sensitivity and efficacy parameters of contrail cirrus could be determined. Overall, the surface temperature change due to contrail cirrus turns out to be considerably smaller than for a CO_2 increase simulation with a similarly sized conventional radiative forcing. The efficacy parameter, based on the effective radiative forcing, is 0.38, deviating significantly from the theoretically expected value of 1. In terms of conventional radiative forcing, the efficacy parameter is as low as 0.21. Therefore, the global mean surface temperature change induced by contrail cirrus is clearly weaker than suggested by, both, the effective and the conventional radiative forcing. Feedback analysis identified changing low and mid level clouds, in comparison to the CO_2 reference case, as main reason for the small efficacy parameter.

In conclusion, there is new and distinct evidence that the use of radiative forcing in aviation climate impact assessments may lead to substantial overestimation of the relative importance of contrail cirrus for aircraft induced global warming. Nevertheless, as several key findings of the present thesis are unique, confirmation from other climate models, equipped with an adequate contrail cirrus parameterization, is regarded as highly desirable.

Declaration

Some results of the present thesis have already been published in the following articles:

Bickel, M., M. Ponater, L. Bock, U. Burkhardt, and S. Reineke, 2020: Estimating the Effective Radiative Forcing of Contrail Cirrus. *Journal of Climate*, 33 (5), 1991 – 2005, https://doi.org/10.1175/JCLI-D-19-0467.1

Ponater, M., M. Bickel, L. Bock, and U. Burkhardt, 2021: Towards Determining the Contrail Cirrus Efficacy. *Aerospace*, 8 (2), https://doi.org/10.3390/aerospace8020042

Contents

Chapter 1

Introduction

1.1 Motivation

Aviation contributes about 3.5 % to man-made climate change if assessed on the basis of radiative forcings (Lee et al., 2021). In recent years, air traffic has been growing largely exponentially, until the COVID-19 pandemic outbreak (see Fig. 1.1). This general trend is expected to continue soon and thus is of major importance to be addressed by future mitigation strategies. Aircraft affect the global climate mainly through CO_2, water vapor, NO_x and soot emissions. Under certain ambient conditions emitted water vapor may condense and form a linear contrail directly behind the engine exhaust (e. g. Schmidt, 1941; Appleman, 1953). If the ambient air is cold and humid enough, linear contrails may spread over large areas and develop into the more important contrail cirrus (e. g. Schumann, 1996; Minnis et al., 1998; Schumann, 2005; Lee et al., 2010), which are considered to contribute the largest part to aviation induced radiative forcing (RF) (Lee et al., 2021). While local in-situ measurements of microphysical contrail properties (e. g. Schröder et al., 2000; Voigt et al., 2010, 2017) and remote sensing measurements of the radiative impact of contrail cirrus exist (e. g. Meyer et al., 2002; Haywood et al., 2009; Schumann and Graf, 2013; Vázquez-Navarro et al., 2015; Gruber et al., 2018), a global assessment of the climate impact can only be achieved by climate model simulations (Ponater et al., 1996, 2002; Fuglestvedt et al., 2003; Burkhardt et al., 2010).

So far, the global climate impact of contrail cirrus has been mainly assessed on the basis of radiative forcings (Sausen et al., 2005; Lee et al., 2009; Chen and Gettelman, 2013, 2016; Bock and Burkhardt, 2016b, 2019; Grewe et al., 2017). For this purpose the well established conventional radiative forcing types RF_{inst} (instantaneous radiative forcing) and RF_{adj} (stratosphere adjusted radiative forcing) were primarily utilized. Combined with the so-called climate sensitivity parameter*, the surface temperature change can then be derived relatively easily, with the climate sensitivity parameter of CO_2 being often used as a forcing-independent reference value. However, climate sensitivity parameters tend to vary substantially between different forcers, which indicates that conventional radiative forcings

*global mean surface temperature change per unit radiative forcing

are potentially unsuited for direct use in deriving surface temperature changes (e. g. Joshi et al., 2003; Berntsen et al., 2005; Shindell, 2014; Richardson et al., 2019). For this reason Hansen et al. (2005) introduced the concept of efficacy, which forms a correction factor for the conventional radiative forcings, that describes the effectiveness of radiative forcings to warm Earth's surface. Ponater et al. (2005) and Rap et al. (2010) have shown that the efficacy parameter of linear contrails (not contrail cirrus) is reduced. Or in other words: The induced global mean surface warming of linear contrails is smaller than the associated conventional radiative forcing would suggest. To overcome problems related to varying efficacy parameters, an improved global mean radiative forcing definition was developed, that features a better proxy for surface temperature change: the effective radiative forcing (ERF, Hansen et al., 2002; Shine et al., 2003; Gregory et al., 2004). The difference between ERF and the conventional radiative forcings can be explained by so-called rapid radiative adjustments (RA). RAs are feedback processes that evolve on a relatively short timescale, within weeks or month, as a direct reaction to the initial perturbation, much faster than surface temperature induced slow feedbacks (SF) that are coupled to the relatively inert ocean.

ERF determination for contrail cirrus has already been approached by Burkhardt and Kärcher (2011) and Gettelman and Chen (2013). However, the applied methods of both studies are to some extent insufficient for deriving an ERF according to the definition, be-

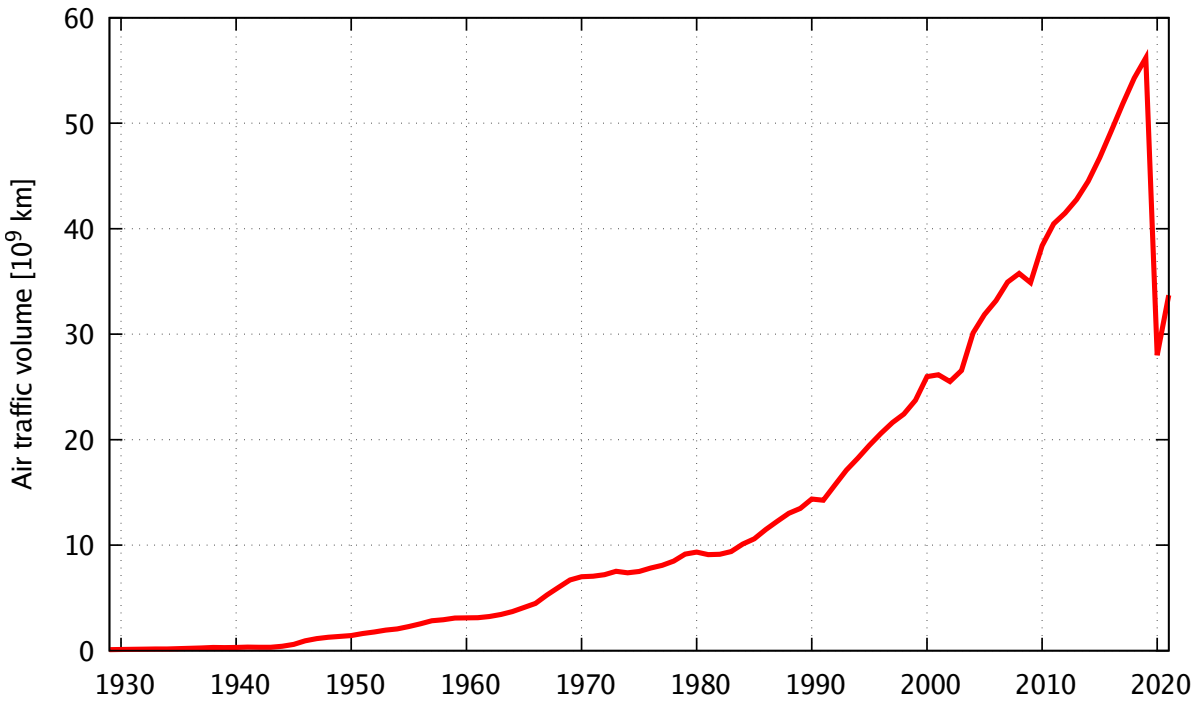

Figure 1.1: Air traffic volume for the years 1929 to 2021 based on data from ICAO (1995–2021) and Airlines for America (2021).

cause a complete consideration of all fully evolved RAs has not been ensured. As the ERF represents the recommended radiative forcing to be used since the 5th IPCC Assessment Report (IPCC, 2013), a contrail cirrus ERF, determined with one of the approved definitions (Forster et al., 2016), is highly desirable. As common in current climate research the ERF calculations should be supported by feedback analysis in order to derive a full set of consistent RAs (e. g. Vial et al., 2013; Smith et al., 2018, 2020), which is extremely helpful for gaining deeper insights in the radiative processes related to contrail cirrus climate impact.

Furthermore, recent studies indicate that for some forcers even the ERF may be an insufficient proxy for estimating surface temperature changes (Marvel et al., 2016; Richardson et al., 2019). This is particularly true for forcers that are mostly distributed inhomogeneously, as is the case for contrail cirrus. Thus it needs to be clarified whether the ERF framework holds for contrail cirrus in predicting surface temperature changes. In order to clarify the open issues, a direct calculation of the actual surface temperature change, induced by contrail cirrus, is urgently needed. Additionally the analysis of SFs might help to explain the physical origin of a potentially deviating reaction of surface temperature change in comparison to the CO_2 reference behavior. SFs are those feedback processes that evolve on a relatively long timescale, over decades, due to changing surface temperatures. They balance the remaining flux imbalance until equilibrium is reached.

In summary, the available ERF estimates of contrail cirrus are still associated with considerably large uncertainties, while the induced surface temperature change, climate sensitivity parameter and efficacy parameter have remained largely unknown. As humans live on Earth's surface, the surface temperature change is often regarded as the crucial key indicator for global climate change. Especially, for future mitigation strategies, for example to contribute to the Paris agreement (limiting global warming below 2°C) it is essential to know the actual surface temperature change induced by contrail cirrus. The current lack of knowledge provides the motivation for the present thesis in order to gain a deeper understanding of the climate impact of contrail cirrus.

1.2 Scientific Questions

The open issues stated above motivated the following fundamental scientific questions of the present thesis:

Q1: What is the magnitude of contrail cirrus ERF when determined by the most appropriate method? How much does the ERF deviate from the conventional radiative forcings?

Q2: Which physical processes (rapid radiative adjustments) are responsible for the deviation between the ERF and the conventional radiative forcing values?

Q3: How much does contrail cirrus warm Earth's surface ($\Delta T_{surface}$, climate sensitivity parameter)?

Q4: Does the expected global mean surface temperature change, based on radiative forcings, correspond with the directly calculated surface temperature change (efficacy parameter)?

Q5: Which physical processes (slow feedbacks) explain a potentially deviating response of the surface temperature in the case of contrail cirrus and CO_2?

1.3 Investigation Strategy

For answering the scientific questions mentioned above the work for the present thesis was split in two major parts. The first part covers the derivation of the various radiative forcings and RAs, while the second part focuses on the surface temperature change and related subjects such as climate sensitivity parameter, efficacy parameter and SFs. The results presented here were mainly derived by global climate model simulations.

Both parts are based on the state-of-the-art and well evaluated contrail cirrus parameterization CCMod developed by Bock and Burkhardt (2016a,b, Sect. 3.1.3), originally implemented in the ECHAM5 climate model (Roeckner et al., 2003, 2006, Sect. 3.1.1). The conventional radiative forcings (RF_{inst} and RF_{adj}) are derived with the radiation double calling technique which results in highly statistically significant results (Stuber et al., 2001). To derive the ERF, various techniques can be used, e. g. regression based methods or the nudging approach (Gregory et al., 2004; Forster et al., 2016). For the present thesis the fixed sea surface temperature (FSST) method with a free-running climate model was chosen for ERF calculations, as it is specially designed to allow the RAs to fully evolve (Forster et al., 2016, not ensured for the nudging approach) while holding the statistical uncertainties within limits (larger for regression based methods). Nevertheless, statistical uncertainties in the FSST approach remain considerably larger than in case of the radiation double calling technique. This, in combination with the relatively small contrail cirrus radiative forcings (e. g. compared to CO_2 doubling simulations), lead to difficulties in obtaining statistically significant results. In order to identify the signal from the background

noise the underlying air traffic dataset needed to be scaled. Multiple simulations with different scalings were performed to yield the optimal scaling factor (Sect. 4.1.1) and to investigate the consequences of the scaling technique (e. g. due to saturation effects and other non-linearities, see Sect. 5.1). By scaling air traffic data it was possible to determine ERFs with sufficient statistical significance (Q1, Sects. 4.1.1 and 4.2.1). As CO_2 increase simulations are needed as reference, the scaling experiments were accompanied by respective CO_2 increase simulations with similarly sized radiative forcings in order to ensure a fair comparison of the resulting climate sensitivity and efficacy parameters (Hansen et al., 2005). In addition, the FSST simulations were further analyzed by a feedback analysis tool, specially designed for the ECHAM5 model by Klocke et al. (2013) and Rieger et al. (2017). This allows for a consistent determination of all RAs in order to physically explain the differences between the conventional radiative forcings and ERF as well as between the contrail cirrus and CO_2 case (Q2, Sects. 4.1.2 and 4.2.2).

The second part of the present thesis focuses on the direct simulation of the contrail cirrus induced surface temperature change. For this purpose the model environment was switched to the more comprehensive and flexible ECHAM/MESSy Atmospheric Chemistry (EMAC) model (Jöckel et al., 2010), because an extensively tested and well established interactive mixed-layer ocean (MLO) was available (Kunze et al., 2014; Stecher et al., 2021). Based on the experience obtained with the ECHAM5 scaling experiments, the EMAC simulations could be performed with an appropriate scaling factor right from the beginning. The FSST simulations were repeated with the EMAC model, analogously to those of ECHAM5, in order to derive consistent conventional radiative forcings and ERFs (Sect. 4.2.1) which could later be used for the climate sensitivity and efficacy parameter calculations. To calculate the surface temperature change itself, four simulations with coupled MLO were performed, consisting of a reference simulation, the contrail cirrus experiment and two CO_2 increase simulations. By combining the results of the FSST and MLO simulations further conclusions regarding the potential of contrail cirrus to warm Earth's surface can be drawn (Q3, Sects. 4.2.3 and 4.2.4). The CO_2 simulations allow for a determination of the actual efficacy of contrail cirrus to induce surface temperature changes (Q4, Sect. 4.2.4). All MLO simulations were further analyzed by feedback analysis in order to derive the SFs which help to explain a deviating response of the surface temperature between contrail cirrus and CO_2 (Q5, Sects. 4.2.5 and 4.2.6).

Chapter 2

Scientific Background

This chapter gives an overview about the physical basis and climate impact of contrail cirrus. Besides the description of the principles of contrail formation and development, the radiative impact of contrail cirrus is discussed in detail. In order to get a fundamental understanding of the radiative processes the Earth-atmosphere radiation budget is explained. The effects of a carbon dioxide (CO_2) increase are also addressed as most contrail cirrus simulations are interpreted in relation to CO_2 experiments. The technical background, of how the results are derived, can be found in chapter 3.

2.1 Air traffic and climate

Global air traffic has been growing exponentially over the last decades. Current growth rates have been strongly interrupted by the COVID-19 crisis, but the general trend is expected to continue soon, as it has done after several smaller drops in the past (see Fig. 1.1). The spatial distribution of air traffic is rather inhomogeneous with about 93 % of all flights taking place over the northern hemisphere (based on Wilkerson et al., 2010, for the year 2006). Local maxima can be found over Europe, USA and China (see Fig. 3.1).

Modern aircraft are powered by jet engines that burn kerosene. The most important emissions are CO_2, water vapor, nitrogen oxides (NO_x), soot and sulfate. When leaving the engine exhaust, these components are mixed with the ambient air and interact with the environment through different physical and chemical processes. For example, CO_2 and water vapor act as greenhouse gases by directly affecting Earth's radiation budget, while nitrogen oxides (NO_x) emissions support ozone (O_3) formation and decrease the lifetime of methane (CH_4) (Lee et al., 2010). Emitted soot forms aerosols which directly affect Earth's shortwave radiation budget but also act as cloud condensation nuclei, which have an impact on cloud formation (Kärcher, 2017). Thus aviation triggers a wide range of physical and chemical processes that influence Earth's environment.

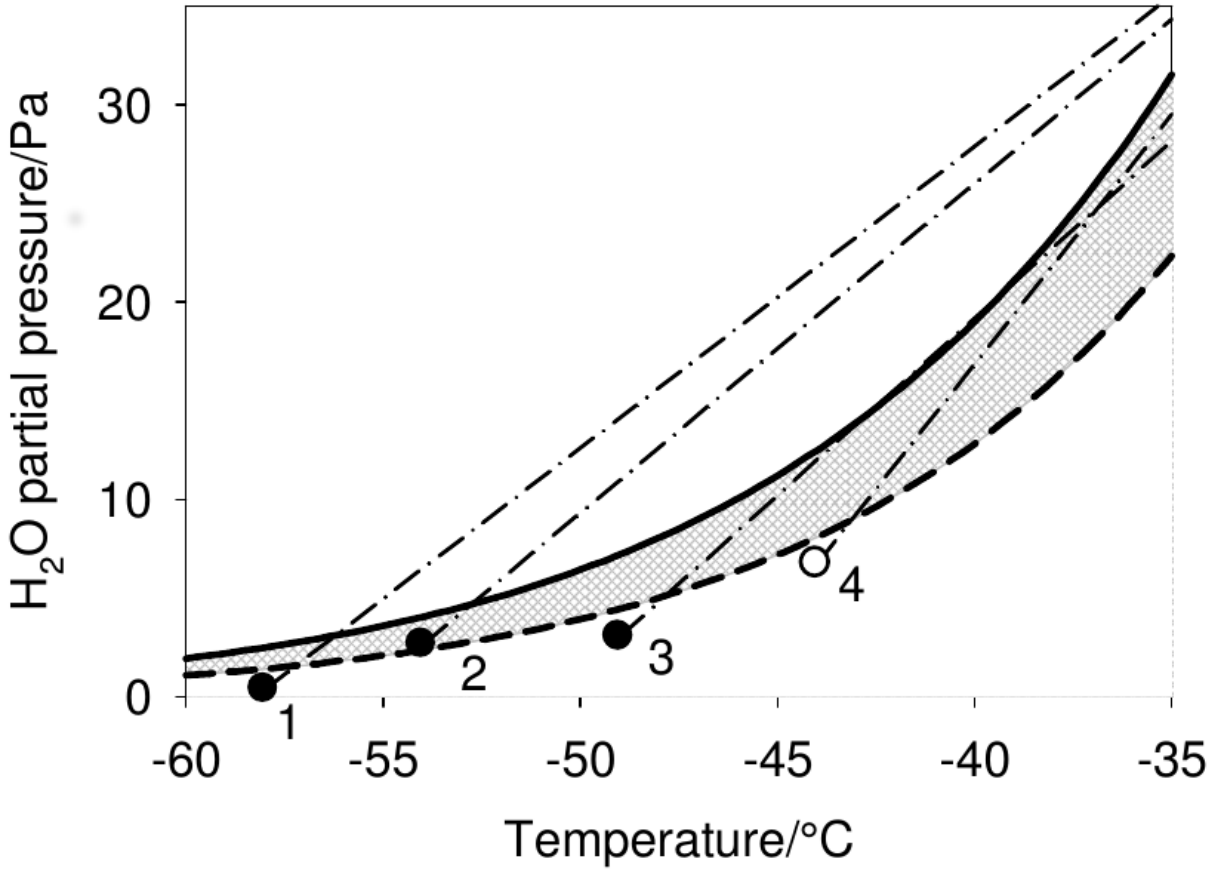

Figure 2.1: The diagram was originally created by Schumann et al. (2012a) in order to explain the contrail formation criteria. Shown is the phase diagram of water (water vapor partial pressure versus temperature) constrained by the saturation vapor pressure with respect to liquid water (solid curve) and ice water (dashed curve). Four different evolutions of cooling exhaust plumes are illustrated by means of isobaric mixing lines (dash-dotted lines). A contrail was observed for exhaust plumes that end with a closed dot (for further description see text).

2.2 Contrail cirrus

One aviation induced feature that has not been mentioned in the last subsection are contrails. After leaving the jet engine, the warm and moist exhaust plume is mixed with cold ambient air and cools down. If the ambient air is cold and humid enough, the water vapor in the exhaust plume condenses and forms a cloud, also known as condensation-trail or contrail. The process is very similar to our breath getting visible on a cold day. In detail the exhaust plume has to reach saturation vapor pressure of liquid water to form a contrail. This condition is also known as the Schmidt-Appleman formation criterion (Schmidt, 1941; Appleman, 1953; Schumann, 1996). In Fig. 2.1 the saturation vapor pressure with respect

to liquid water is depicted as the solid curve. Dash-dotted lines, marked with numbers 1-4, represent mixing ratios for different observed exhaust plumes. If the mixing line of an exhaust plume runs above the saturation vapor pressure curve of liquid water, at least for a short period of time, a contrail forms (see exhaust plumes 1, 2 and 3 in Fig. 2.1). The exhaust plume cools down until it reaches ambient air temperature (see endpoints of dash-dotted lines). If this final state is at least saturated with respect to ice (dashed line), beyond the formation criterion also the persistence criterion is fulfilled, and contrails can exist for several hours (see exhaust plume 2 in Fig. 2.1). Reaching the ice water saturation state without touching the liquid water saturation state, at least for a short period of time, is not sufficient to form a contrail. In contrast to that, observations show that natural cirrus clouds usually form only when large supersaturations of up to 140%-180% are reached (Koop et al., 2000; Krämer et al., 2009). For this reason the formation of contrails starts much earlier than for natural cirrus clouds.

Contrail formation begins with the condensation of water vapor into liquid water droplets in the supersaturated exhaust plume which subsequently freeze to build small ice crystals. The condensation process may occur homogeneously without condensation nuclei (below approx. -38°C) but also heterogeneously on the surface of aircraft emitted soot, sulfate particles or ambient aerosols. If the persistence criterion is fulfilled, ice particles may grow by absorbing ambient humidity. Overall, the water absorbed from the ambient supersaturated air by far exceeds what was initially emitted by the jet engine (e. g. Heymsfield et al., 1998; Schumann et al., 2012b). Vertical wind shear combined with high horizontal wind speeds (e. g. jet streams) spread contrails over large regions. During that process contrails loose their linear shape and develop into contrail cirrus (Minnis et al., 1998; Haywood et al., 2009; Mannstein et al., 2010). On the other hand, if only the formation criterion is fulfilled, but the persistence criterion is not, contrails get diluted with dry ambient air and dissipate quickly by evaporation (exhaust plume 1 and 3 in Fig. 2.1).

As soon as the linear structure is lost, contrail cirrus hardly differ from natural cirrus clouds, what makes it nearly impossible to distinguish between both with current remote sensing techniques. For this reason satellite based observations are mostly limited to linear contrails where detection algorithms can make use of the line-shaped structures (Minnis et al., 2013; Duda et al., 2013). However, if combined with further information (e. g. distinct air traffic patterns or weather observations) conclusions on the origin of a cirrus cloud can be drawn at least locally (Vazquez-Navarro et al., 2010; Schumann and Graf, 2013; Vázquez-Navarro et al., 2015).

For assessing contrail cirrus physical and radiative quantities on a global scale, climate models are the optimal choice (Burkhardt et al., 2010). Recent model studies calculated a global contrail cirrus coverage of up to 1.2% for the year 2006 (Bock and Burkhardt, 2016b). In contrast to that, linear contrails are estimated to cover only about 0.15 % of the Earth (Bock, 2014).

The present thesis focuses exclusively on the impact of contrail cirrus. Like natural ice clouds, contrail cirrus affect global climate mainly by changing the radiation budget of Earth's atmosphere. A description of the relevant radiative processes can be found in the next section.

2.3 Earth-atmosphere radiation budget

Global climate change is fundamentally linked to perturbations of Earth's radiative balance. To understand how contrail cirrus affect the climate system, it is necessary to know the basic radiative processes. The currently observed Earth-atmosphere radiation budget provides a good basis for this (Fig. 2.2).

The climate state of the Earth is mainly determined by radiation received from the sun. In climate research electromagnetic radiation is often referred to as radiative flux or irradiance and is defined as an amount of power received by a distinct surface area:

$$\mathrm{E} \;=\; \frac{\mathrm{Q}}{\mathrm{A}} \quad \left[\frac{\mathrm{W}}{\mathrm{m}^2}\right] \tag{2.1}$$

The radiative flux emitted by sun which reaches Earth is also known as solar constant and measured perpendicular to the incoming rays of the sun. Satellite observations yielded a mean solar constant of $1360.8\,\mathrm{Wm}^{-2}$ (Kopp and Lean, 2011). However, as Earth is a rotating sphere, the solar radiative flux needs to be distributed over the entire surface for global energy budget considerations. That results in a global mean solar irradiance of about $340\,\mathrm{Wm}^{-2}$, which on average enters Earth's atmosphere at the top of the atmosphere (TOA) (see Fig. 2.2). Largest energy emissions can be found at a wavelength of approximately 500 nm by simply substituting the surface temperature of the sun ($\sim$5772 K, Prša et al., 2016) into Wien's displacement law (Wien, 1893). This implies that most of the sun's energy is emitted in the visible and near infrared part of the electromagnetic spectrum, which is in meteorology usually referred to as shortwave (SW) or solar radiation (represented by yellow arrows in Fig. 2.2). When entering the atmosphere the solar radiation interacts with gases, particles and clouds. On its way down to surface the solar radiation is partially absorbed by the atmosphere ($79\,\mathrm{Wm}^{-2}$), as well as reflected by clouds ($76\,\mathrm{Wm}^{-2}$). That results in only about half of the irradiance, which enters the atmosphere at TOA, to reach Earth's surface ($185\,\mathrm{Wm}^{-2}$). Caused by Earth's global mean surface albedo of 0.13 (Wild et al., 2013), about $24\,\mathrm{Wm}^{-2}$ are reflected by Earth's surface. The remaining $161\,\mathrm{Wm}^{-2}$ are absorbed by Earth's surface, where the radiation is transformed into sensible heat (warming of Earth's surface). In total about $100\,\mathrm{Wm}^{-2}$ of the incoming solar irradiance are reflected to space ($76\,\mathrm{Wm}^{-2} + 24\,\mathrm{Wm}^{-2}$).

Earth's global mean surface temperature for the year 2021 was about 288 K (NOAA National Centers for Environmental Information, 2022). After the Stefan-Boltzmann law (Stefan, 1879; Boltzmann, 1884; Ponater et al., 2012) a (black) body radiates power dependent on its temperature (T):

$$\mathrm{E}_{\mathrm{Boltzmann}} \;=\; \varepsilon \;\; \sigma \; \mathrm{T}^4_{\mathrm{surface}} \quad \left[\frac{\mathrm{W}}{\mathrm{m}^2}\right] \tag{2.2}$$

with ε being the emissivity and σ the Stefan-Boltzmann constant ($5.67 \cdot 10^{-8}\,\mathrm{W\,m^{-2}\,K^{-4}}$). The emissivity describes how efficiently a body can emit radiation. Earth's surface emissivity ranges between approximately 0.6 and 1.0, depending on surface and wavelength, and

is normally small (< 0.85) for semi-arid areas and deserts and large (> 0.95) for vegetation, water and ice (Hulley et al., 2015).

When substituting the global mean surface temperature of Earth into Eq. 2.2 and assuming a global mean emissivity of the Earth's surface close to unity an emitted radiative flux of about $398\,\mathrm{Wm}^{-2}$, as shown in Fig. 2.2, can be calculated. Using again Wien's displacement law the largest amount of energy that is emitted at those temperatures consists of average wavelengths around $10\,\mu\mathrm{m}$ (Wien, 1893). Therefore the largest amount of energy is emitted in the infrared part of the electromagnetic spectrum, which is also referred to as longwave (LW) or thermal radiation (represented by orange arrows in Fig. 2.2). The LW radiative balance is strongly influenced by greenhouse gases (e. g. water vapor, CO_2, CH_4) and to a lesser extent by clouds. Greenhouse gases as well as liquid and ice cloud particles absorb large parts of the LW radiation emitted by Earth's surface. This effect makes the atmosphere relatively opaque for LW radiation and leads to absorption and re-emission at various altitudes. After the Stefan-Boltzmann law molecules in the atmosphere re-emit radiation depending on their temperature. On average the re-emission is uniformly radiated in all directions, meaning that the initial upward LW flux is partly re-emitted downward.

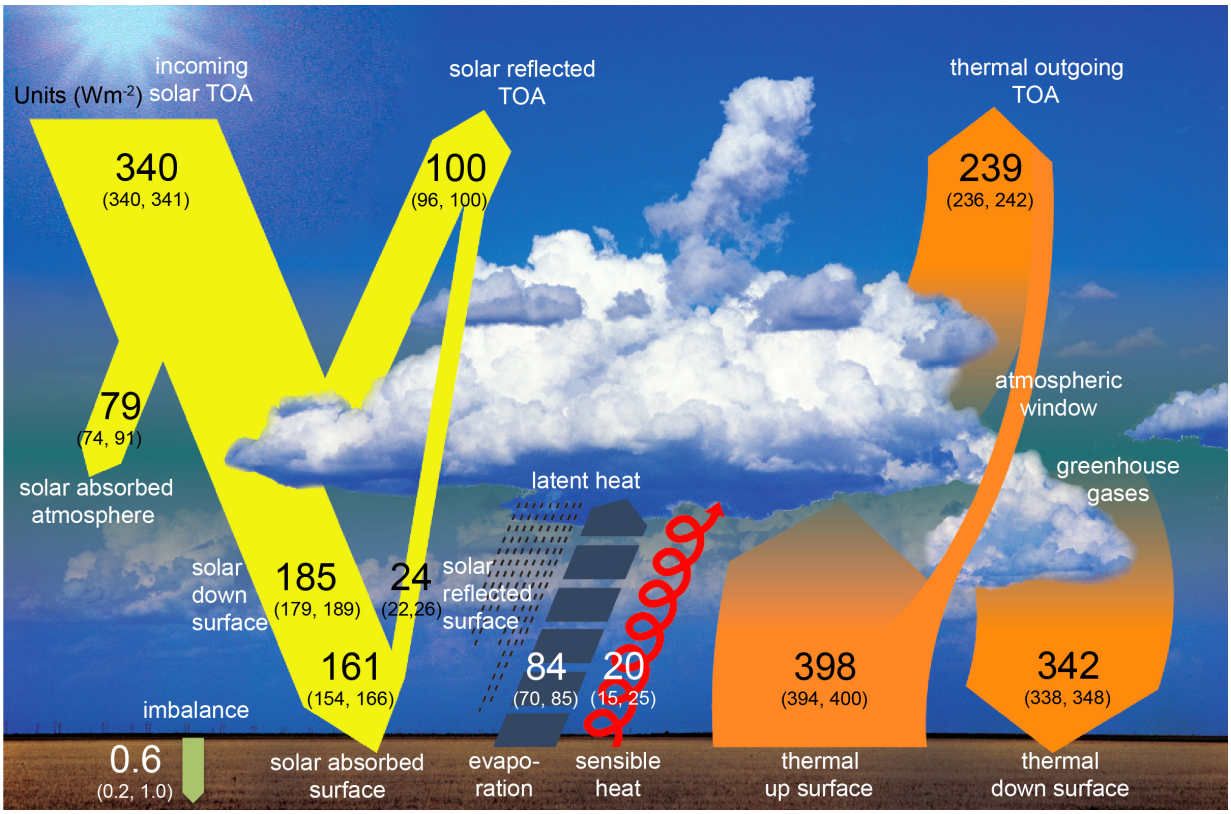

Figure 2.2: Observed Earth radiation budget as originally illustrated in the 5$^{\mathrm{th}}$ Assessment Report of the IPCC (Hartmann et al., 2013). The schematic gives an overview of the important radiative processes in Earth's atmosphere in order to explain how climate works. A detailed description can be found in the text.

This process acts like a radiative energy trap, which reduces LW emissions to space. In total, greenhouse gases and clouds cause $342\,\mathrm{Wm^{-2}}$ of LW radiation to be re-emitted to Earth's surface (see Fig. 2.2). This process is also known as greenhouse effect. Without an atmosphere (greenhouse gases and clouds) Earth's surface temperature would be far cooler, even below the freezing point of water (Lacis et al., 2010; Ponater et al., 2012). Approximately $239\,\mathrm{Wm^{-2}}$ of LW radiation are emitted to space.

To close the energy budget at the surface, beyond radiative fluxes also latent and sensible heat fluxes need to be taken into account. For example, heat from the surface can be directly transported into the atmosphere by ascending air. This is mainly induced by convective processes which account for about $20\,\mathrm{Wm^{-2}}$ of sensible heat which is transported into the atmosphere. Sensible heat at the ground is also absorbed to evaporate water, which is then stored in the atmosphere. When transported to higher altitudes the air cools down until the stored water may condense again and a cloud forms. This condensation process releases a large amount of latent heat into the atmosphere ($84\,\mathrm{Wm^{-2}}$).

2.4 Radiative forcing

As described above the Earth-atmosphere radiation budget is mainly controlled by solar and thermal radiative fluxes. In climate equilibrium, the long-term global mean SW and LW radiative fluxes are balanced at TOA. At the surface the energy balance is closed by sensible and latent heat fluxes. With $340\,\mathrm{Wm^{-2}}$ of incoming ($\mathrm{E_{\downarrow}}$) and $339\,\mathrm{Wm^{-2}}$ of outgoing radiative fluxes ($\mathrm{E_{\uparrow}}$) the TOA radiative flux balance of the current atmosphere is almost closed except for $1\,\mathrm{Wm^{-2}}$ (see Fig. 2.2). Any such radiative imbalance at TOA is called radiative forcing (RF):

$$\mathrm{RF} \;=\; \mathrm{E_{\downarrow}} \;-\; \mathrm{E_{\uparrow}} \quad \left[\frac{\mathrm{W}}{\mathrm{m^2}}\right] \tag{2.3}$$

A positive radiative forcing, as seen in Fig. 2.2, means that more radiation is entering the system than is emitted to space. Excessive radiation is partly absorbed by Earth's atmosphere and surface, where it is transformed into sensible heat. A positive radiative forcing leads in principle to a warming of Earth's surface while a negative radiative forcing results in a cooling:

$$\mathrm{RF} \;\sim\; \Delta \mathrm{T_{surface}} \tag{2.4}$$

$$\begin{aligned} \mathrm{RF} \;&>\; 0 \quad \rightarrow \text{ Warming} \\ \mathrm{RF} \;&<\; 0 \quad \rightarrow \text{ Cooling} \\ \mathrm{RF} \;&=\; 0 \quad \rightarrow \text{ Equilibrium} \end{aligned}$$

In Fig. 2.2 approximately $0.6\,\mathrm{Wm^{-2}}$ are absorbed by Earth's surface. This radiative imbalance is the main driver of current global surface warming. The remaining imbalance of about $0.4\,\mathrm{Wm^{-2}}$ is absorbed by Earth's atmosphere (not shown in Fig. 2.2). It is also

important to note that the troposphere is closely coupled to the Earth's surface through vertical mixing, so radiative energy deposited anywhere in this coupled system gets swiftly distributed over the whole global domain.

If the radiative forcing is zero the amount of radiation that is leaving the global system at TOA equals the amount of radiation that is entering (radiative equilibrium). Thus the atmosphere is in a stationary state and the global mean temperature of the troposphere and surface nearly remain constant in the global long-term mean.

Besides surface temperature change, the radiative forcing metric is regarded as one of the most popular proxies for estimating changes in the climate system. As radiative forcings represent the source of slowly evolving surface temperature changes they can be determined long before the actual surface temperature change has fully developed. Surface temperatures are known to react slowly (over decades), as they are delayed by the the relatively inert oceans.

Some greenhouse gases (e. g. CO_2) do have a relatively strong impact on the stratosphere, which is well decoupled from the troposphere below, as convective mixing terminates near the tropopause and stable stratification prevails at higher altitudes. In this case radiative forcings calculated at the TOA can be misleading when used to estimate surface temperature changes. To exclude those stratospheric impacts, the radiative forcing can be preferably determined at tropopause height (e. g. Hansen et al., 1997).

2.5 Radiative impact of contrail cirrus

Fig. 2.2 shows a general description of the current climate system, considering the most important climate relevant agents. Within this general framework, the present thesis focuses almost exclusively on the climate impact of contrail cirrus and the corresponding feedbacks. Contrail cirrus, as a component of clouds in general, play a non-negligible role in global climate and for anthropogenic climate change. More than one half of the Earth's surface is on average covered with clouds (King et al., 2013). The radiative effectiveness of clouds is often expressed in terms of optical thickness which describes the amount of radiative flux which is absorbed or scattered by the cloud particles. Optical thickness is dependent on the microphysical properties of the cloud, which are specified by the liquid and ice water content, particle number concentration, particle size, and in case of ice clouds the particle shape. Clouds affect the SW part as well as the LW part of the global radiation budget. To illustrate their relevance for global climate two basic cloud types are discussed here. Fig. 2.3 shows the radiative influence of low, thick liquid water clouds (a) and high, mostly thin ice clouds (b).

Low liquid water clouds (stratus, cumulus, cumulonimbus, fog) are often optically thick, so that much of the incoming solar radiation is scattered at or just below the cloud tops. This means that the solar radiation reaching the surface is reduced substantially. On the other hand cloud droplets act similar to greenhouse gases by absorbing LW radiation. Thus the greenhouse effect below thick clouds is to some extent enhanced and more LW radiation is re-emitted towards surface. However, the relative strength of the induced greenhouse

effect depends on the temperature difference between the cloud and the surface. As this temperature difference is rather small for low clouds the greenhouse effect is comparatively weak in contrast to clouds with higher ceilings. For this reason the dampened incoming SW radiation is dominating the enhanced LW part, meaning that the induced net radiation budget change at TOA is negative (Allan, 2011). Therefore low, optically thick, liquid water clouds have a surface cooling effect on average.

Naturally formed high and thin ice clouds (e. g. cirrocumulus, cirrostratus) do hardly differ from contrail cirrus. In terms of microphysical properties young contrail cirrus is mainly characterized by a larger amount of ice particles, which have an overall smaller diameter than natural cirrus (Voigt et al., 2017). The main reason for that is the increased availability of condensation nuclei (soot and sulfate particles) in the exhaust plume of aircraft, in contrast to the relatively low concentration of background aerosol which is available for natural cirrus formation. However, the fundamental radiative effect of both cirrus cloud types remains similar.

Thin cirrus clouds let the SW radiation pass almost unhindered, while only a small amount is reflected. Thus SW insolation at the surface is less affected than for the thicker low water clouds. Similar to low, thick clouds, cirrus clouds act comparable to greenhouse gases by reducing the outgoing longwave radiation (OLR). On satellite images, taken in

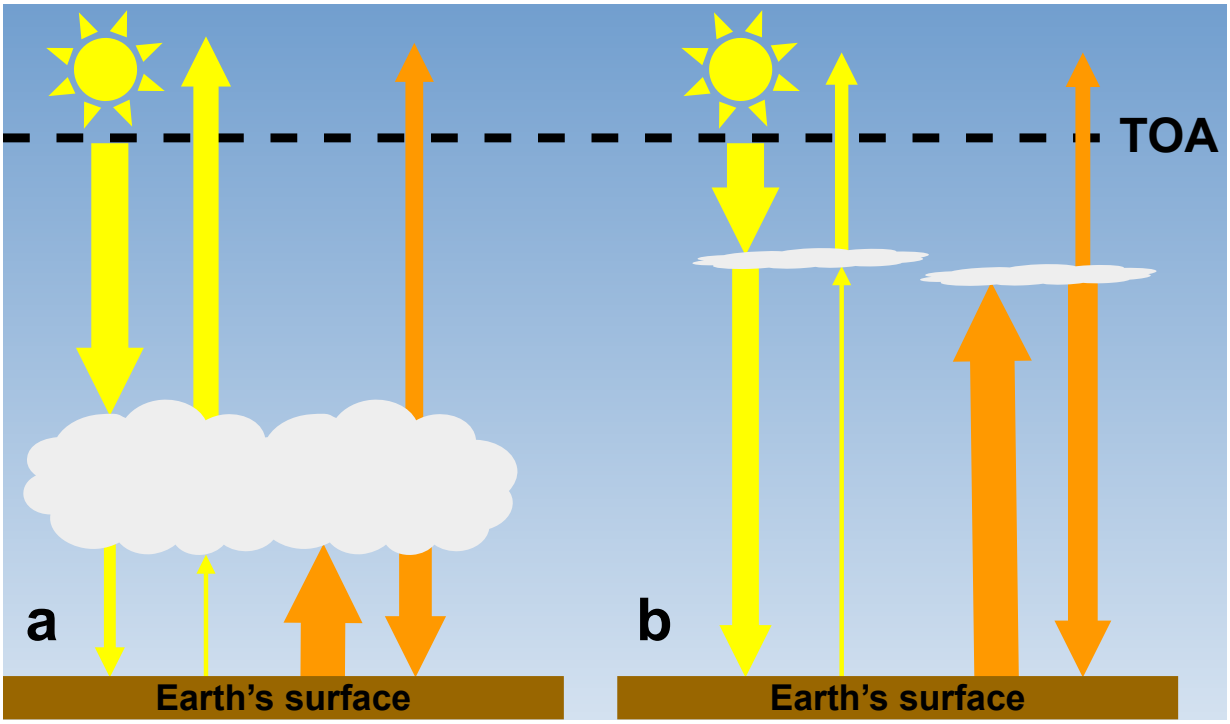

Figure 2.3: Illustration of the radiative impact of two common cloud types on Earth's radiation budget. On average low-altitude thick clouds (a) are cooling, while high-altitude thin clouds (b) are warming Earth's surface. Yellow arrows depict SW radiation and orange arrows LW radiation. A more detailed description can be found in the text.

the LW spectra, cirrus clouds can be identified as clearly distinguished spots because much less LW radiation is emitted. As explained above, the relative strength of the greenhouse effect depends on the temperature difference between the surface and the cloud and is therefore considerably stronger for ice clouds. For contrail cirrus the ratio of LW trapping to SW reflection is often about 2 to 1 in the long-term mean (Schumann and Graf, 2013, their Table A1). However, there is of course a large difference between day and night conditions because no SW forcing contributes at nighttime. Depending on the solar zenith angle contrails exceeding a certain optical depth may also cool, especially at daytime (e. g. Markowicz and Witek, 2011; Forster et al., 2012; Schumann and Heymsfield, 2017). On global average contrail cirrus, as well as natural cirrus, has a positive net radiative effect at TOA, which leads to a surface warming effect (Lee et al., 2009, 2021).

2.6 Rapid radiative adjustments

The radiative processes explained in Sect. 2.5 describe the direct response of the vertical radiative flux profile to a given perturbation (e. g. contrail cirrus or CO_2). The associated net radiative budget change at TOA (or, alternatively, at the tropopause level) is also referred to as instantaneous radiative forcing (RF_{inst}). RF_{inst} includes just the instantaneous radiative reaction to the perturbation and no follow-up processes.

In this way RF_{inst} characterizes the radiative effect of a perturbation only for a short period of time, right after it has formed. Shortly after, the atmosphere reacts to the forcing by changing its temperature and other physical properties. One typical example are stratospheric processes which are fairly well decoupled from the troposphere below and are known to adapt on a relatively short timescale, within weeks or months. For example a CO_2 increase results in a relatively fast cooling of the stratosphere through increased emission of LW radiation (Manabe and Wetherald, 1967; Stuber et al., 2001). Radiative adaptions that develop on a relatively short timescale are called rapid radiative adjustment (RA). The radiative flux adaption, which is caused by a changing temperature in the stratosphere, is called stratospheric temperature adjustment ($RA_{Strat.\,Temp.}$) and is not included in RF_{inst}. The modified radiative forcing type that results if $RA_{Strat.\,Temp.}$ is included is called stratosphere adjusted radiative forcing (RF_{adj}):

$$RF_{adj} \;=\; RF_{inst} \;+\; RA_{Strat.\,Temp.} \quad \left[\frac{W}{m^2}\right] \tag{2.5}$$

RF_{adj} is a far better proxy to estimate surface temperature changes (Ramaswamy et al., 2018).

However RF_{adj} does not take other rapidly evolving tropospheric adaptions into account. Such tropospheric adaptions are for example changes in the temperature profile of the troposphere as a reaction to the perturbation. If tropospheric temperatures increase (decrease) more (less) LW radiation is emitted to space (see Eq. 2.2). The radiative flux change, associated with the tropospheric temperature profile change, is called lapse rate adjustment ($RA_{Lapse\,Rate}$). As surface temperature changes are not included in $RA_{Lapse\,Rate}$,

temperature changes in the troposphere predominantly have an effect on the steepness of the temperature profile or in other words on the lapse-rate (temperature change per height). $RA_{\text{Lapse Rate}}$ may be viewed as a tropospheric counterpart to $RA_{\text{Strat.}}$, which describes temperature changes in the stratosphere.

Rapid adaptions in the vertical flux profile originate also from humidity changes in the atmosphere. As water vapor is a greenhouse gas, an increase (decrease) in humidity is associated with a strengthened (weakened) greenhouse effect, resulting in a warming (cooling). The corresponding radiative flux change due to humidity adaptions is called water vapor adjustment (RA_{H_2O}). The RA_{H_2O} is often directly coupled to the $RA_{\text{Lapse Rate}}$ as the amount of water vapor which can be carried by the atmosphere is dependent on temperature. The warmer (colder) the air, the more (less) water vapor can be held. For this reason, in a changing climate, where it may be assumed that the relative humidity remains approximately constant (Allen and Ingram, 2002), the absolute water vapor change depends to a certain extent on the temperature change.

Besides temperature and humidity, clouds can also rapidly adapt to the perturbation, e. g., as they are affected by changes in the tropospheric static stability. The radiative flux change which is caused by the adaption of natural clouds is called natural cloud adjustment ($RA_{\text{Natural Clouds}}$). It includes changes in cloud cover as well as cloud microphysical properties such as ice crystal number concentration (ICNC), ice water content (IWC) and effective radius (r_{eff}).

If all RA are taken into account, the so-called effective radiative forcing (ERF) is yielded (Ramaswamy et al., 2018; Smith et al., 2018, their Eq. 1):

$$\text{ERF} = \text{RF}_{\text{adj}} + \text{RA}_{\text{Lapse Rate}} + \text{RA}_{\text{H}_2\text{O}} + \text{RA}_{\text{Natural Clouds}} \quad \left[\frac{\text{W}}{\text{m}^2}\right] \tag{2.6}$$

The path from RF_{inst} to ERF is also illustrated in Fig. 2.4. If the RAs (solid red arrow) are added to RF_{inst}, the ERF is obtained.

Radiative flux changes due to adjustments of the surface temperature itself are, strictly speaking, not considered as a RA. As the surface temperature change is mainly controlled by oceans, its reaction is very slow, compared to the timescale of atmospheric RAs. Oceans do have a large heat capacity which delays the full development of the surface temperature adaption for (multiple) decades. However, a distinction is often made between land and sea surface. Land surface temperatures react much faster to radiative imbalances and are therefore often considered as RA (Vial et al., 2013). This also includes areas covered with sea ice. The radiative flux change associated with land or sea ice surface temperature changes is then named Planck adjustment (RA_{Planck}). Note that the respective surface temperature change is extended through all tropospheric layers above as the troposphere is considered to be relatively well mixed. The corresponding radiative flux changes are also included in RA_{Planck}.

A direct consequence of surface temperature changes is the adaption of the surface albedo. Glacier and sea ice cover is decreasing (increasing) if surface temperatures rise (drop). Less (more) ice or snow cover results in a decrease (increase) of the surface albedo

and thus in weakened (strengthened) reflection of SW radiation. Thus, a reduced (increased) surface albedo causes a warming (cooling). The radiative flux change due to a changing surface albedo is called albedo adjustment (RA_{Albedo}). RA_{Albedo} always amplifies the initial surface temperature change.

If radiative flux changes due to a land surface temperature increase, as well as associated follow-up effects, are considered as RA, the ERF is slightly lower (Vial et al., 2013). The resulting radiative forcing is than only maintained by the fixed sea surface temperatures

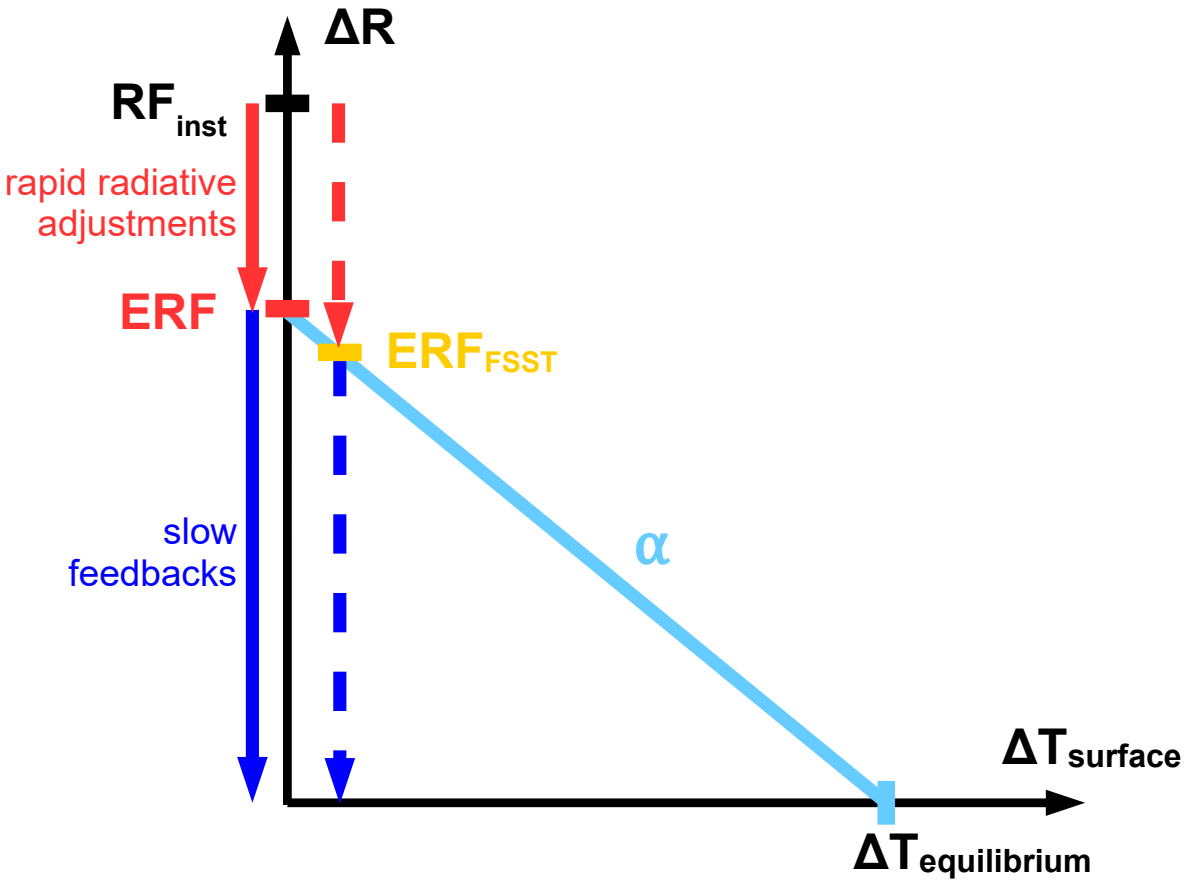

Figure 2.4: Illustration of the the link between surface temperature change and radiative forcings. The difference between RF_{inst} and ERF can be explained by rapid radiative adjustments (RA, red arrows, negative in this example). When comparing radiative forcings of different forcing agents, ERF is a far better proxy for estimating surface temperature changes. Slow feedbacks (SF, dark blue arrows) develop as a reaction to the surface temperature change and balance the remaining radiative imbalance (ERF) until a new equilibrium is reached. In literature radiative adaptions due to land surface temperature changes induced by the FSST method are often considered as rapid adjustment (Vial et al., 2013). As a consequence the surface temperature slightly adapts and the lower ERF_{FSST} is yielded.

(FSST) and is defined as ERF_{FSST}:

$$ERF_{FSST} = ERF + RA_{Planck} + RA_{Albedo} \quad \left[\frac{W}{m^2}\right] \tag{2.7}$$

ERF_{FSST} is also depicted in Fig. 2.4. Due to included RA_{Planck} and RA_{Albedo} the respective sum of all RA (dashed red arrow) is larger for ERF_{FSST}. As a consequence of the small rapid component of surface temperature change, ERF_{FSST} is already slightly shifted to the right in Fig. 2.4. Since the radiative forcing calculations performed for the present thesis are based on the FSST approach (further explained in Sect. 3.1.4) the ERF results presented later correspond with ERF_{FSST}.

As all fast adaptions of the atmosphere are taken into account, both ERF types (standard ERF and modified ERF_{FSST}) are conceptually superior to the conventional radiative forcings in comparing different forcing agents with respect to their surface temperature change. This has been confirmed empirically for quite a number of forcing mechanisms (e. g. Hansen et al., 2005) For this reason the ERF represents the recommended radiative forcing since the 5th IPCC Assessment Report.

2.7 Slow radiative feedbacks

Only much later than the RAs have been fully developed (within few months) the changing ocean temperature and related follow-up effects dominate the development of the atmosphere/surface system towards a new radiative and climate equilibrium. As sea surface temperature and the related feedbacks are gradually adapting, the radiative imbalance at TOA further decreases (Fig. 2.4, blue line). The sea surface temperature change is fully developed when the remaining radiative forcing approaches zero and a new state of equilibrium is reached. In nature this will require time-scales in the order of centuries for the deep ocean, yet the oceanic mixed-layer has a shorter time-scale of several decades. Radiative flux adaptions due to sea surface temperature changes and associated follow-up processes are referred to as slow feedback (SF). The radiative flux change from the sea surface temperature itself, including related land surface temperature changes, is called Planck feedback (SF_{Planck}). Due to the relatively well mixed troposphere the surface temperature change may be added to all tropospheric layers and the corresponding radiative flux change is also included in the SF_{Planck}. The remaining temperature change, e. g. variations in the steepness of the temperature profile, are taken into account in the $SF_{Lapse\,Rate}$. SFs exist for all processes mentioned above in the context of RAs ($SF_{Strat.}$, $SF_{Lapse\,Rate}$, SF_{H_2O}, $SF_{Natural\,Clouds}$, SF_{Albedo}). If all SFs are added to the ERF, radiative equilibrium should be reached:

$$\begin{aligned} ERF &+ SF_{Strat.\,Temp.} + SF_{Lapse\,Rate} + SF_{H_2O} \\ &+ SF_{Natural\,Clouds} + SF_{Planck} + SF_{Albedo} \approx 0 \end{aligned} \tag{2.8}$$

In Fig. 2.4 the sum of all SFs is depicted by dark blue arrows. The magnitude of the SF is dependent on the type of ERF (standard ERF: solid dark blue arrow or ERF_{FSST}:

dashed dark blue arrow). While RAs are predominantly induced by rapid adaptions of the atmosphere to the initial perturbation, SFs develop mainly as a reaction to the surface temperature change and balance the remaining radiative imbalance until a new equilibrium is reached. For this reason RAs and SFs of the same process can be structured very differently (see also Chung and Soden, 2015, their Figs. 8, 9, 11).

RAs and SFs can be separated relatively easily, in a technical sense, because their development time strongly differs (month vs. decades). In literature slow feedbacks are often divided by the final surface temperature change ($\Delta T_{surface}$) and are then called feedback parameters (FP):

$$FP_x = \frac{SF_x}{\Delta T_{surface}} \quad \left[\frac{W}{m^2\,K}\right] \tag{2.9}$$

$$x: \ \text{Strat. Temp.},\ \text{Lapse Rate},\ H_2O,\ \text{Natural Clouds},\ \text{Planck},\ \text{Albedo}$$

As FPs are calculated relatively to the absolute surface temperature change, they are better suited for directly comparing forcing agents of various type and magnitude. Similar to radiative forcings, RAs and SFs, as well as feedback parameters (FPs), are mainly determined at TOA.

The sum of all FPs yields the total feedback parameter (α, Ponater et al., 2012; Gregory and Andrews, 2016):

$$\alpha = \sum_x FP_x \quad \left[\frac{W}{m^2\,K}\right] \tag{2.10}$$

In Fig. 2.4 the total feedback parameter is represented by the gradient of the light blue line and describes the amount of RF that is needed for a distinct surface temperature change.

2.8 Climate sensitivity and efficacy parameters

Radiative forcings form the origin of temperature and climate changes and, as explained above, the surface temperature change is generally considered the key indicator of global climate change. The mathematical connection between the surface temperature change ($\Delta T_{surface}$) and the radiative forcing (RF) is given by the climate sensitivity parameter (λ):

$$\lambda = \frac{\Delta T_{surface}}{RF} = -\frac{1}{\alpha} \quad \left[\frac{K\,m^2}{W}\right] \tag{2.11}$$

Note that the negative inverse of the climate sensitivity parameter yields the feedback parameter (α).

Eq. 2.11 suggests that the climate impact ($\Delta T_{surface}$) of a forcing agent can be directly estimated if the respective radiative forcing is known and thus is indeed the reason and

purpose for the central role of radiative forcing in global climate research (Ramaswamy et al., 2018). A large (small) radiative forcing is assumed to lead to a large (small) surface temperature change. However, that assumption is only valid if λ is more or less constant for all climate agents. While this is mostly fulfilled among equally distributed greenhouse gases, it is not for linear contrails (Ponater et al., 2005). Similar deviations have also been confirmed for methane and black carbon (Richardson et al., 2019) as well as for a number of more exotic forcing processes (Marvel et al., 2016).

To adapt the conceptual framework, so that different climate agents (ca) can still be compared with respect to their impact on surface temperature change, Hansen et al. (1997, 2005) introduced the climate efficacy parameter (r):

$$\Delta T_{\text{surface, ca}} = \lambda_{CO_2} \cdot r_{ca} \cdot RF_{ca} \tag{2.12}$$

$$\text{ca (climate agents) : e. g. contrail cirrus, } CH_4, \text{ black carbon, ...}$$

Note that the climate sensitivity parameter of CO_2 (λ_{CO_2}) is used as a reference, so that the climate impact of different forcers are compared relatively to CO_2. The efficacy parameter, which depends on the climate agent, can be interpreted as a correction factor for the reference climate sensitivity of CO_2.

If combined with Eq. 2.11, the efficacy parameter can be written as:

$$r_{ca} = \frac{\lambda_{ca}}{\lambda_{CO_2}} \tag{2.13}$$

However, the type of climate agent is not the only factor that determines the efficacy parameter. For example, the efficacy parameter also depends on the radiative forcing type that is used. As described above, an essential part of the differences between radiative forcings can be explained by RAs, which are again dependent on the type of climate agent. The more RAs that are taken into account, the more effects, that are not related to surface temperature changes, are included. Meaning that the ERF is best suited, because it is only maintained by the slow reacting surface temperature. Thus, in theory, the ERFs (and the corresponding climate sensitivity parameter, based on ERF) of different climate agents should be better comparable regarding their surface temperature change. Or in other words, the efficacy parameter is expected to be approximately unity in the ERF framework. While this has empirically proved to be largely valid for well mixed climate agents, there are still outliers like CH_4 and black carbon, which have efficacy parameter smaller than 1 (Richardson et al., 2019). The physical origin can then be found in differently acting SFs, which tend to deviate if non-homogeneously acting feedback processes play a major role (e. g. forcers that are directly or indirectly affecting cloud properties). Deviations were found for linear contrails as well (Ponater, 2010), but are not yet determined for contrail cirrus. Furthermore, the climate parameters mentioned above are also known to depend on the individual climate model that is issued (Vial et al., 2013).

Finally, it is worth mentioning that radiative forcings and surface temperature change are not the one and only relevant indicators to assess the climate impact of an agent. Signals like the probability of extreme weather events or changes in precipitation are also

essential indicators for a changing climate, however, are not in focus of the present thesis. It will also not be addressed whether radiative forcing or surface temperature change are better suited to represent climate change in general. Still, when contributions to global warming are to be assessed or mitigated, e. g. when considering how to achieve the goals of the Paris agreement (2°C climate target), global mean surface temperature impact is obviously the target parameter.

In literature the ratio between ERF and RF_{adj} has often been identified with the efficacy parameter (e. g. in Lee et al. (2021), as no better estimates were available to them). However, this equivalence is only valid if certain conditions are fulfilled (as correctly pointed out in Appendix C of Lee et al., 2021). Following Ponater et al. (2021) the ratio between ERF and RF_{adj} can be expressed as:

$$\frac{ERF_{\text{contrail cirrus}}}{RF_{\text{contrail cirrus}}} = \frac{r_{\text{contrail cirrus}}}{r^*_{\text{contrail cirrus}}} \cdot \frac{ERF_{CO_2}}{RF_{CO_2}} \tag{2.14}$$

With $r_{\text{contrail cirrus}}$ and $r^*_{\text{contrail cirrus}}$ being the climate efficacy parameters in the conventional radiative forcing (with respect to RF_{inst} or RF_{adj}) and ERF framework respectively. Hence, the ratio between ERF and RF_{adj} only equals the efficacy parameter ($r_{\text{contrail cirrus}}$) if the ERF and the conventional radiative forcing of CO_2 are approximately equal and if the efficacy parameter of contrail cirrus in the ERF framework ($r^*_{\text{contrail cirrus}}$) is close to unity. The first condition is typically valid within a 10 % range, if RF_{adj} is used as conventional radiative forcing (respective radiative forcings are presented later in Tables 4.1 and 4.2). The second condition is the fundamental motivation and expectation when using the ERF framework. Yet, as deviations from this rule have already been demonstrated (see above), and contrail cirrus has never been investigated from this perspective, there is certainly good reason to perform direct simulations of surface temperature change from contrail cirrus. These will also allow to quantify whether ERF/RF_{adj} for contrail cirrus and $r^*_{\text{contrail cirrus}}$ is identical or not.

Chapter 3

Methods

In order to get a deepened understanding of the radiative impact and feedback processes induced by contrail cirrus, different methods and techniques were applied. This chapter focuses on the technical description of how the various results were derived. First the two climate models, including the most relevant modules and parameterizations, are described. Secondly a description of the feedback analysis tool follows which was developed and used to calculate the rapid radiative adjustments and slow feedbacks. The third part of this chapter describes the different simulations and evaluations which were performed to assess the various aspects of contrail cirrus climate impact.

3.1 Climate models

Direct determination of the climate impact of contrails and contrail cirrus on the basis of in-situ measurements or remote sensing techniques represents a major challenge for current science. While local radiative measurements of single contrails or contrail patterns have been successfully carried out and evaluated (e. g. Minnis et al., 1998; Meyer et al., 2002; Haywood et al., 2009; Schumann and Graf, 2013; Vázquez-Navarro et al., 2015; Schumann et al., 2017; Gruber et al., 2018), measurements on a global scale still pose an unsolved problem. Especially when spread over large areas, contrail cirrus simply differ too little from natural cirrus clouds, which impedes the development of contrail cirrus detection algorithms. Additionally, the overall climate impact of contrail cirrus is considerably small (e. g. compared to climate change induced by CO_2 or CH_4 increase) which causes problems to identify reliable signals from natural variability.

To overcome this problem, climate science widely makes use of climate models in order to globally simulate the physical properties and radiative impact of small but still important forcing mechanisms like contrails. The present thesis uses two climate models, equipped with a state-of-the-art contrail cirrus parameterization to deeply study the climate impact of contrail cirrus. In this section a description of both climate models, the ECHAM5 model and the EMAC/MESSy model environment can be found. Subsequently an detailed overview of the contrail cirrus parameterization (CCMod) is given. Hereafter follows a more

technical description of the methods to derive the different radiative forcings, including the fixed sea surface temperature (FSST) approach. The section closes with a brief description of the mixed-layer ocean (MLO) module, which was used in the EMAC/MESSy model environment in order to perform surface temperature change simulations.

3.1.1 ECHAM5

The simulations for the first part of the present thesis were performed with the ECHAM5 (5^{th} generation of the ECMWF model, Hamburg version) general circulation model (GCM) (Roeckner et al., 2003, 2006). The model version used here is based on the aerosol-climate model ECHAM5-HAM by Stier et al. (2005) and was equipped with the contrail cirrus parameterization CCMod by Bock (2014) (see Sect. 3.1.3 for details).

A resolution of T42L41 was chosen, which is equivalent to a Gaussian grid of approximately 2.8°×2.8° in latitude and longitude, with 41 vertical hybrid σ-pressure levels. This results in a grid box layout of 64 (latitude) × 128 (longitude) × 41 (vertical). The vertical layout is specially designed for simulations with contrail cirrus by a refinement of the vertical spacing in the upper troposphere and lower stratosphere. At 250 hPa the vertical extend of a grid box is approximately 500 m. The time integration is solved by a leapfrog scheme with a time step length of 15 min. A radiation call is performed every 60 min.

The cloud scheme was chosen according to Lohmann and Ferrachat (2010) (LF10) and represents the module (within the code) in which the key parts of the contrail cirrus parameterization are implemented. LF10 features a two-moment scheme for natural clouds, meaning that the water content and number concentration of liquid and ice cloud particles are both represented by prognostic variables (Lohmann et al., 2008). As the natural cloud cover scheme the parameterization after Sundqvist (1978) is used. The general model setup and tuning was adopted from Bock and Burkhardt (2016a,b). All other parameterizations, including the radiation scheme, are those described in Roeckner et al. (2003).

3.1.2 EMAC

The simulations for the second part of the present thesis were conducted with the ECHAM/MESSy Atmospheric Chemistry (EMAC) model (Jöckel et al., 2010). The model system was primarily switched because EMAC provides a well established and extensively tested MLO (see Sect. 3.1.5), which was necessary for the surface temperature change simulations. Furthermore, EMAC is clearly superior to the standard ECHAM5 model in terms of handling and modification capabilities, such as with respect to alternative cloud schemes (see below) or the use of the nudging technique (e. g. Jöckel et al., 2006; Lelieveld et al., 2007; Righi et al., 2020).

The configuration of EMAC is controlled by the Modular Earth Submodel System (MESSy, version used for the present thesis: 2.54). The main feature of MESSy is its modular layout which allows the user to create a highly customized climate model, that precisely addresses the needs of the proposed problem. The different components of the model are organized in submodels, which can be easily (de)activated and controlled via

namelists. In the present thesis ECHAM5 (version used: 5.3.02) is utilized as the core climate model with a resolution of T42L41. The chemical scheme was adopted from Righi et al. (2020) and covers the fundamental chemical reactions needed. Identical to the standard ECHAM5 model (see Sect. 3.1.1), time integration is solved by a leapfrog scheme with a time step length of 15 min. However, radiation calls were performed on a shorter interval of 45 min.

In EMAC the two-moment cloud scheme developed by Kuebbeler et al. (2014) (K14) was chosen instead of the LF10 parameterization. K14 is an enhanced version of LF10, with a new multiple-mode ice microphysical scheme for cirrus clouds. It includes a parameterization for homogeneous and heterogeneous ice formation (Kärcher et al., 2006; Righi et al., 2020). Furthermore, the MADE3 aerosol module of Kaiser et al. (2019) is used instead of the ECHAM-HAM aerosol parameterization (Stier et al., 2005).

Due to the change of the cloud scheme, one task of the present thesis was to implement the contrail cirrus parameterization CCMod in K14. That includes the coupling of CCMod to the MADE3 aerosol module, the re-implementation of the fractional cover for natural cirrus clouds and the reintroduction of the saturation adjustment, which is an essential part of CCMod (Bock and Burkhardt, 2016a, a detailed description follows in Sect. 3.1.3). As a result, the newly created contrail cirrus setup for EMAC (EMAC-CCMod) had to be retuned. The tuning aimed at maintaining the contrail cirrus physical properties well within the observational range, while keeping the global radiative imbalance at TOA low, in order to enable the coupling of the MLO. A more detailed description of the tuning process, including an evaluation against observations, can be found in Appendix A. As common with the MESSy framework, the CCMod extension in EMAC can be (de)activated and controlled via a namelist.

3.1.3 Contrail cirrus parameterization

The contrail cirrus parameterization CCMod, applied in the present thesis, was developed by Bock (2014) and is described and evaluated against observations in Bock and Burkhardt (2016a,b). The code is based on the contrail cirrus parameterization by Burkhardt and Kärcher (2009), which was originally built for ECHAM4. In the standard ECHAM5 model CCMod is integrated in the LF10 cloud scheme (Lohmann and Ferrachat, 2010) and is hereafter referred to as ECHAM5-CCMod. For the EMAC simulations, CCMod was implemented in the K14 cloud scheme (Kuebbeler et al., 2014) as part of the present thesis and is hereafter denoted as EMAC-CCMod.

In the model air traffic emissions are induced from an air traffic dataset which provides emitted water vapor and air traffic density (see Sect. 3.3.1). The subsequently called nucleation parameterization determines if the air is cold and humid enough to form ice particles. The contrail cirrus fraction is subdivided into a new and a pre-existing cloud part. Already existing ice particles are able to grow. CCMod is coupled to the aerosol parameterization HAM in standard ECHAM5 model (Stier et al., 2005) and to the MADE3 aerosol module in EMAC (Kaiser et al., 2019). Aerosol concentration provides an upper boundary for the amount of newly nucleated contrail cirrus ice particles. Contrail cirrus

is completely integrated in the hydrological cycle and competes with natural ice clouds for the ambient water vapor (Burkhardt and Kärcher, 2009).

Following the approach of Lohmann et al. (2008) for natural ice clouds, the two-moment scheme was also adopted for contrail cirrus. Thus IWC and ICNC of contrail cirrus are both prognostic variables. In the model prognostic contrail cirrus variables are treated as tracers, which are affected by advection and vertical diffusion. Further prognostic variables are contrail cirrus coverage, contrail cirrus volume and contrail cirrus length (mean length of all contrails in a grid-box). Overall, CCMod covers a wide range of processes: Contrail formation, volume growth due to turbulent diffusion and sedimentation, spreading from wind shear, deposition and loss of ice crystals from sublimation, sedimentation and precipitation.

In addition, changes to the maximum permitted humidity were required. Measurements show that large ice supersaturations of more than 200 % exist in cloud-free as well as inside of natural cirrus clouds (Krämer et al., 2009). For this reason Lohmann et al. (2008) implemented a nucleation parameterization which allows ice supersaturation in their two-moment cloud scheme. In the original model cirrus cloud formation due to homogeneous freezing starts at a relative humidity of about 150 % (Bock, 2014). On the other hand, natural cloud cover is also calculated as a function of relative humidity (Sundqvist, 1978). At a relative humidity of 100 % the complete grid box is covered with a cloud. Hence, if ice clouds form at a relative humidity of 150 % the cloud coverage in the grid box jumps immediately from 0 % to 100 % and no fractional cloud coverage is available. For this reason, there would be no space left for contrail cirrus if ice clouds already exist. To solve this problem Bock (2014) reintroduced the fractional cloud cover by limiting the maximum relative humidity to 100 %. Humidity exceeding the saturation level is converted into cloud ice. This approach is also known as the saturation adjustment (Lohmann and Kärcher, 2002) and was implemented in EMAC-CCMod as well.

3.1.4 Radiative forcing calculation and fixed sea surface temperature method

Over the last decades multiple radiative forcing definitions were developed and constantly improved (Hansen et al., 2005; Myhre et al., 2013; Ramaswamy et al., 2018). Within this thesis the instantaneous radiative forcing (RF_{inst}), the stratosphere adjusted radiative forcing (RF_{adj}) and the effective radiative forcing (ERF) are evaluated. While the radiative forcings have already been introduced and described in Sects. 2.4 and 2.6, this section focuses more on the technical description of how the various radiative forcings are calculated in the climate model.

RF_{inst} can be calculated with a single simulation by performing two radiative transfer calls – one with and one without perturbation at each time step (radiation double calling technique). The radiation calls are set up in a backward configuration (see Sect. 3.2.1). Thus the main radiative transfer calculation, which impacts the simulation, is performed with perturbation (model runs in perturbed state). In parallel, a second radiative transfer

calculation is executed but with the perturbation (contrail cirrus or CO_2) removed. It is important to note that the second radiative transfer calculation is purely diagnostic and has no effect on the dynamics and physics in the model (Stuber et al., 2001). Note that the ECHAM5-CCMod CO_2 simulations were performed after the forward approach, which was later changed to the backward approach in the EMAC-CCMod CO_2 simulations to be more consistent with the contrail cirrus simulations. In ECHAM5-CCMod (EMAC-CCMod) radiation calls are performed every 60 min (45 min). If the net radiative fluxes at TOA of both radiative transfer calculations ($E_{net,\,perturbed}$ and $E_{net,\,unperturbed}$) are subtracted, the radiative forcing is yielded:

$$RF = E_{net,\,perturbed} - E_{net,\,unperturbed} \qquad [W\,m^{-2}] \tag{3.1}$$
$$(\,E_{net} = E_{\downarrow} - E_{\uparrow})$$

With $E_{\downarrow}$ the incoming and $E_{\uparrow}$ the outgoing radiative flux at TOA of the respective radiative transfer call. In complete analogy, RF_{adj} is determined with the radiation double calling technique by a single simulation. However, RF_{adj} accounts for temperature adjustments in the stratosphere, which is realized in the second diagnostic radiative transfer calculation adopting the method described by Stuber et al. (2001). As both radiative transfer calculations rely on the same physical background conditions, the statistical uncertainties are small for RF_{inst} and RF_{adj} and a simulation length of 5 years was sufficient. RF_{adj} has been the metric of choice for previous contrail radiative forcing studies with the ECHAM5 model (Marquart et al., 2003; Ponater et al., 2005; Burkhardt and Kärcher, 2011; Bock and Burkhardt, 2016b, 2019).

In contrast to both conventional RFs (RF_{inst} and RF_{adj}), the ERF can no longer be determined by a single simulation. Two independent simulations, one with and one without perturbation, are needed to achieve the full development of all rapid radiative adjustments (RA). The ERF is then calculated by substituting the net radiative flux at TOA of both simulations into Eq. 3.1.

To suppress the slow feedbacks that are not to be included in ERF, reference and perturbed simulation are performed fixing the lower boundary (in an ideal case) with constant surface temperature (Hansen et al., 2005). For technical reasons only the sea surface temperature is kept constant, as fixed land surface temperatures often cause conflicts with the convection parameterization. The simulations presented here use sea surface temperatures from a climatology by Rayner et al. (2003). The whole technique is also known as fixed sea surface temperature (FSST) method and is strongly recommended by Forster et al. (2016) to calculate the ERF. The simulations to determine RF_{inst} and RF_{adj} are based on the FSST setup as well to ensure a quasi-stationary climate state.

In recent years, the ERF has become well established in climate research and depicts the definition of choice since the 5th IPCC Assessment Report (IPCC, 2013). Due to both radiative transfer calculations relying on two independent simulations, the statistical uncertainties are larger than for RF_{inst} and RF_{adj}, determined with the radiation double calling technique. A simulation length of 30 years was needed, for the reference and perturbed simulations, respectively, to obtain a statistically significant ERF. An alternative approach to

calculate ERFs, with largely reduced statistical uncertainties, is available by applying the nudging method in FSST simulations (e. g. Chen and Gettelman, 2013). Nudging means that certain variables in the model (e. g. pressure or wind) are specified by climatologies to synchronize the reference and perturbed simulation. However, the free-running FSST approach was preferred because it is unclear whether the RAs fully develop in a nudged setup (Forster et al., 2016).

The ERF can also be derived from simulations with interactive ocean by regressing the TOA radiative flux against the global mean surface temperature change. This should result in a regression line similar to the light blue line in Fig. 2.4, whose intersection with the y-axis determines the ERF. The method is also known as Gregory regression method (Gregory et al., 2004). However, statistical uncertainties are even larger in this case than for the FSST method (Ponater et al., 2012; Forster et al., 2016) and did only lead to significant results for a CO_2 doubling in the present thesis, but not for the relatively small contrail cirrus perturbation.

3.1.5 Mixed-layer ocean

The sea surface temperatures of the FSST simulations are predefined by a climatological seasonal cycle of observed data (Rayner et al., 2003, see also Sect. 3.1.4). In order to simulate the full surface temperature reaction of a perturbation, sea surface temperatures need to be interactive as well. To achieve this, an ocean module needs to be coupled to the climate model. The surface temperature change simulations were performed exclusively with the EMAC model, which already provides a ready-to-use and extensively tested mixed-layer ocean (MLO) sub-model (Dietmüller et al., 2014; Stecher et al., 2021). The MLO sub-model was implemented by Kunze et al. (2014) and is based on the code of Roeckner et al. (1995).

The MLO has a constant depth of only 50 m, which ensures a sufficiently fast response, in order to keep simulation length and computing times within reasonable limits. As exchange with the deeper ocean layers is not covered by the MLO, a new equilibrium state is reached much more swiftly than for full ocean modules (e. g. Li et al., 2012a). The transient phase, which describes the time span where the perturbation is introduced until a new stable surface temperature is reached, turned out to be about 20 years for the simulations of the present thesis.

Conceptually, the MLO module requires a correction of the surface radiative fluxes which affect the ocean. If the reference FSST simulation is used as initial state for the reference MLO simulation, sea surface temperatures change because the radiative imbalance of the reference FSST simulation usually never becomes completely zero (at least not locally). Thus the climate state of the MLO simulation moves away from that of the FSST simulation, even if no perturbation has been introduced yet. This, first, underlines the importance of tuning, so that an acceptable radiative imbalance lower than $\pm 0.5\,\mathrm{Wm^{-2}}$ can be obtained. To remove the effect of this remaining radiative imbalance, Sausen et al. (1988) introduced the so called flux correction for coupled ocean-atmosphere models. The flux correction is calculated from the net surface energy budget for each grid box of the

reference FSST run. In the MLO simulations, the flux correction is then subtracted from the radiative flux, which is transferred to the ocean. Overall this results in an ocean temperature reacting to the perturbation only, without being affected by the radiative flux imbalance, introduced by the FSST climatology. Ideally, the physical background of the reference FSST simulation then corresponds to those of the reference MLO simulation.

3.2 Feedback analysis

As explained in Sects. 2.6 and 2.7 rapid radiative adjustments (RA) explain the difference between the various radiative forcings, while the slow feedbacks (SF) balance the remaining flux imbalance to regain radiative equilibrium. Both feedback types (RA and SF) can be calculated by feedback analysis methods.

In most studies the kernel method has been chosen, mainly for reasons of computational efficiency (Vial et al., 2013; Zelinka et al., 2013; Smith et al., 2018). However, the application to large perturbations is problematic, since a linear response of the radiative flux change is assumed and saturation effects are not captured. Another problem arises when feedbacks are based on more than just one physical quantity, as applicable for the cloud feedback, which is dependent on cloud cover, IWC and ICNC. In this case the calculation is no longer straightforward (Zelinka et al., 2012), which explains why most of the studies derive the cloud feedback from the cloud radiative effect (CRE).

3.2.1 Partial radiative perturbation method

The merits of radiative feedback analysis in explaining the global forcing-response relationship lie in its ability to identify individual processes and parameters that play a crucial role for the net response. The importance of processes may vary for different forcing agents (e. g. Modak et al., 2016; Rieger et al., 2017; Smith et al., 2018; Colman and Soden, 2021). Since cloud effects are in focus of the present thesis, the partial radiative perturbation (PRP) method was preferred over the kernel method for calculating the radiative feedbacks (Colman and McAvaney, 1997). The feedback analysis tool applied to the ECHAM5-CCMod simulations was originally developed by Klocke et al. (2013) and extended by Rieger et al. (2017). In the context of the present thesis the feedback analysis tool was further modified to include contrail cirrus. The following feedbacks (RA and SF), depending on the respective physical quantities in brackets, can be calculated:

- Planck feedback (vertically constant tropospheric temperature)
- lapse-rate feedback (tropospheric temperature gradient)
- stratospheric temperature feedback (stratospheric temperature)
- water vapor feedback (water vapor mixing ratio)
- cloud feedback (cloud cover and cloud microphysical properties)

- albedo feedback (surface albedo)
- aerosol feedback (aerosol optical properties) [only for EMAC-CCMod simulations]

The PRP method determines feedbacks by an exact re-calculation of the radiative fluxes. For this purpose, all variables of the underlying simulations that are relevant for a radiation call were stored. For the PRP analysis of the ECHAM5-CCMod (EMAC-CCMod) simulations, a timestep length of 12 h (5 h) was chosen. In general RAs can be determined if data of the FSST simulations is substituted into the feedback analysis tool. If substituting data from the MLO simulations, on the other hand side, a combination of SF and RA is yielded. To derive SF exclusively, the RA calculated from FSST simulations need to be subtracted from the feedbacks calculated from the MLO simulations. The feedbacks are determined as follows, by combining a forward and backward calculation:

$$\Delta R_i^{\text{forward}} \;=\; R(x_i^{\text{exp}},\; x_j^{\text{ref}}) \;-\; R(x_i^{\text{ref}},\; x_j^{\text{ref}}) \tag{3.2}$$

The forward calculation, for the respective feedback i, consists of a difference of two radiative flux calculations (R). The variables x correspond to the respective physical quantities used in the radiative transfer calculations. Index i refers to the physical quantities, that determine the feedback to be calculated (e. g., water vapor mixing ratio in case of the water vapor feedback). Index j address the remaining physical quantities. The exponent of x indicates the source of the physical quantity (reference run or experiment). Both radiative transfer calculations are almost completely based on physical quantities of the reference run. Only the physical quantity responsible for the feedback itself is replaced in the first radiative transfer calculation by that from the experiment (x_i^{exp}). In this manner, the radiative flux change of the respective feedback can be determined based on the change of the associated physical quantity. If the physical quantities of the FSST simulations are used, the feedback analysis is also capable for direct determination of the instantaneous radiative forcing (RF_{inst}). For this purpose, the contrail cirrus physical quantities or, respectively, the CO_2 concentrations are substituted into x_i^{exp}.

Rieger et al. (2017), among others, have shown that the forward calculation is not sufficient to determine the feedbacks in a way to balance the radiative forcing exactly. For this reason, the feedbacks in the present thesis were determined from a combination of forward and backward calculations (centered):

$$\Delta R_i^{\text{backward}} \;=\; -\Big[R(x_i^{\text{ref}},\; x_j^{\text{exp}}) \;-\; R(x_i^{\text{exp}},\; x_j^{\text{exp}})\Big] \tag{3.3}$$

The backward calculation is performed analogously to the forward calculation, but is mainly based on physical quantities of the experiment. Only in the first radiation call the physical quantities relevant for the feedback are replaced by those from the reference run (x_i^{ref}). It is also possible to determine RF_{inst} with the backward calculation. RF_{inst} calculated via the backward feedback analysis corresponds to RF_{inst} determined with the FSST simulations, because the model runs in perturbed state (except for the ECHAM5-CCMod CO_2 simulations, see also Sect 3.1.4).

In a final step, the forward ($\Delta R_i^{forward}$) and backward ($\Delta R_i^{backward}$) part of the feedback are combined to a centered feedback ($\Delta R_i^{centered}$):

$$\Delta R_i^{centered} = 0.5 \cdot \left[\Delta R_i^{forward} + \Delta R_i^{backward} \right] \tag{3.4}$$

Note that the feedback plots (shown later) include RF_{adj} and ERF that were directly determined from the model simulations and not by feedback analysis. As the radiation calls in both climate models are set up analogously to the backward calculation of the feedback analysis partially small deviations arise when forming the budget. Deviations between radiative forcings and feedbacks as well as systematical errors of the feedback analysis method are combined in a residuum term.

Since four radiation calls are required per time step for each feedback, the PRP method costs considerably more computing time compared to the kernel method. However, by using the original perturbation in combination with the centered version of the PRP method, the feedbacks are more precise. Saturation effects are taken into account and – most important – cloud feedbacks can be determined directly.

Similar to the kernel method, feedback analysis tools need to be based on the same radiation code which was used for the simulations to be evaluated. For this reason, the feedback analysis tool applied to the EMAC-CCMod simulations was completely rebuilt as part of the present work. The entire radiation code was duplicated from the EMAC model, so that the radiative fluxes can be re-calculated with maximum accuracy. In order to consider all processes relevant for radiation, the EMAC feedback tool was extended by an aerosol feedback. The aerosol feedback exclusively describes the radiative impact of aerosol distributions, which are interactively simulated by the MADE3 aerosol module. Aerosol-cloud interactions where not addressed explicitly here.

Bickel et al. (2020) found substantial deviations for some of their forward and backward PRP feedback calculations (see their appendix). That might lead to systematic disagreements when comparing PRP results to those derived with the kernel method as the latter one is set up in a way that corresponds only to the forward calculation. However, in the meantime new insights about these large deviations could be gained and are described in Appendix C.

3.3 Simulation strategy

In the present thesis, the climate impact of contrail cirrus is assessed in terms of radiative forcing and surface temperature change. For this purpose, two different types of climate model simulations were utilized (FSST and MLO simulations). This section gives a brief overview of the performed simulations, their aims and the applied evaluation methods. Furthermore the utilized air traffic dataset, which represents the basis for contrail cirrus formation, is described.

3.3.1 Air traffic inventory

As explained in Sect. 3.1.3 the contrail cirrus parameterization CCMod uses air traffic density and water vapor emissions to initiate contrail formation. These emissions have been provided by the Aviation Environmental Design Tool (AEDT) air traffic inventory (Wilkerson et al., 2010). The simulations performed as part of the present thesis utilize the AEDT dataset for a future scenario of the year 2050, with a monthly resolution, without diurnal cycle.

Fig. 3.1 shows the respective distributions of covered air traffic volume in terms of flown distances. The associated distribution of water vapor emissions looks almost identical. Overall about 156×10^9 km of track distance and 1.155×10^{12} kg of water vapor emissions are projected for the year 2050. Compared to a CO_2 perturbation, which is homogeneously distributed through the entire atmosphere, air traffic is spatially distributed strongly non-uniformly. Maxima can be found over Europe, the USA, Japan and the eastern part of China. As calculated from the air traffic dataset about 92 % of the air traffic takes place over the northern hemisphere. Due to the significantly higher cruise altitudes projected for the year 2050 about 64 % of the water vapor are emitted above 314 hPa. Contrail cirrus predominantly follow these distributions as their lifetime is usually not extending the timescale of one day.

3.3.2 Performed simulations

3.3.2.1 Fixed sea surface temperature simulations

The first series of simulations for the present thesis was performed with the ECHAM5-CCMod model as used by Bock and Burkhardt (2016b, 2019) to determine ERF results with optimal consistency with previous work. The relatively small contrail cirrus radiative forcings, in combination with large uncertainties introduced with the FSST method to derive ERFs, required a scaling of the underlying air traffic dataset in order to derive statistically significant results, not only for ERF but also for the various RA parameters.

A complete listing of all performed simulations and the corresponding simulation length is provided in Table 3.1. Contrail cirrus simulations, yielded with differently scaled air traffic, are marked as ATR followed by the scaling factor (e. g. ATR-4 for a contrail cirrus simulation with a 4 times increase of the underlying air traffic dataset). In order to get a general feeling for the consequences of scaling for contrail and climate parameters, a set of multiple scaling experiments was performed with the ECHAM5-CCMod FSST setup. RF_{adj} was calculated for ATR-1, ATR-2, ATR-4, ATR-6, ATR-8, ATR-10 and ATR-12. Associated ERF simulations were performed for ATR-1, ATR-4, ATR-8 and ATR-12. As explained in Sect. 2.8 the climate impact of a forcer is often specified relative to a CO_2 perturbation. For this reason the ATR-4, ATR-8 and ATR-12 simulations were accompanied by CO_2 simulations with a corresponding CO_2 increase. The CO_2 concentrations

[†]Tropopause heights illustrated in the present thesis are derived according to the WMO definition, based on model simulation output (Stuber et al., 2001; Reichler et al., 2003)

were chosen so that the RF_{adj} of the ATR simulations matches the RF_{adj} of the respective CO_2 simulation*: ATR-4: +25.5 ppmv CO_2, ATR-8: +37 ppmv CO_2, ATR-12: +45 ppmv CO_2. The corresponding CO_2 increase simulations are marked as CO_2 followed by the scaling factor of the ATR simulation that is targeted (e. g. CO_2-8 for the +37 ppmv CO_2 simulation that aims to reproduce the RF_{adj} of ATR-8). The CO_2 simulations mentioned

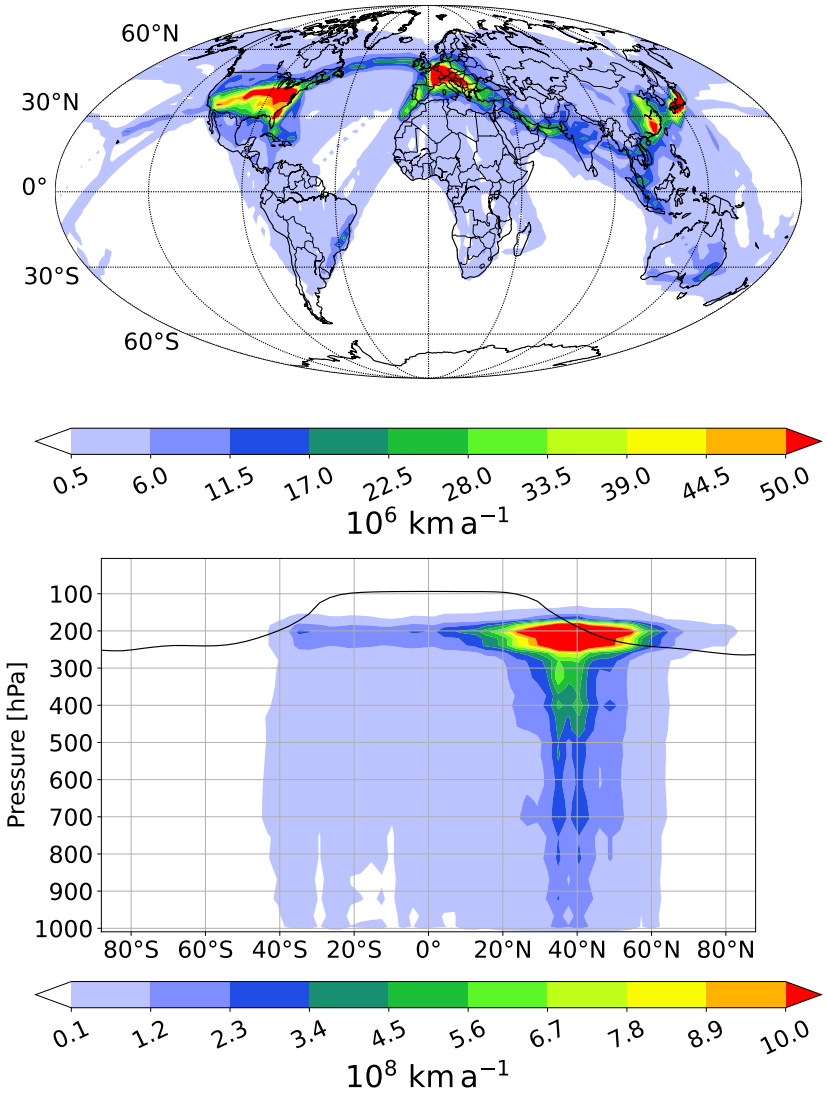

Figure 3.1: Global distribution of the air traffic volume at 240 hPa (top) and as zonal mean vertical cross section (bottom) of the AEDT air traffic dataset for the year 2050 (Wilkerson et al., 2010). This dataset formed the basis for all contrail cirrus simulations of the present thesis. The black solid line in the bottom plot depicts the climatological tropopause height†.

*Note that the CO_2 increases used for the CO_2 simulations of the present thesis have nothing to do with the actual CO_2 increase induced by aircraft emissions

Table 3.1: Overview of all performed simulations and the corresponding simulation length. Contrail cirrus simulations are labeled as ATR followed by the factor of air traffic scaling. Corresponding CO_2 increase simulations were performed to complement the air traffic scaling simulations and are marked as CO_2 followed by the air traffic scaling that is targeted (for a more detailed description see text). CO_2-2× indicates the CO_2 doubling experiments. Various air traffic scaling experiments and CO_2 increase simulations have been conducted with the ECHAM5-CCMod FSST setup (upper table). EMAC-CCMod FSST were only performed for ATR-12, CO_2-2× and CO_2-12 (middle table). Those perturbations were also used for the surface temperature change simulations with the EMAC-CCMod MLO setup (bottom table). Simulations marked with a star were further analyzed with the PRP feedback analysis.

ECHAM5-CCMod FSST simulations

	Reference	ATR-1	ATR-2	ATR-4	ATR-6	ATR-8	ATR-10	ATR-12	CO_2-4	CO_2-8	CO_2-12	CO_2-2×
RF_{inst}								5 yrs			5 yrs	5 yrs
RF_{adj}		5 yrs	5 yrs	5 yrs	5 yrs	5 yrs	5 yrs	5 yrs	5 yrs	5 yrs	5 yrs	5 yrs
ERF	30 yrs	30 yrs		30 yrs		30 yrs		30 yrs*	30 yrs	30 yrs	30 yrs*	30 yrs*

EMAC-CCMod FSST simulations

	Reference	ATR-12	CO_2-12	CO_2-2×
all RF types	30 yrs	30 yrs*	30 yrs*	30 yrs*

EMAC-CCMod MLO simulations

	Reference	ATR-12	CO_2-12	CO_2-2×
$\Delta T_{surface}$	70 yrs	60 yrs*	60 yrs*	55 yrs*

*analyzed by PRP feedback analysis

above feature relatively small radiative responses and were, for this reason, supported by a CO_2 doubling simulation (CO_2-2×) in order to backup statistics. Corresponding ERF simulations were performed for all CO_2 concentrations as well. Note that the CCMod parameterization is also active for CO_2 simulations, including the saturation adjustment, but with air traffic set to zero. RF_{inst} simulations were only conducted for ATR-12, CO_2-12 and CO_2-2×. A simulation length of 5 years was sufficient for RF_{inst} and RF_{adj} to be statistical significant, while ERF simulations need to be considerably longer (30 years). In order to allow the model to adjust to the added perturbation all simulations were preceded by a spin-up phase of 2 years for RF_{inst} and RF_{adj} simulations and 5 years for ERF simulations.

For the surface temperature change simulations the climate model was changed from ECHAM5-CCMod to EMAC-CCMod. For consistency reasons the simulations to derive RF_{inst}, RF_{adj} and ERF were repeated with the new setup, but only for ATR-12, CO_2-2× and CO_2-12. Note that the CO_2 concentration of CO_2-12, in order to yield the RF_{adj} of ATR-12, is slightly larger for EMAC-CCMod (+56 ppmv).

Furthermore the ATR-12, CO_2-2× and CO_2-12 simulations of both models were analyzed with the PRP feedback analysis in order to determine the RAs. In total 340 years of ECHAM5-CCMod FSST simulations and 120 years of EMAC-CCMod FSST simulations were evaluated for the present thesis. One big advantage of the EMAC/MESSy infrastructure (compared to ECHAM5) is that the three radiative forcings of one perturbation can be determined within one pair of simulations (reference and experiment) with three parallel radiative transfer calculations, which saves a lot of computing time.

3.3.2.2 Surface temperature change simulations

The simulations for determining the contrail cirrus induced surface temperature change were exclusively performed with the EMAC-CCMod model. To allow for changing sea surface temperatures, the SST prescription was replaced by a mixed-layer ocean (see Sect. 3.1.5). The flux correction (described in Sect. 3.1.5), needed for the MLO module, could be derived from the EMAC-CCMod FSST reference simulation.

The MLO simulation series was initialized with the reference simulation running for 10 years in order to ensure a sufficiently long spin-up phase. Based on this last state of the reference run, three perturbed simulations were branched off: ATR-12, CO_2-2× and CO_2-12. Nevertheless, the reference simulation was continued as well, in order to ensure a sufficiently long reference phase for response and feedback analysis. As a reaction to the added perturbations, surface temperatures adapt until radiative equilibrium is restored. For the transient phase, where the surface temperature changes towards the new equilibrium, the simulations had to be run for 20 more years (30 years for CO_2-2× due to the larger perturbation). With the final temperature reached, another 40 years were simulated for ATR-12, CO_2-12 and the reference simulation (25 years for CO_2-2×). All coupled ocean simulations performed within the present thesis were only evaluated from this equilibrium phase after the surface temperature change has been fully evolved and radiative equilibrium has been restored at TOA, meaning that the so called equilibrium surface temperature change is determined.

Combined with the radiative forcings of the EMAC-CCMod FSST simulations climate sensitivity and efficacy parameters can be calculated (see Eq. 2.11 and Eq. 2.12). In addition the EMAC-CCMod MLO simulations were further analyzed with the PRP feedback analysis method in order to derive the SFs. In total 245 years of EMAC-CCMod MLO simulations were evaluated.

Chapter 4

Climate impact of contrail cirrus

4.1 ECHAM5-CCMod results

The results presented in this section* are all derived from the ECHAM5-CCMod model (model description see 3.1.1) with the intention to provide results consistent with Bock and Burkhardt (2016b, 2019). A detailed model evaluation against observations can be found in Appendix A. First, the set of air traffic scaling experiments is described which forms the basis for deriving a significant ERF. Subsequently, the different radiative forcings calculated for contrail cirrus are shown. The subsection closes with the results of the feedback analysis to derive the rapid radiative adjustments (RA) in order to explain the differences between the radiative forcings. The central objective of the present thesis is the identification of differences in the forcing, feedback, and response behavior between contrail cirrus and CO_2. For this purpose, the contrail cirrus scaling experiments and feedback analysis were accompanied by comparable CO_2 increase simulations, and both sets of simulations are discussed in context.

4.1.1 Radiative forcings

Compared to RF_{inst} and RF_{adj}, ERFs derived from free-running simulations with the FSST approach tend to have considerably larger statistical uncertainties (Forster et al., 2016). For this reason it was necessary to scale the underlying air traffic dataset. The contrail cirrus simulations presented in the present thesis are mostly based on the AEDT air traffic dataset for the year 2050, except for two unscaled simulations with the 2006 AEDT air traffic dataset, shown in Appendix A, in order to allow for a fair comparison with recent measurements. Table 4.1 shows all radiative forcings that were calculated with the ECHAM5-CCMod model. In the following, the contrail cirrus simulations are referred to as ATR, followed by the air traffic scaling factor. As CO_2 perturbations are often used as reference in climate science (see Sect. 2.8) and to analyze a potential different behavior to

*large parts of this subsection have already been published in Bickel et al. (2020) and Ponater et al. (2021)

Table 4.1: The table shows all RF_{inst}, RF_{adj} and ERF derived with the ECHAM5-CCMod model (FSST setup). The results are based on different scalings of air traffic and corresponding CO_2 concentrations. The contrail cirrus simulations are abbreviated as ATR, followed by the air traffic scaling factor. The CO_2 increase of CO_2-4, CO_2-8 and CO_2-12 was chosen so that their RF_{adj} match the respective RF_{adj} of the corresponding ATR simulations. Statistical uncertainties are given as 95 % confidence intervals derived from the interannual variability.

Name	CO_2 conc. [ppmv]	air traffic scaling factor	RF_{inst} [Wm^{-2}]	RF_{adj} [Wm^{-2}]	ERF [Wm^{-2}]	$\frac{ERF}{RF_{adj}}$
ATR-1	348	1	-	0.169 ±0.003	0.019 ±0.129	not sig.
ATR-2	348	2	-	0.274 ±0.003	-	-
ATR-4	348	4	-	0.412 ±0.005	0.042 ±0.158	not sig.
ATR-6	348	6	-	0.504 ±0.004	-	-
ATR-8	348	8	-	0.595 ±0.008	0.169 ±0.129	0.28
ATR-10	348	10	-	0.656 ±0.006	-	-
ATR-12	348	12	0.674 ±0.005	0.701 ±0.010	0.261 ±0.102	0.37
CO_2-4	373.5 (+25.5)	0	-	0.403 ±0.000	0.325 ±0.122	0.81
CO_2-8	385 (+37)	0	-	0.576 ±0.001	0.439 ±0.152	0.76
CO_2-12	393 (+45)	0	0.413 ±0.000	0.693 ±0.000	0.617 ±0.108	0.89
CO_2-2×	696 (+348)	0	2.411 ±0.002	4.083 ±0.029	3.548 ±0.124	0.87

contrail cirrus, the ATR scaling experiments were complemented by several CO_2 increase simulations. The CO_2 increase simulations CO_2-4, CO_2-8 and CO_2-12 were performed for direct comparison with ATR-4, ATR-8 and ATR-12 respectively. The respective CO_2 concentrations were chosen so that the RF_{adj} of the CO_2 increase simulations approximately yield the respective RF_{adj} of the corresponding ATR simulations. A standard CO_2 doubling experiment (CO_2-2×) was performed for model evaluation reasons, in order to allow for better comparison with CO_2 results from literature. RF_{inst} simulations were only performed for ATR-12, CO_2-12 and CO_2-2×.

The RF_{adj} and ERF of the ATR and CO_2 increase simulations are shown in Fig. 4.1. RF_{adj} of contrail cirrus (blue solid line) is characterized by very small confidence intervals due to the application of the radiation double calling technique. The increase of RF_{adj} with larger scalings of air traffic is not linear. For example, the RF_{adj} of ATR-12 is only about 4 times larger than for the corresponding unscaled simulation. The origins and consequences of this saturation effect are further discussed in Sect. 5.1. The respective ERFs of contrail cirrus (blue dashed line, Fig. 4.1) are substantially reduced compared to RF_{adj}. As obvious, the confidence intervals of the ERFs are more than one magnitude larger than for RF_{adj}. All ERFs are significantly smaller than their corresponding RF_{adj}, but only the ERFs of ATR-8 and ATR-12 differ significantly from zero, indicating that simulations with lower (or no) scaling are not suitable to yield a reasonably interpretable value for contrail cirrus ERF. Based on those results that provide a sensible relative uncertainty, the contrail cirrus ERF is reduced to 28 % and 37 % of the RF_{adj} value for ATR-8 and ATR-12, respectively. Most important for the central objective of this simulation series: The ERF/RF_{adj} ratio

for ATR-12 is only 42 % of the ERF/RF_{adj} ratio for CO_2-12, indicating that the ERF of contrail cirrus is less than half than that of CO_2 in case that both perturbations induce the same magnitude of RF_{adj}.

As described above, the CO_2 concentrations were chosen so that the RF_{adj} (red solid line, Fig. 4.1) approximately yield the RF_{adj} of the respective ATR simulations. RF_{adj} simulations were performed for CO_2 increases between +25.5 ppmv (CO_2-4, corresponding to ATR-4) and +45.0 ppmv (CO_2-12, corresponding to ATR-12). Overall the related RF_{adj} of ATR and CO_2 are in good agreement. Similar to the ATR simulations, the statistical uncertainties are very small for CO_2. Corresponding ERFs were calculated for CO_2-4, CO_2-8 and CO_2-12 (Fig. 4.1, red dashed line) and are throughout smaller than their respective

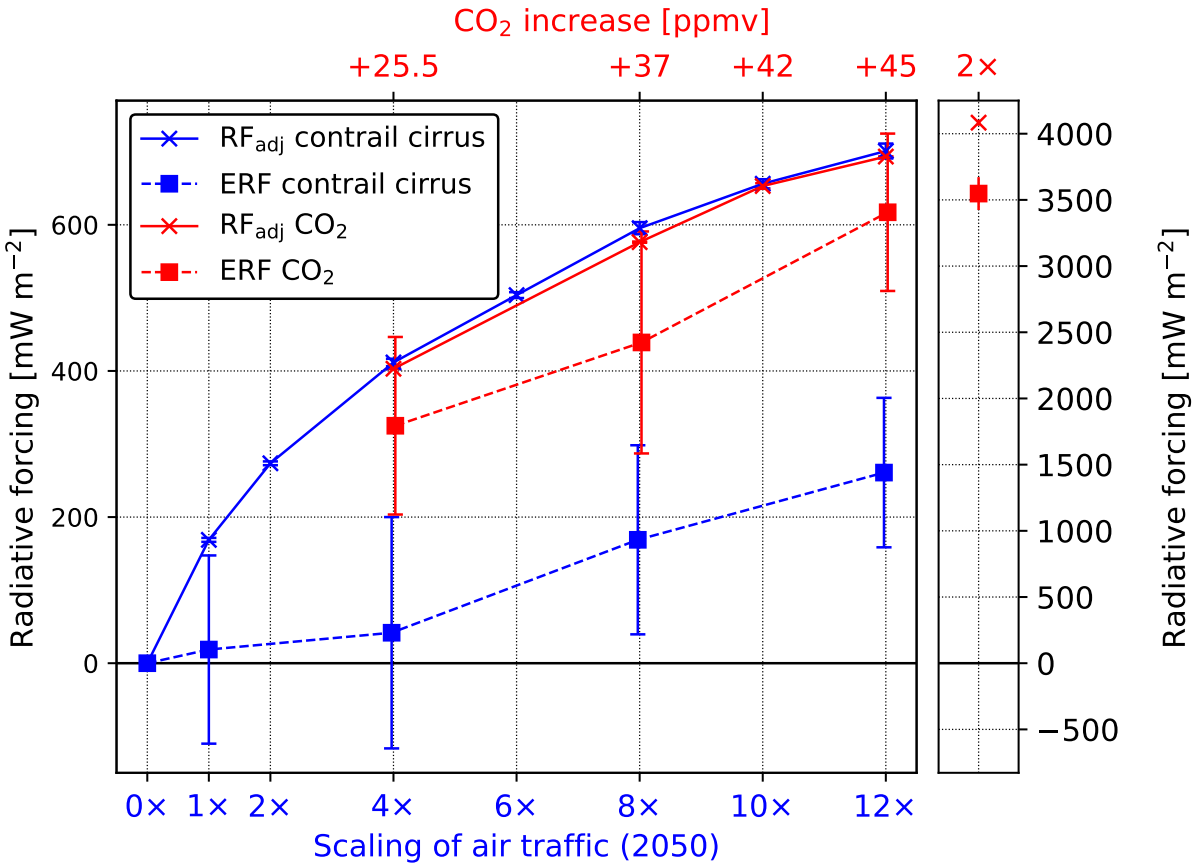

Figure 4.1: Results of the air traffic scaling experiments, derived with ECHAM5-CCMod. RF_{adj} (blue solid line) and ERF (blue dashed line) of contrail cirrus were calculated for different scalings of the AEDT air traffic dataset for the year 2050. The simulations were compared to CO_2 increase experiments with a comparably sized RF_{adj} (red solid line) and corresponding ERF simulations (red dashed line). The associated CO_2 increases are shown on the upper horizontal axis. RF_{adj} and ERF was also calculated for a CO_2 doubling (see right box). Whiskers show the 95 % confidence intervals based on the interannual variabilities. (Source: Bickel et al., 2020)

RF_{adj}. Unlike the ATR case all CO_2 ERFs do significantly differ from zero, but not from their RF_{adj} counterparts. However, the CO_2 doubling simulation (CO_2-2×, right box of Fig. 4.1) makes it plain that the ERF reduction* of the CO_2 simulations is a stable and significant feature. Here the ERF is reduced by about 13 % compared to RF_{adj}, largely consistent with CO_2-12 with a decrease of 10 %.

The ERF reduction, relative to RF_{adj}, is larger for all ATR simulations than for their CO_2 counterparts. The ERF of ATR and CO_2 does only significantly differ for the 12 times scaling, although the significance test only marginally fails for ATR-4 and ATR-8. It is sensible, however, to use ATR-12 and CO_2-12 for further analysis by feedback analysis, in order to explain the different behaviors regarding ERF reduction.

4.1.2 Rapid radiative adjustments

The previous subsection has shown a substantially reduced ERF, compared to RF_{adj}, for the ATR simulations. In this subsection the physical background and the underlying differences to the CO_2 case are addressed. According to the radiative forcing concept (see Sect. 2.6) the physical origin of this feature has to be found in the rapid radiative adjustments (RA). For this reason, ATR-12, CO_2-12 and CO_2-2× have been analyzed with the PRP feedback analysis (see Sect. 3.2.1 for scientific and technical background) to determine the RAs.

Fig. 4.2 shows the results of the feedback analysis for ATR-12. In line with the theoretical concept, if all RAs (left box) are added to RF_{adj} (middle box), the ERF (right box) is yielded. Note that RF_{adj} is shown here instead of RF_{inst}, meaning that the main effect of the stratospheric temperature RA is already included in RF_{adj}. The stratospheric temperature RA can be derived by subtracting RF_{inst} from RF_{adj} (see Table 4.1), resulting in $+27\,\mathrm{mWm^{-2}}$ for ATR-12. As known from Dietmüller et al. (2016), the stratospheric temperature RA is small for contrail cirrus. The remaining stratospheric temperature RA depicted in Fig. 4.2 is related to the set of feedbacks revealed by the PRP method, not to the contrail cirrus forcing. The residuum explains the remaining difference between RF_{adj} and ERF, which can never be fully closed by PRP feedback analysis as a consequence of deviations from linearity (e. g. Boer and Yu, 2003b; Rieger et al., 2017).

As only SSTs are held fixed in the applied FSST method the surface temperature slightly increases by about +0.012 K for ATR-12, resulting in a nonzero Planck RA. However, the Planck RA, as well as the surface albedo RA hardly contribute to total RAs. The remaining RAs (except for the surface albedo RA) are much more substantial and also statistically significant. The water vapor RA and the lapse rate RA are largely dependent on tropospheric temperature changes. The sum of both RAs yields $+24\,\mathrm{mWm^{-2}}$, meaning that they almost compensate each other. Hence, the natural cloud RA is largely responsible for the reduced ERF. With $-391\,\mathrm{mWm^{-2}}$ it almost equals the total ERF reduction

*The term "ERF reduction" or "reduced ERF" is used in the present thesis to refer to an ERF that is smaller than the associated RF_{adj}

of -413 mWm^{-2}. The residuum turns out to be quite small, which confirms a consistent feedback analysis.

The RAs can be explained by changes in underlying physical quantities. Fig. 4.3 shows zonal mean vertical cross sections of the differences between ATR-12 and the reference ERF simulation for some key variables. Their patterns generally show some resemblance to the air traffic density pattern (see Fig. 3.1). The temperature change (Fig. 4.3 c) indicates a dipole structure, typical for the response to added absorbing perturbations, with warming below and cooling above contrail cirrus cover (Ackerman et al., 1988; Ponater et al., 2005). While the maximum amount of warming can be found directly below the main flight levels, the temperature increase gets smaller towards the surface and becomes almost zero on the ground per construction (FSST). Overall the temperatures in the troposphere (below the tropopause, see black solid line in Fig. 4.3 c) are increasing. Thus LW emission to space is increased, which results in a negative global mean lapse rate RA. In contrast, the temperature in the lowermost stratosphere region is slightly decreasing. The cooler levels emit less LW radiation, leading to the positive stratospheric temperature RA described above. Directly connected to tropospheric temperature is the amount of water vapor which can be carried by air. As a consequence of rising temperatures in the troposphere, the specific humidity increases (see Fig. 4.3 d). The regions with the largest increase of

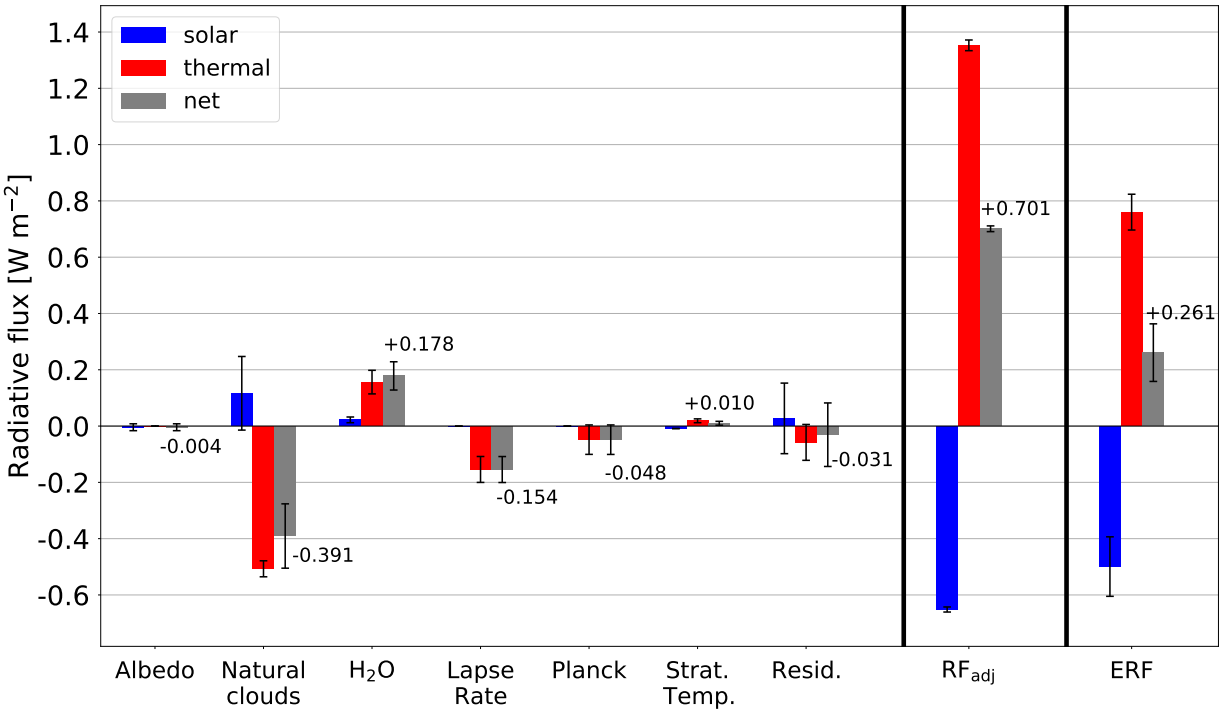

Figure 4.2: Rapid radiative adjustments (RA) derived by feedback analysis of the ATR-12 ECHAM5-CCMod FSST simulation (left box). The respective radiative fluxes (gray bars) are separated into a shortwave part (blue bars) and a longwave part (red bars). Whiskers show the 95 % confidence intervals based on the interannual variabilities.

specific humidity, between 0° and 30°N, are deviating from the maximum temperature increase around 40°N. Nevertheless, temperatures are also increasing in those regions with largest specific humidity increase, however only by about 0.05 K and thus not visible in the figure. The southward shift of maximum specific humidity increase (relative to maximum temperature increase) might be induced by larger absolute temperatures in the tropics, related to a stronger increase of saturation water vapor with temperature. As water vapor is a greenhouse gas, an increased specific humidity results in less emitted LW radiation, leading to a positive water vapor RA. It is common in feedback analysis to find the

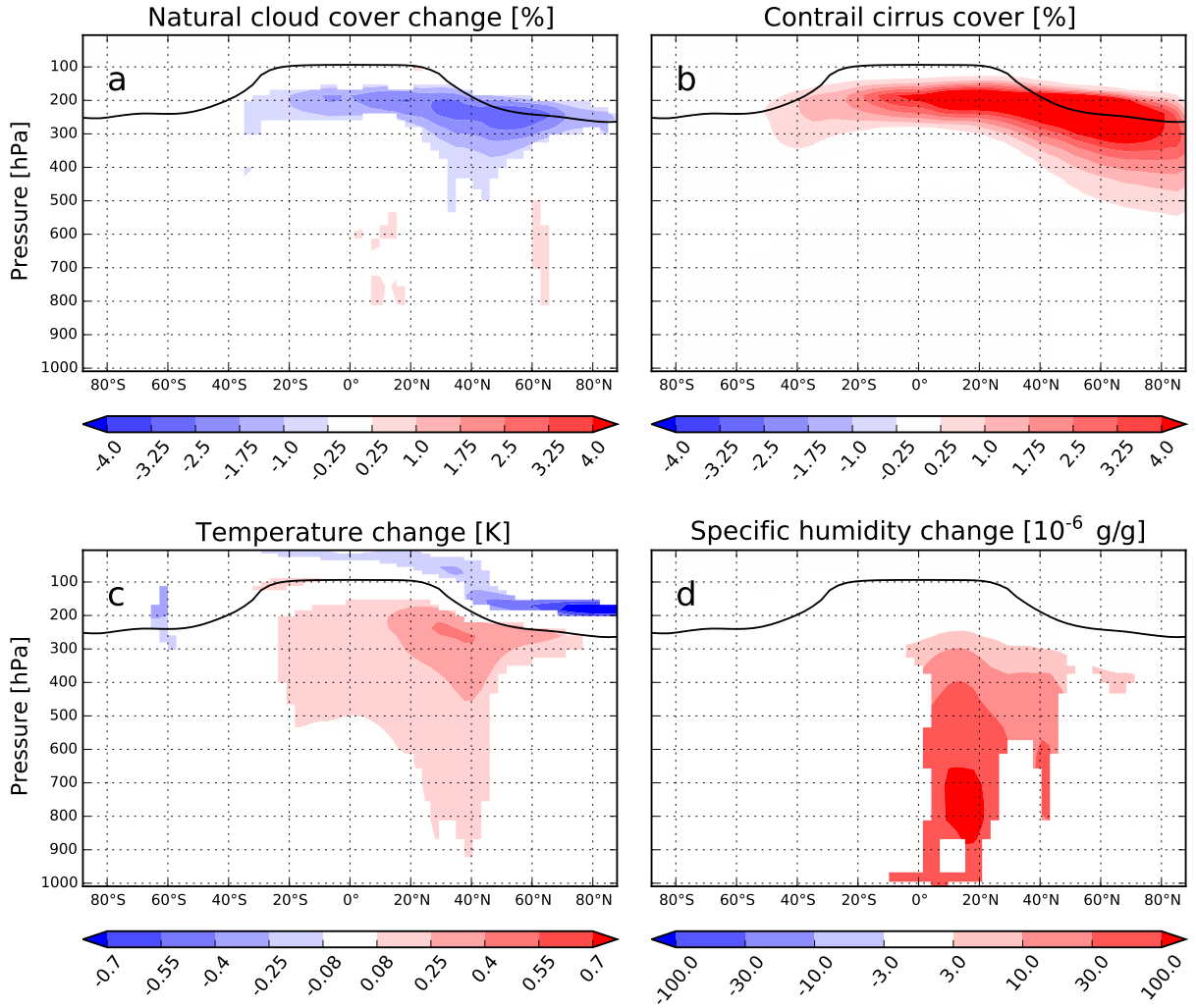

Figure 4.3: Zonal mean vertical cross section of natural cloud cover change (a), contrail cirrus cover (b), temperature change (c) and specific humidity change (d) for the ECHAM5-CCMod ATR-12 FSST simulation. The black solid line shows the climatological tropopause height. Data is only plotted for areas where the deviation from the reference simulation is significant at the 99 % confidence level.

negative lapse rate RA associated with an overcompensating positive water vapor RA (e. g. Vial et al., 2013).

As said, the natural cloud RA represents the largest negative contribution, resulting in an ERF which is substantially reduced relative to RF_{adj} for ATR-12. Natural cloud cover (see Fig. 4.3 a) decreases predominantly where contrail cirrus cover forms (see Fig. 4.3 b). Thus contrail cirrus cover increase is partly compensated by a decrease of natural cirrus cover. This damping effect is mainly induced by a limited amount of available supersaturated water vapor in the atmosphere, for which cirrus clouds and contrail cirrus are competing during their formation. For example, at 220 hPa a contrail cirrus cover of +3.5 % faces a loss of natural cirrus cover of -1.4 % (absolute percentage points). The decrease of natural cloud cover is the main reason for the negative natural cloud RA and, in turn, is mainly responsible for the reduced ERF. It is important to note, that the compensation effect is amplified by scaling, to some small extent (for further details see Sect. 5.1).

In a next step it is pointed out why the ERF reduction of CO_2-12 is much weaker than for ATR-12. Fig. 4.4 shows the RAs calculated with the PRP feedback analysis for CO_2-12. Again, if all RAs (left box) are added to RF_{adj} (middle box), ERF (right box) is yielded. Due to the small RF_{adj}, scaled to ATR-12, the RAs are not significantly different from zero, except for the Planck RA. However, the calculated RAs for CO_2-2×

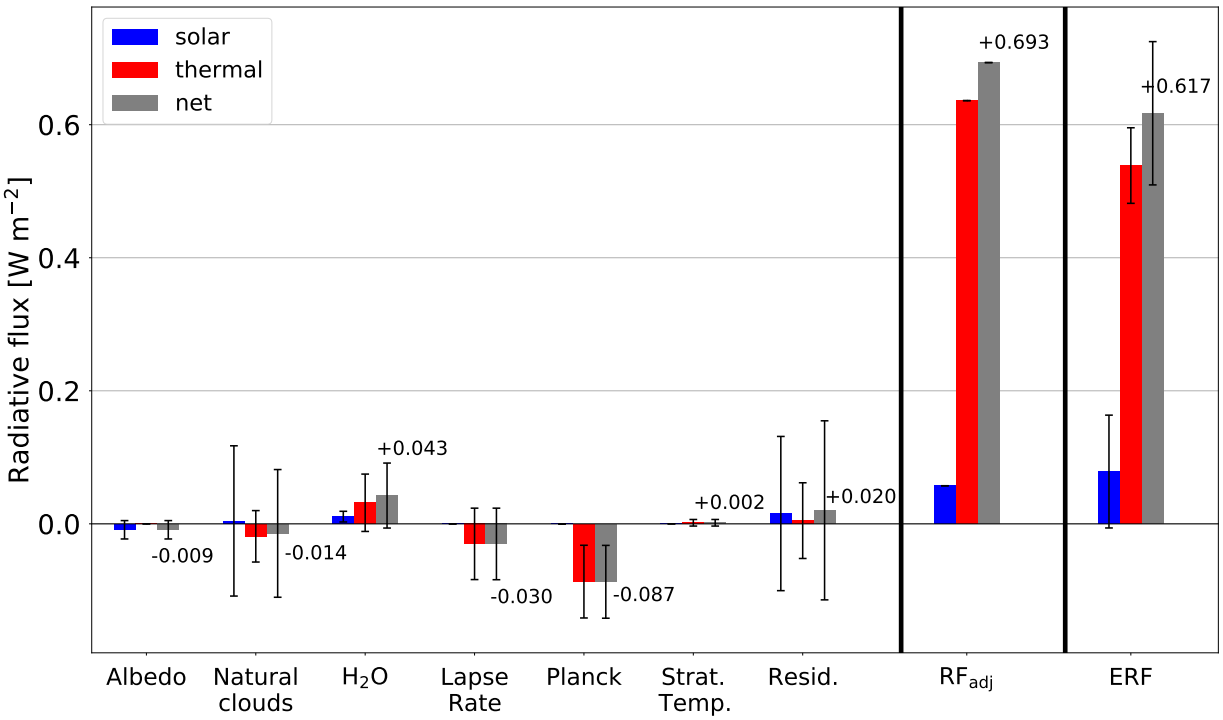

Figure 4.4: Rapid radiative adjustments (RA) derived by feedback analysis of the CO_2-12 ECHAM5-FSST simulation (left box). The respective radiative fluxes (gray bars) are separated into a shortwave part (blue bars) and a longwave part (red bars). Whiskers show the 95 % confidence intervals based on the interannual variabilities.

are significant and their relative amount is in general largely consistent with those of CO_2-12 (see Fig. C.1). For this reason, and as we prefer to compare ATR-12 and CO_2-12 for optional consistency, the feedback analysis of CO_2-12 is shown here, in spite of the RAs being much less significant. A description of the statistically more significant results of CO_2-2× can be found in Bickel et al. (2020, see their Fig. 6b).

For CO_2 perturbations the difference between RF_{inst} and RF_{adj} is known to be large, and the latter is generally considered as the more sensible choice (Hansen et al., 2005, see also Sect. 2.6). By definition the CO_2 induced stratospheric temperature RA is already included in RF_{adj}. The very small remaining part shown in Fig. 4.4 originates (as in the contrail cirrus case) from other rapid adjustments (e. g., from water vapor) revealed by the PRP feedback analysis. The cloud RA is negative but turns out to be smaller than for CO_2-2×, if scaling is considered. Consistent with CO_2-2×, the cloud RA features the largest statistical uncertainties. The underlying distributions of natural cloud cover change of both CO_2 experiments are comparable. An increase of low cloud cover in the tropics was found to be the main reason for the negative cloud RA (not shown). As for ATR-12 and consistent with literature the water vapor RA is exceeding the lapse rate RA in magnitude (Vial et al., 2013), but the compensation between both is less distinct than for ATR-12. Temperatures increase throughout large parts of the troposphere with maxima around +0.1 K between 40°S and 50°N, below 700 hPa (not shown). The ERF is reduced for CO_2-12 as well (-76 mWm^{-2}), but considerably weaker than for ATR-12 (-413 mWm^{-2}). With -87 mWm^{-2}, the significantly negative Planck adjustment explains large parts of the reduced ERF in case of CO_2-12. It is induced by a surface temperature increase of +0.025 K, leading to enhanced emission of LW radiation to space.

As described in Sect. 2.6 the Planck RA is often not accounted for in ERF, as adjustments due to surface temperature changes are related to SF. However, as a consequence of the applied FSST method, the Planck RA, due to land surface temperature changes, is included in ERF here. As the Planck RA is determined by feedback analysis, a corrected ERF can be calculated. If the Planck RA is subtracted, a ERF of 704 mWm^{-2} is yielded for CO_2-12, meaning that the ERF reduction disappears. This behavior is also valid for the more significant CO_2-2× simulation (see Bickel et al., 2020, Fig. 6b). For ATR-12 the ERF reduction is slightly reduced if the Planck RA is considered as SF and results in a corrected ERF of 309 mWm^{-2} (instead of 261 mWm^{-2}). Nevertheless, in the following only non-corrected radiative forcings are used for further calculations in order to be consistent with literature results, which are predominantly derived with the FSST method.

4.2 EMAC-CCMod results

The results described in this section are all derived from the EMAC-CCMod simulations (model description see Sect. 3.1.2). To keep the radiative imbalance within limits and enable the later coupling of the MLO, a retuning of the model was required. Further details about the tuning process, including an evaluation against observational data, can be found in Appendix A.

The section starts with a description of the derived radiative forcings. Exploiting what has been learned with respect to statistical significance of the simulation results from the ECHAM5-CCMod scaling experiments, FSST simulations with EMAC-CCMod have only been performed for ATR-12, CO_2-12 and CO_2-2×. Again, the PRP feedback analysis has been applied to those simulations in order to determine the RAs. As the next and main step, corresponding simulations with a coupled MLO have been performed to derive the respective surface temperature changes. Based on these simulations the slow feedbacks (SF) were calculated with the help of the PRP feedback analysis (the technique is the same as for the RAs). By combining the radiative forcings with the surface temperature changes, the climate sensitivity and efficacy parameters were derived for the three perturbations. For a better comparison between ATR-12 and CO_2-12, with respect to their surface temperature response, the respective feedback parameters have also been calculated. Altogether, this section yields a comprehensive compilation of all key climate parameters of contrail cirrus, meeting the main goal of the present thesis. Note that coupled MLO simulations have only been performed with the EMAC-CCMod setup.

4.2.1 Radiative forcings

As learned from the scaling experiments in Sect. 4.1.1, the ERF of contrail cirrus is only significantly different from zero if the underlying 2050 AEDT air traffic dataset is at least scaled by a factor of 8 (see Fig. 4.1). Analogously, RAs are also hard to interpret due to statistical noise for low scalings. Motivated by these findings, FSST simulations with sufficiently strong scaling, to derive the different radiative forcings, have been performed (see Table 4.2). A RF_{adj} of $858\,mWm^{-2}$ has been calculated for ATR-12. With about $568\,mWm^{-2}$, the corresponding ERF is considerably reduced to about 66 %, compared to RF_{adj}. The statistical uncertainty of the ERF is indeed small enough to allow a significant distinction from zero as well as from RF_{adj}. Potentially, significant results might be yielded with a smaller scaling of ATR as well.

Again, following the general concept adopted here, ATR-12 is compared to a CO_2 experiment with a similarly sized RF_{adj}. Increasing the CO_2 concentration by +56 ppmv results in a RF_{adj} of $854\,mWm^{-2}$ and meets the requirements sufficiently well. As for ECHAM5, the simulation series is complemented by a standard CO_2 doubling simulation (CO_2-2×) to facilitate comparison with results from literature but also between the two models used here. Note, for example, that the corresponding ERFs of both CO_2 simulations are larger than the respective RF_{adj} (+21 % for CO_2-12) in contrast to what was found in ECHAM5-CCMod. The statistical uncertainties of the ERF, derived for CO_2-12, allow for significant differentiation from zero and also from their respective RF_{adj}. Additionally, the ERF of CO_2-12 is well separated from the respective counterpart of ATR-12. For a further discussion of the results and a comparison between both models see Sect. 5.2.

It may be interesting to some that the radiative impact of contrail cirrus shows a fundamentally different behavior during day and night which offers great potential for mitigation strategies (Stuber et al., 2006; Stuber and Forster, 2007). While contrail cirrus reflects SW and traps LW radiation during day, it only affects LW radiation during night.

Table 4.2: RF_{inst}, RF_{adj} and ERF derived from the EMAC-CCMod FSST simulations. Statistical uncertainties are depicted as 95 % confidence intervals of the interannual variability.

Name	CO_2 conc. [ppmv]	air traffic scaling factor	RF_{inst} [Wm^{-2}]	RF_{adj} [Wm^{-2}]	ERF [Wm^{-2}]	$\frac{ERF}{RF_{adj}}$
ATR-1	348	1	0.187 ±0.003	0.188 ±0.003	-	-
ATR-12	348	12	0.843 ±0.004	0.858 ±0.004	0.568 ±0.125	0.66
CO_2-12	404 (+56)	0	0.553 ±0.001	0.854 ±0.001	1.034 ±0.105	1.21
CO_2-2×	696 (+348)	0	2.919 ±0.001	4.177 ±0.001	4.574 ±0.094	1.10

The AEDT air traffic dataset, utilized here, features no diurnal cycle and thus the different impact on radiative forcing between day and night periods can be fairly evaluated. A grid box is accounted to the night period if the incoming SW radiation at TOA is zero. If subdivided accordingly, a RF_{adj} of 351 mWm^{-2} and 32 mWm^{-2} are yielded for the night and day periods, respectively (based on the ATR-1 simulation). That means, that the climate impact of contrail cirrus, on the basis of RF_{adj}, is about 10 times larger during night. The net RF_{adj} of 191 mWm^{-2} slightly deviates from that shown in Table 4.2 because instantaneous (instead of accumulated) model output was used here in order to exactly distinguish between day and night periods. The ERF derived for day periods even becomes negative, however not significantly different from zero (based on the ATR-12 simulation).

4.2.2 Rapid radiative adjustments

The previous subsection again revealed a smaller ERF relative to RF_{adj} for the ATR simulation. To explain the physical background and differences to the CO_2 case, the PRP feedback analysis has been applied to ATR-12, CO_2-12 and CO_2-2×, in accordance with the ECHAM5-CCMod simulations. With the determined RAs the origin of the ERF reduction can be revealed.

Fig. 4.5 shows the results of the feedback analysis for ATR-12. As for the ECHAM5-CCMod feedback figures, the sum of all RAs (left box) and the RF_{adj} (middle box) yields the ERF (right box). If calculated as the difference of RF_{adj} and RF_{inst} (see Table 4.2), a smaller stratospheric temperature RA of 15 mWm^{-2} is yielded, compared to 34 mWm^{-2} derived by feedback analysis. The remaining difference between both results is depicted as the stratospheric temperature RA in Fig. 4.5. The residuum turns out to be larger, compared to the ECHAM5-CCMod ATR-12 simulation, but is still considerably smaller than the physically relevant RAs (see below). The residuum mainly originates from a different calculation approach of RF_{adj} between the FSST simulations and the PRP feedback analysis. While the RF_{adj} determined with the FSST simulations is based on the backward calculation only, the PRP feedback analysis combines the forward and backward calculation (for further details see Sects. 3.2.1 and 3.1.4). The RF_{adj} calculated from the centered feedback calculation (forward and backward calculation combined) is only 813 mWm^{-2} (not shown in Fig.) and would compensate for large parts of the residuum.

Overall, the ERF reduction of ATR-12 is largely determined by the natural cloud, water vapor and lapse rate RA, while the aerosol, albedo and stratospheric temperature RA do hardly contribute. The non-zero Planck RA is again the result of changing land surface temperatures as a consequence of the applied FSST method. The corresponding global mean surface temperature increase is about +0.011 K and results in an increased emission of LW radiation. Depending on the tropospheric temperature change, the water vapor and lapse rate RA are compensating each other almost perfectly. Thus the natural cloud RA (-249 $\mathrm{mWm^{-2}}$) explains practically all of the ERF reduction of -290 $\mathrm{mWm^{-2}}$. The remaining negative contribution is largely contributed by the residuum, as explained above.

Again, the origin of RAs can be mostly traced back to adaptions of the basic physical quantities. Fig. 4.6 shows the change of the important variables for ATR-12. Going beyond the ECHAM5 analysis and anticipating the discussion of slow feedbacks in the next sections, the radiative fluxes from the EMAC simulations have been analyzed with respect to their vertical profiles to identify those levels from where the respective RA originates. This has been done by decomposition of the RAs into upward and downward fluxes (see Fig. 4.7 for the natural cloud RA of ATR-12).

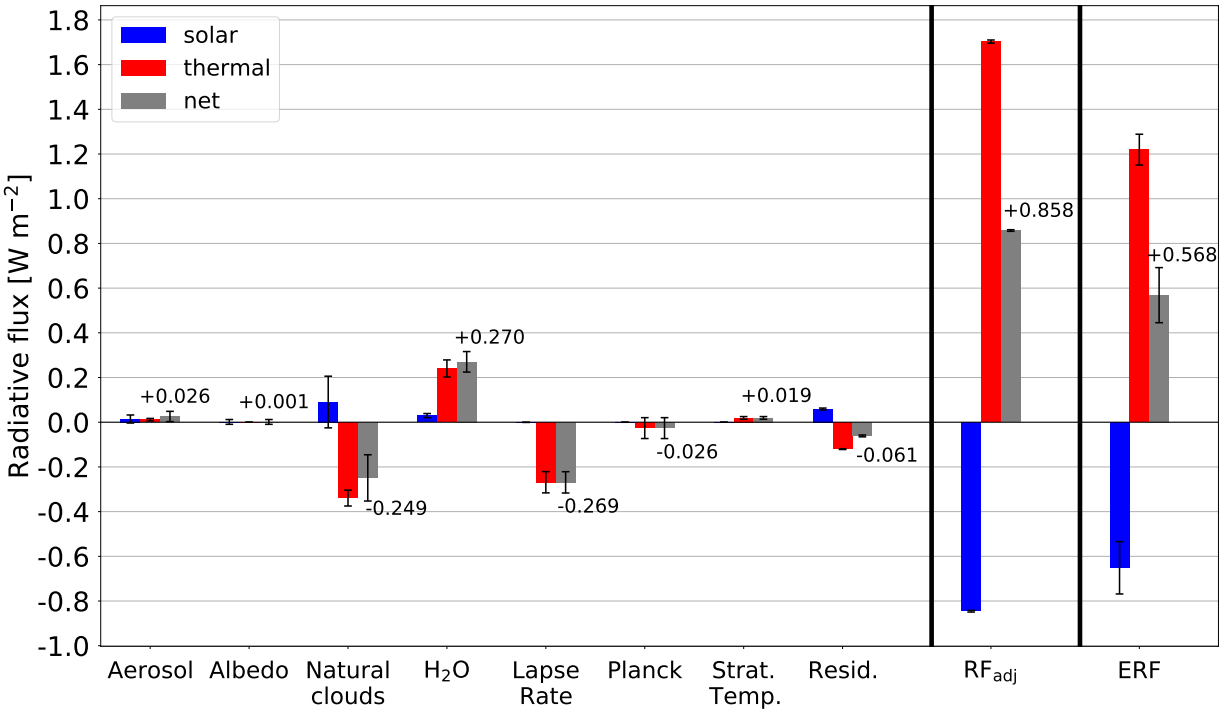

Figure 4.5: Rapid radiative adjustments (RA) determined by feedback analysis of the ATR-12 EMAC-FSST simulation (left box). The respective radiative fluxes (gray bars) are subdivided into a shortwave part (blue bars) and a longwave part (red bars). Whiskers show the 95 % confidence intervals based on the interannual variabilities.

The negative natural cloud RA consists of a large negative LW and smaller positive SW proportion, which is consistent with the inducing reduction of natural cirrus cover (see Fig. 4.6 a). Natural cloud cover decrease overlaps fairly accurate with those regions where contrail cirrus cover occurs (see Fig. 4.6 b), except for latitudes poleward of 70°N, where contrail cirrus is extremely thin due to a low ice water content (see Bock and Burkhardt, 2016b, Fig. 5 and 7). The compensation might again be related to contrail cirrus and natural cirrus competing for the same amount of ambient water vapor, during formation.

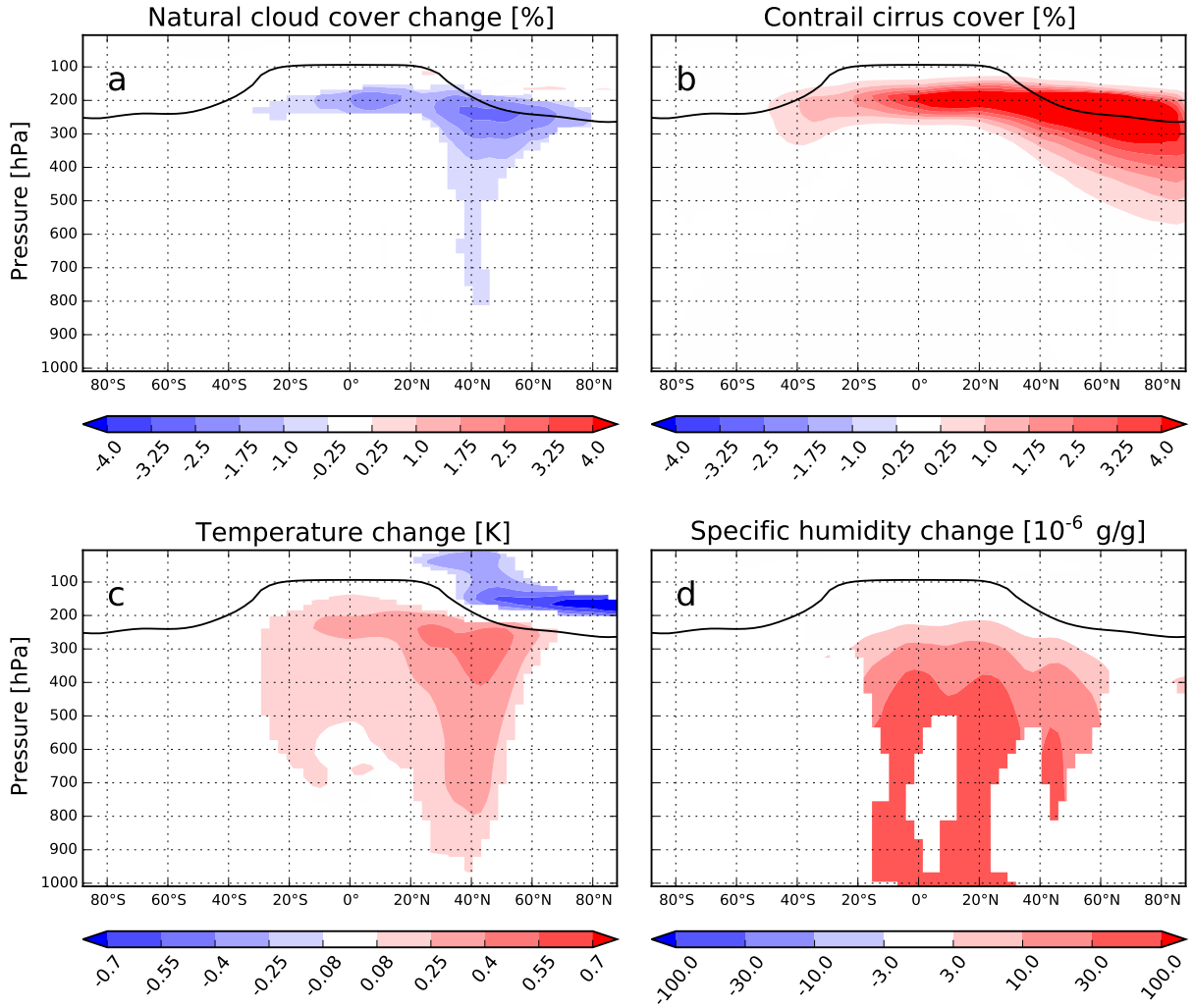

Figure 4.6: Zonal mean vertical cross section of natural cloud cover change (a), contrail cirrus cover (b), temperature change (c) and specific humidity change (d) of the EMAC ATR-12 FSST simulation. The black solid line shows the climatological tropopause height. Data is only plotted for areas where the deviation from the reference simulation is significant to the 99 % confidence interval.

The largest contributions to SW and LW natural cloud RA respectively can be found around 40°N, predominantly corresponding to those regions with most natural cloud cover decrease (see Fig. 4.7, first and second row). Here, the strongest vertical radiative flux gradients can be found, that contribute to the RA, determined at TOA (for a more detailed description refer to the caption of Fig. 4.7). However, if added, both maxima almost cancel out each other, so that the largest negative net contribution (SW + LW) to natural cloud RA can be found between 10°N and 30°N at an altitude between 200 and 500 hPa

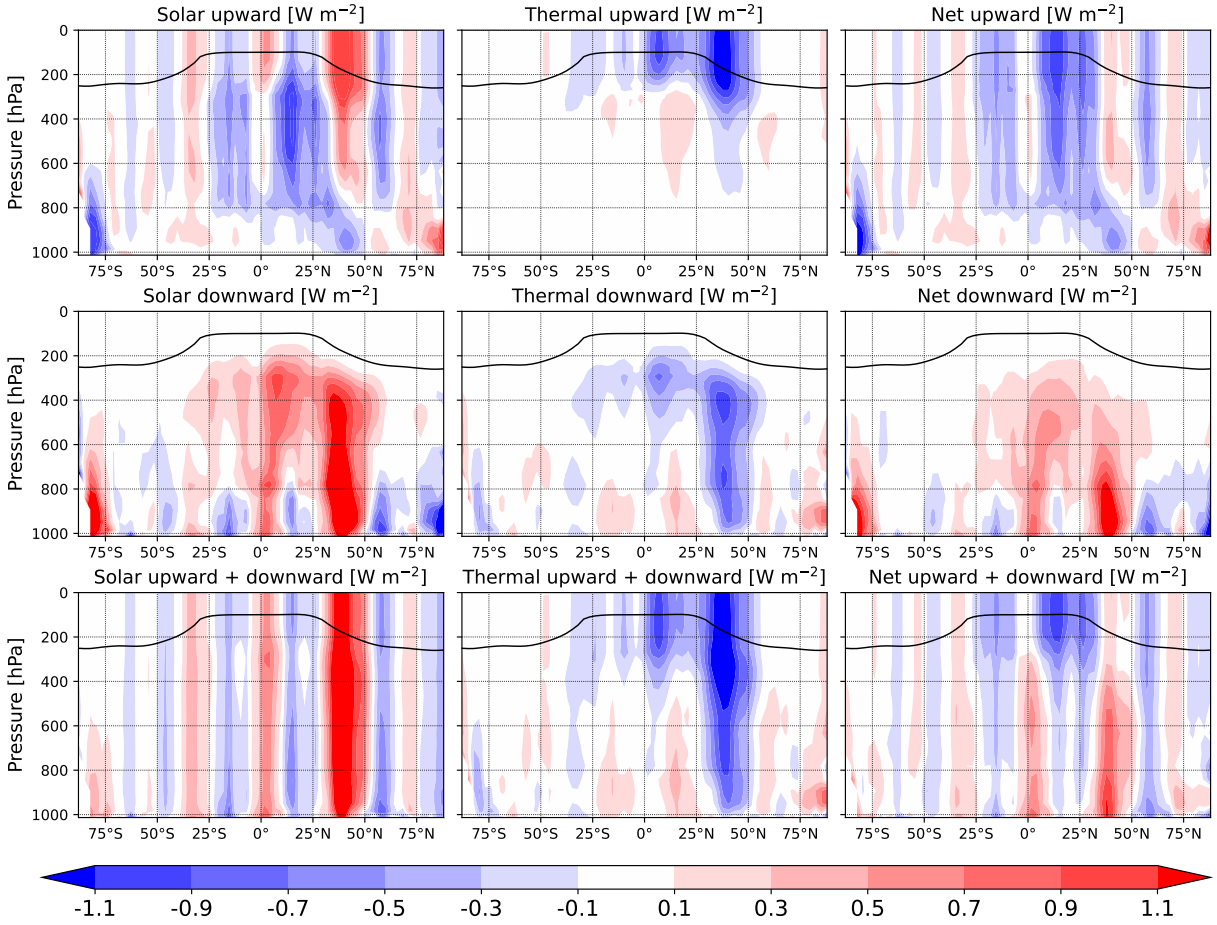

Figure 4.7: Zonal section of the natural cloud RA for ATR-12 subdivided into upward (first row), downward (second row) and combined upward and downward vertical fluxes (third row). The respective fluxes are further decomposed into solar (left column), thermal (middle column) and net fluxes (right column). If averaging the uppermost level, at TOA, of the net, combined upward and downward fluxes (bottom right), the natural cloud RA of -249 mWm^{-2} is yielded. The origin of natural cloud RA formation can be identified with the help of vertical gradients. For example, large parts of the net negative natural cloud RA form between 10°N and 30°N at an altitude between 200 and 500 hPa (see bottom right panel).

(indicated by the strong vertical flux gradients to be noticed in Fig. 4.7, third row). Thus, the maximum contribution to the negative natural cloud RA is considerably shifted to the south in comparison to maximum natural cloud cover reduction (35°N - 55°N).

In addition to ice clouds, changes of lower liquid water clouds do also contribute to the natural cloud RA (see large gradients around 800 hPa in Fig. 4.7, right column). However, the respective structural features are rather noisy and are the reason why the natural cloud RA has the largest uncertainty of all terms (see net upward and downward fluxes of Fig. 4.7 between 600 and 1000 hPa).

The temperature increases below and decreases above those regions with largest air traffic density (compare Fig. 4.6 c with Fig. 3.1). This temperature distribution is typical for contrail cirrus and is often referred to as temperature dipole effect (Ackerman et al., 1988; Ponater et al., 2005). Larger upper tropospheric temperatures result in an increased emission of LW radiation and thus in a negative lapse rate RA. Extended evaluation of the upward and downward fluxes reveals that the main contribution to lapse rate RA originates between 10°N and 30°N (not shown). The inverse physical relation (less emission of LW radiation due to smaller temperatures) explains the positive stratospheric temperature RA.

As seen above, the negative lapse rate RA is completely compensated by the positive water vapor adjustment which is a result of the strong coupling between warming and moistening of air. Significant increased specific humidity between 15°S and 60°N results in a strengthened greenhouse effect (see Fig. 4.6 d). As for the Planck RA, the region between 10°N and 30°N at an altitude between 500 hPa and surface contributes the largest parts to water vapor RA (again retrieved from upward and downward decomposition of the corresponding radiative fluxes, not shown). The positive aerosol RA is caused by an increase of aerosol optical depth over the western Sahara by over 0.05, which extends across the Atlantic ocean to Central America with decreasing impact (not shown here).

Summarizing, the highest contributions to lapse rate and water vapor RA are located considerably south of the air traffic density maximum. In combination with the southward shift of the natural cloud RA, this behavior suggests a considerably stronger sensitivity of the RAs towards the subtropical and tropical regions.

In contrast to ATR-12, an increased ERF was found for CO_2-12, relative to the corresponding RF_{adj}. The enhanced ERF is almost exclusively caused by a positive contribution to the SW radiative flux component. The physical origin was again analyzed by feedback analysis, to derive the RAs, which explain the difference between RF_{adj} and ERF (see Fig. 4.8). Compared to the corresponding ECHAM5 simulations, most RAs are significantly different from zero here. The residuum turns out to be quite small, compared to ATR-12, because there is hardly any difference between the forward and backward RF_{adj}, determined by feedback analysis. Altogether the ERF increase is mainly induced by the natural cloud, water vapor, lapse rate and Planck RA. The relatively large negative Planck RA, is a consequence of rising land surface temperatures due to the applied FSST method (see Sect. 3.1.4). On a global scale, including areas with fixed sea surface temperature, the surface temperature increases by about 0.10 K. The water vapor RA slightly overcompensates the lapse rate RA by 28 mWm^{-2} and thus has a contributing effect to ERF increase, which is a common feature for CO_2 forcing (e. g. Smith et al., 2018). With +201 mWm^{-2},

the natural cloud RA adds by far the biggest contribution and is even larger than the overall difference between RF_{adj} and ERF of $+180\,mWm^{-2}$. In contrast to the water vapor, lapse rate and Planck RA, the natural cloud RA is almost exclusively driven by a SW flux change, corresponding to the SW ERF increase. As explained in Sect. 2.6 and at the end of Sect. 4.1.2, the Planck RA, due to land surface temperature change, is sometimes considered as SF. In that case, an even larger ERF of $1125\,mWm^{-2}$ would be reached.

The RAs of CO_2-12 were also traced back to their physical origin by analyzing the respective upward and downward fluxes (not shown). Again, due to the small radiative forcing some features are only barely significant. However, they can be largely confirmed by CO_2-2×, which overall shows a very similar behavior. Typical for a CO_2 increase experiment, the temperature rise is homogeneously distributed over large parts of the troposphere. Due to its coupling to tropospheric temperature, the specific humidity increase shows a similar distribution. The largest contributions to natural cloud RA can be found between 40°S and 10°S and between 20°N and 70°N. By decomposing the natural cloud RA into an upward and downward component, the vertical origin of the increased ERF can be precisely determined. A reduction of low clouds between 900 and 700 hPa was found to be the main origin, which clearly corresponds to the dominance of the positive SW over the negative LW flux component.

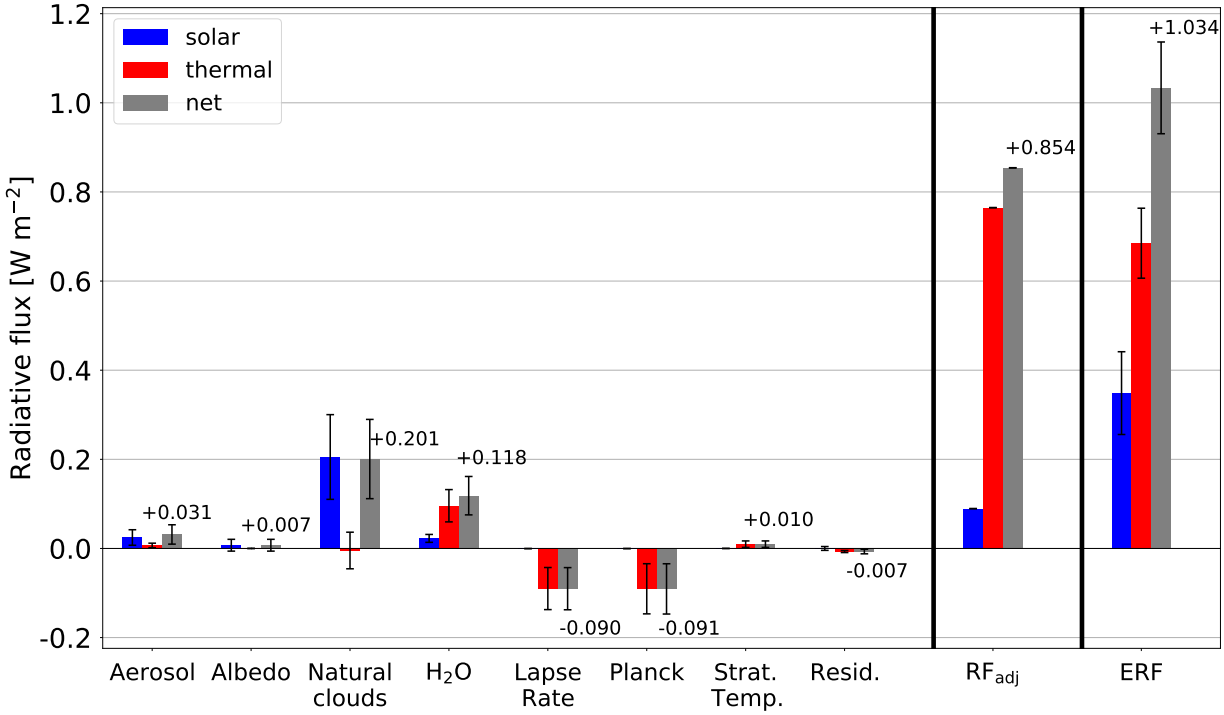

Figure 4.8: Rapid radiative adjustments (RA) derived by feedback analysis of the CO_2-12 EMAC-FSST simulation (left box). The respective radiative fluxes (gray bars) are subdivided into a shortwave part (blue bars) and a longwave part (red bars). Whiskers show the 95 % confidence intervals based on the interannual variabilities.

Overall there is a large degree of consistency in the results of the FSST simulations for ECHAM5-CCMod (Sect. 4.1) and EMAC-CCMod, but also some differences will be pointed out later (Sect. 5.2).

4.2.3 Surface temperature change

Following the general concept of the present thesis the EMAC-CCMod model was used for ATR and CO_2 increase simulations with an interactive ocean (see Sect. 3.1.5), in order to go beyond radiative forcings and address the issue of potential differences in climate

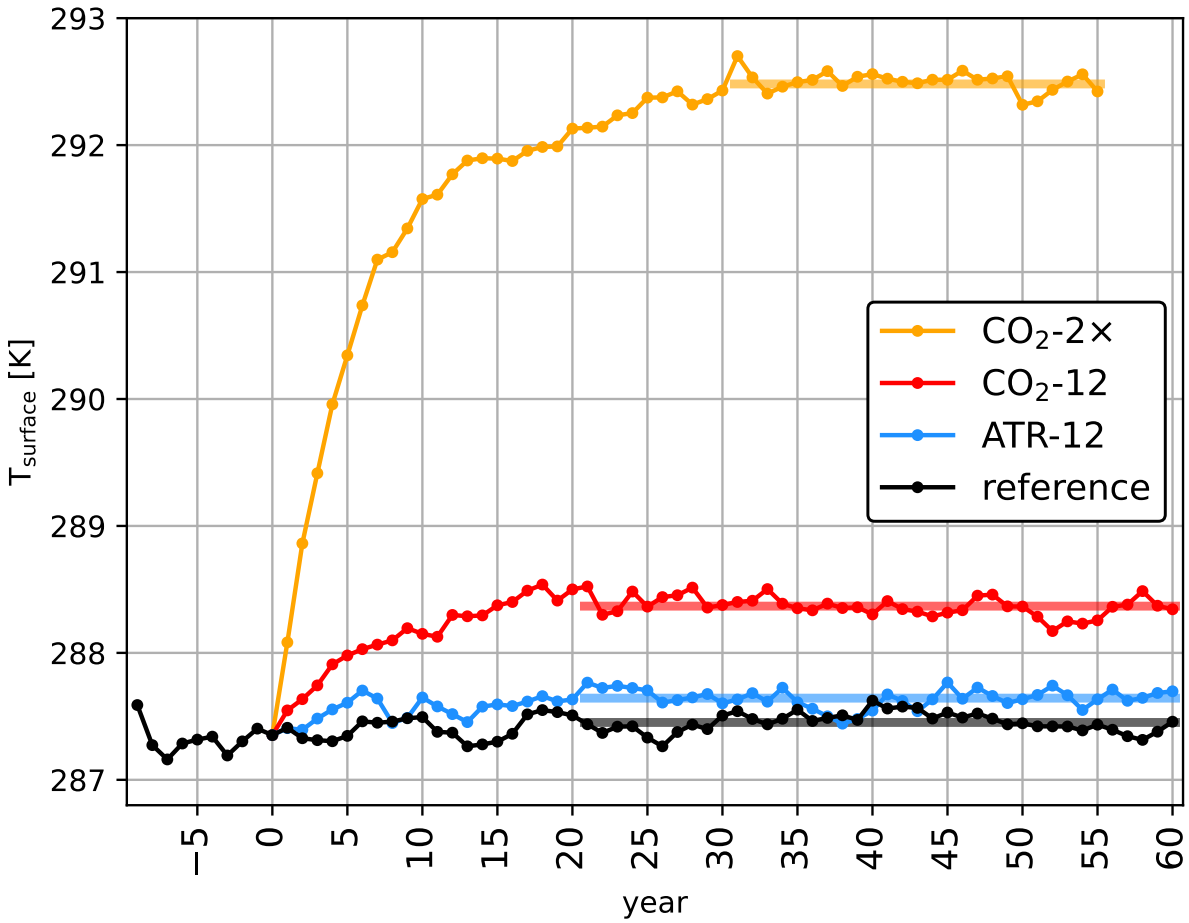

Figure 4.9: Evolution of surface temperature changes forced by contrail cirrus (blue curve) and by CO_2 increases (red and orange curve), based on the four EMAC-CCMod simulations with coupled mixed-layer ocean (MLO). The period before year zero was used as spin-up phase for the unperturbed reference simulation (black curve). In year zero, the respective perturbations were added. Shaded horizontal bars indicate the mean temperatures of the respective periods, which mark the time frames where the simulations have restored equilibrium.

sensitivity parameters and related slow feedbacks. Simulations were performed for ATR-12, CO_2-12, CO_2-2×, and a reference case without perturbation. Note that there is no ECHAM5-CCMod counterpart for these simulations.

Fig. 4.9 shows the evolution of surface temperature changes for all four simulations and depicts relatively well the three phases of a standard MLO simulation. First of all, the reference simulation (black solid line) was granted a 10 year spin-sup phase so that the model can relax to the initial MLO coupling. Subsequently, based on the reference simulation, the three perturbed simulations, ATR-12 (blue), CO_2-12 (red) and CO_2-2× (orange) were branched off by adding the respective perturbations. This transient phase ends when

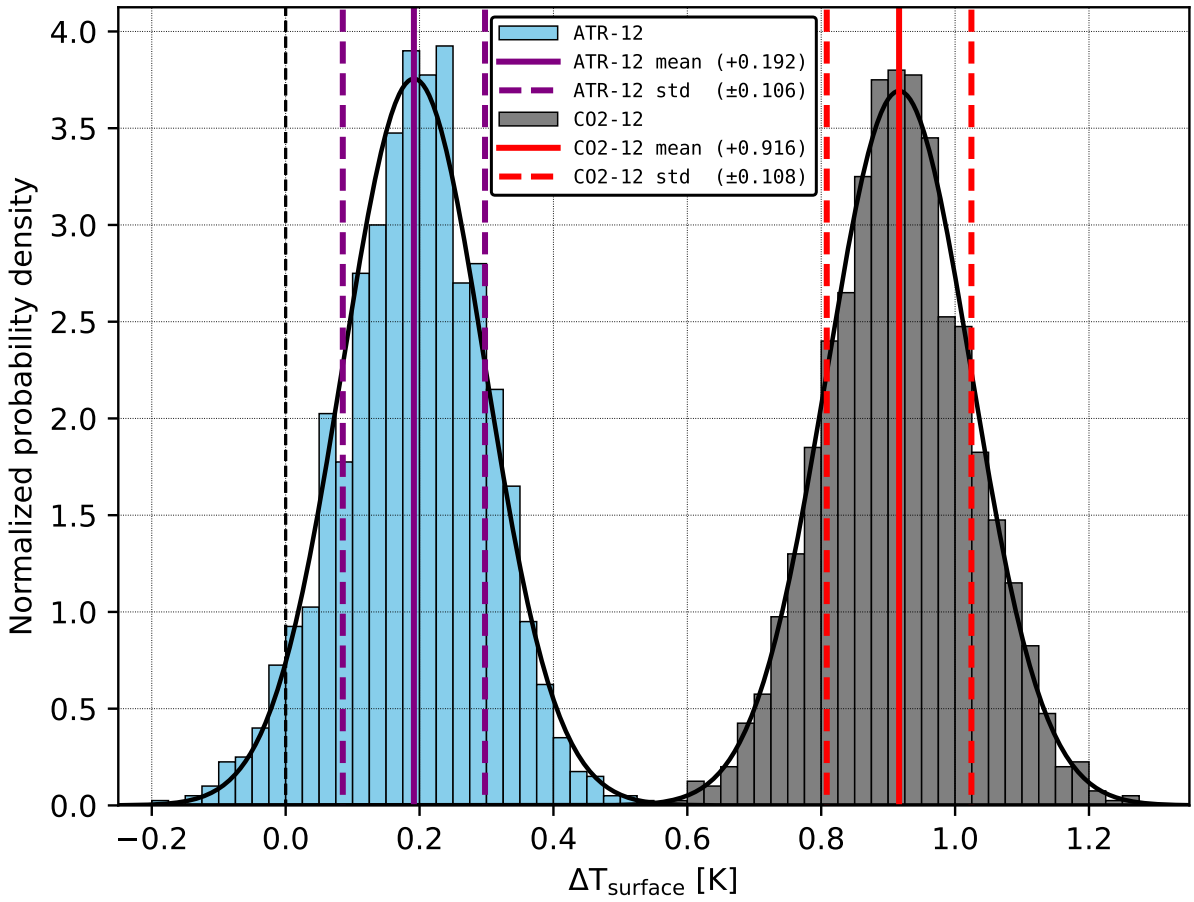

Figure 4.10: The plot shows the probability density distributions of surface temperature change based on the ATR-12 (blue) and CO_2-12 (gray) EMAC-MLO simulations. Both distributions are derived by combining all annual global mean surface temperatures of the EMAC-MLO reference simulation with those of the experiments mentioned before (bootstrap method). Data are normally distributed (black solid curve) in both cases. The respective mean values are depicted by vertical solid lines and the standard deviations by vertical dashed lines.

the model has reached a new equilibrium. Besides surface temperature change, time series of many variables (e. g. ice cover, cloud cover, specific water vapor and radiative imbalance) have been analyzed, to verify that the transient phase is completed. The equilibrium phase is masked by a low radiative imbalance in combination with largely stationary physical quantities on a climatological scale (see shaded horizontal bars in Fig. 4.9). For CO_2-2× the equilibrium phase starts 10 years later (year 31), compared to ATR-12 and CO_2-12, because the adjustment to the larger perturbation requires more time. Only the respective equilibrium phases were used for evaluation and analyzed by the PRP feedback analysis (see shaded horizontal bars in Fig. 4.9). The reference simulation was also continued for 60 more years, however only the last 40 years were used for evaluation to be compared with ATR-12 and CO_2-12. Due to the relatively large perturbation of CO_2-2× 25 years were enough to reach exceedingly significant results. The preceding spin-up phases were also used to apply the Gregory regression method (see Sect. 3.1.4 or Gregory et al., 2004), however, has been left aside here because for this method differences are only statistically significant for CO_2-2×.

For ATR-12 the global mean surface temperature increases by +0.192 K with a standard deviation of ±0.108 K (see Fig. 4.9 and Table 4.3). Overall, the warming is not restricted to regions where air traffic occurs. Almost the entire globe is characterized by increasing surface temperatures. Despite the equivalent RF_{adj} value (see Table 4.2), the corresponding counterpart CO_2-12 shows a more than four times larger surface temperature response of +0.916 K (see Table 4.3). That by far exceeds the expected reduction by a factor of about 2, as estimated from the ERF(ATR-12)/ERF(CO_2-12) factor. The surface temperature of the CO_2 doubling simulation increases by +5.013 K.

Following the general concept, the essential differences between the response to contrail cirrus or CO_2, respectively, are investigated by simulations with similar forcing strength. Hence, for statistical evaluation the temperature increase of ATR-12 and CO_2-12 have been further analyzed and compared. Fig. 4.10 shows the corresponding probability distributions of the surface temperature change, which are derived if a $\Delta T_{surface}$ value is calculated for all possible combinations of the annual mean surface temperature of the reference simulation and of ATR-12 (blue) or CO_2-12 (gray) respectively (bootstrap method). The surface temperature increase of both simulations is normally distributed. It is important to note, that both probability distributions are almost completely separated. The temperature increase of ATR-12 is significantly different from zero as well as from the CO_2-12 distribution.

4.2.4 Climate sensitivity and efficacy parameters

A central aspect of the radiative forcing concept is that radiative forcings can be used to predict surface temperature changes induced by physical drivers. The connection between radiative forcing and global mean surface temperature is established by the climate sensitivity parameter (see Eq. 2.11), which describes the capability of a radiative forcing to warm Earth's surface. However, radiative forcings of different forcers can only be fairly compared with respect to their impact on surface temperature, if their climate response

Table 4.3: Summary of surface temperature changes ($\Delta T_{surface}$), climate sensitivity parameters (λ) and efficacy parameters (r) derived from EMAC-CCMod FSST and MLO simulations. Efficacy parameters of ATR-12 utilize the CO_2-12 simulation as reference. Values in brackets show the statistical uncertainties expressed as standard deviations based on the interannual variability. The standard deviations for the climate sensitivity parameters were calculated after Díaz-Francés and Rubio (2013). No statistical uncertainties are provided for the efficacy parameters, as the underlying distribution (quotient of two ratio distributions) is not straightforward for calculating statistical parameters analytically. However, the respective probability distribution of the efficacy parameters based on ERF, which depicts the most uncertain one, is shown in Fig. 4.12.

	ATR-12	CO_2-12	CO_2-2×
$\Delta T_{surface}$ [K]	+0.192 (±0.106)	+0.916 (±0.108)	+5.050 (±0.096)
λ (RF_{inst}) [$KW^{-1}m^2$]	0.227 (±0.126)	1.659 (±0.196)	1.730 (±0.037)
r (RF_{inst})	0.137		
λ (RF_{adj}) [$KW^{-1}m^2$]	0.223 (±0.124)	1.073 (±0.127)	1.209 (±0.026)
r (RF_{adj})	0.208		
λ (ERF) [$KW^{-1}m^2$]	0.337 (±0.254)	0.887 (±0.257)	1.104 (±0.068)
r (ERF)	0.380		

is comparable, or in a more mathematical sense, if their corresponding climate sensitivity parameters are of approximately the same size. Thus, the ratio of both climate sensitivity parameters, which is the efficacy parameter (r), should be close to unity (see Eq. 2.12). For conceptual and historical reasons CO_2 increase experiments are normally used as reference for efficacy calculations (Ramaswamy et al., 2018).

Depending on the radiative forcing type, different climate sensitivity and efficacy parameters have been determined. Studies already revealed that efficacy parameters, based on the more traditional radiative forcings (RF_{inst} and RF_{adj}), deviate considerably strong from unity for some forcers (Hansen et al., 2005). In contrast, if based on the ERF an overall improvement can be observed (Richardson et al., 2019). However, efficacy parameters with large deviations from unity were also found in the ERF framework (Marvel et al., 2016, see Fig. S2 in their supplement).

So far, the respective behavior of contrail cirrus had been unknown as efficacy calculations were not available. In the following, the different radiative forcings and temperature changes, presented in the previous sections, were utilized to determine various climate sensitivity parameters of contrail cirrus and CO_2. By combining both, the respective efficacy parameters have been determined, in order to verify whether contrail cirrus radiative forcings alone can be used for a reasonable estimate of the expected equilibrium surface temperature change.

Table 4.3 shows the calculated climate sensitivity and efficacy parameters, based on RF_{inst}, RF_{adj} and ERF. The climate sensitivity parameters of both CO_2 increase simulations are comparable in size, however those derived from the CO_2-12 simulations tend to be smaller as could be expected from literature (see for example Hansen et al., 2005, their

Table 1). This deviation increases for RF_{adj} and ERF. For this reason, in order to ensure a fair comparison with contrail cirrus, it is essential for the CO_2 increase experiment to be similarly sized in terms of radiative forcing.

Note that the parameters based on the RF_{inst} framework are just provided for the sake of completeness as the corresponding efficacy parameter is not expected to reach unity from known conceptual reasons - which are actually confirmed in this case. In the ERF (RF_{adj}) framework an efficacy parameter of 0.380 (0.208) was calculated. Thus, the efficacy parameter of contrail cirrus is smaller than unity for both radiative forcings and fails to come close to unity even in the ERF framework.

As even the global mean surface temperature response is associated with considerable statistical uncertainty for ATR-12 and CO_2-12 (see Fig. 4.9), a careful evaluation of the significance of the climate sensitivity parameters is required. In Fig. 4.11, the climate sensitivity parameters of ATR-12 (blue) and CO_2-12 (gray), based on the ERF, are thus further statistically analyzed.

The sub-samples are derived by forming all possible ratios of annual mean ERFs and surface temperature changes (bootstrap method). Climate sensitivity parameters follow a ratio distribution (black solid lines), as the underlying quantities (ERF and $\Delta T_{surface}$) are normal distributed (Springer, 1979). Here, both distributions of the climate sensitivity parameter (for ATR-12 and CO_2-12) are positively skewed, meaning that the right tail of the distribution is longer and the mean (vertical solid line) is shifted to the right compared to the mode (maximum probability). Statistical uncertainties are expressed as standard deviations and were calculated after Díaz-Francés and Rubio (2013, see their Eq. 8). Confidence intervals, according to (Fieller, 1954), were also determined and fully confirm the correctness of the standard deviations, however, are not shown here. For ATR-12 the distribution includes negative values, as negative surface temperature responses may appear for the combination of individual years (see Fig. 4.9). Although both climate sensitivity parameter distributions are overlapping, a clearly significant separation is obvious with respect to their standard deviations (vertical dashed lines in Fig. 4.11). In addition, the climate sensitivity parameter of ATR-12 is significantly different from zero.

Division of both mean climate sensitivity parameters yields in a contrail cirrus efficacy parameter of 0.380. The respective distribution of efficacy parameters, again derived with the bootstrap method, is shown in Fig. 4.12 and follows a double ratio distribution (quotient of two ratio distributions). For this reason, the analytical methods used to evaluate the statistical uncertainties of the ratio distributions are no longer applicable. However, the general shape of the efficacy parameter distribution is almost identical to the climate sensitivity parameter distribution of ATR-12 (see Fig. 4.11) and thus similarly sized statistical uncertainties can be expected. Nevertheless, if the formula after Díaz-Francés and Rubio (2013) is applied (which assumes that the two input distributions are normally distributed, which is in fact not the case), a standard deviation of ± 0.307 is yielded for the efficacy parameter based on the ERF. For both reasons the efficacy parameter is, with high probability, smaller than unity as well as significantly larger than zero. About 90 % (68 %) of the calculated efficacy parameters, determined with the bootstrap method, are

smaller than 1 (0.5). Thus, the analysis convincingly indicates the reduced effectiveness of contrail cirrus in forcing surface temperature changes, compared to CO_2.

It has to be stated that the actual mean values derived from the ratio distributions do not exactly equal the ratio of the respective mean $\Delta T_{surface}$ and mean ERF due to the nature of the ratio distribution (Qiao et al., 2006). This feature becomes more prominent if the mean value of the denominator of the ratio distribution (in this case the radiative forcing) is close to zero. For consistency reasons all climate sensitivity and efficacy parameters presented within the present thesis were calculated from the mean $\Delta T_{surface}$ and mean

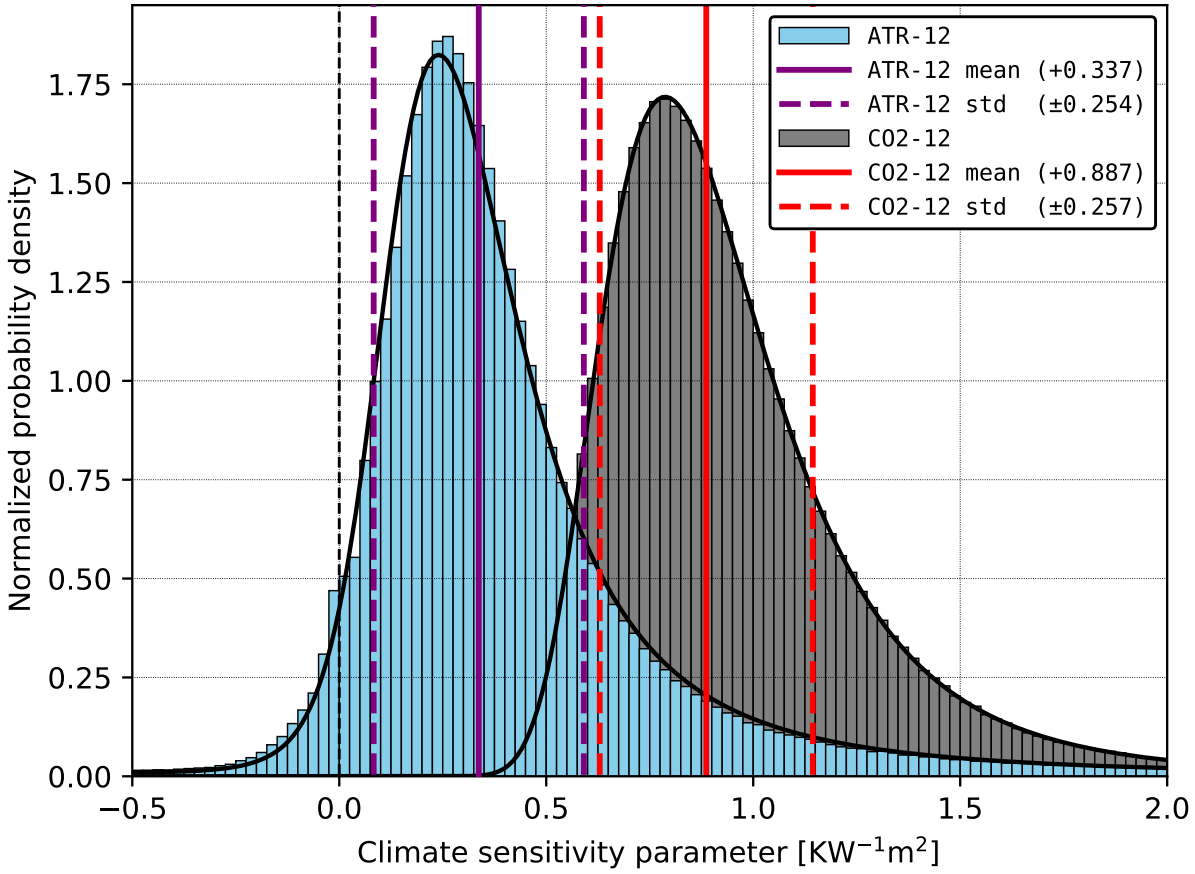

Figure 4.11: Shown are the distributions of the climate sensitivity parameter based on the ATR-12 (blue) and CO_2-12 (gray) simulations, derived with the bootstrap method. Here the ERF is used to calculate climate sensitivity parameters. ERFs (surface temperature changes) are taken from the EMAC-FSST (EMAC-MLO) runs. The climate sensitivity parameters follow ratio distributions (black solid curve) as the climate sensitivity parameter is calculated as the quotient of two normally distributed parameters (radiative forcing and temperature change). The respective mean values are depicted by vertical solid lines and the standard deviations by vertical dashed lines (calculated after Díaz-Francés and Rubio, 2013).

radiative forcings (not derived from the respective ratio distributions). The suitability of this way to calculate mean ratio values is later also independently confirmed by yielding consistency with the results of the feedback analysis (see the total feedback parameter in Fig. 4.18 which corresponds to the inverse of the climate sensitivity parameter).

4.2.5 Slow feedbacks

During the transient phase, slow feedbacks (SF) evolve as a reaction to changing surface temperature and compensate the radiative forcing until a new quasi-equilibrium is attained. In theory, balance is restored when the remaining radiative imbalance approaches zero. However, due to interannual variability the net radiative flux values continue to vary around zero even for climate equilibrium. The PRP feedback analysis was applied to the equilibrium phases of the simulations, where the temperature and climate response as

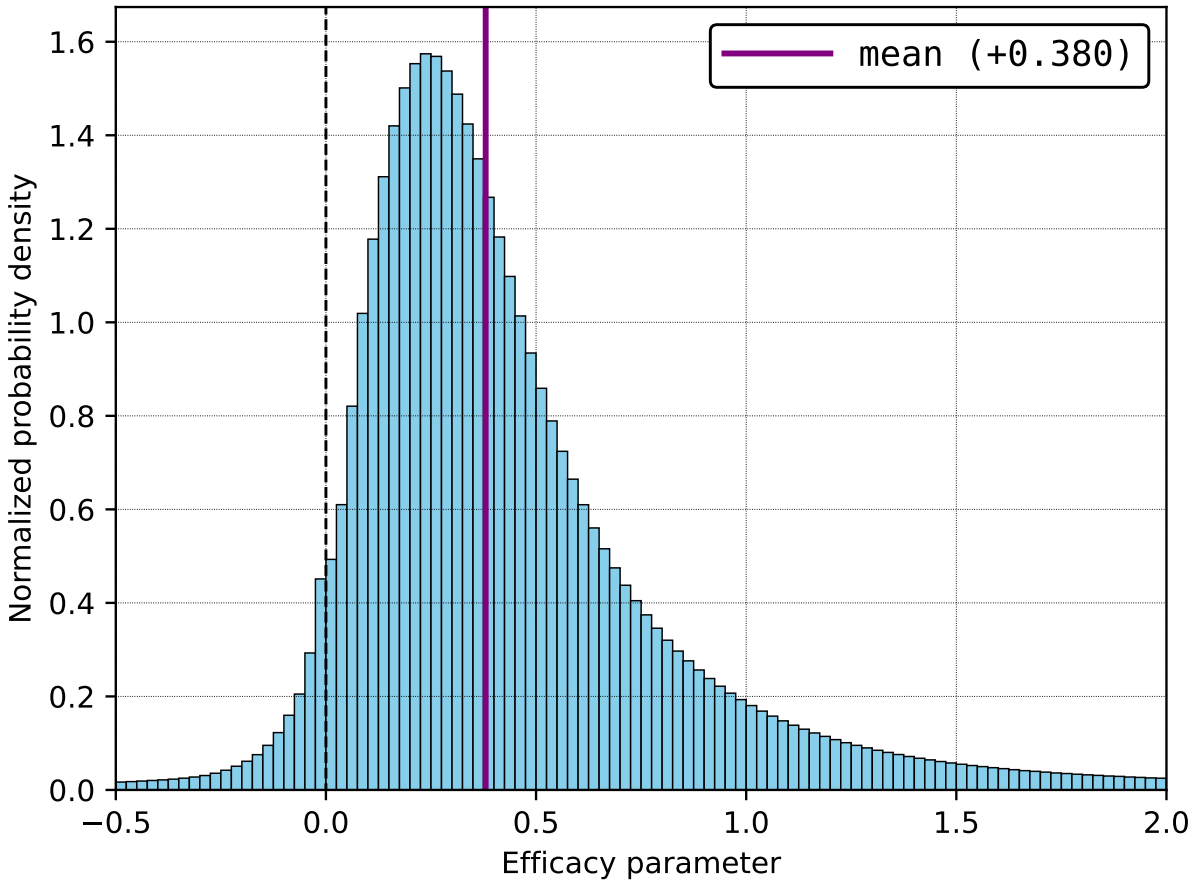

Figure 4.12: Distribution of contrail cirrus efficacy parameters. The samples are derived with the bootstrap method by dividing the climate sensitivity parameters of ATR-12 by those of CO_2-12 (see Fig. 4.11). Statistical uncertainties are deliberately omitted as the underlying distribution (quotient of two ratio distributions) is not straightforward.

well as the SFs have been fully developed. SFs were determined for ATR-12, CO_2-12 and CO_2-2×.

It is important to mention that the flux differences, determined from the MLO simulations, include both RAs and SFs (see Sect. 3.2.1 for further details). For this reason the RAs, shown in Sect. 4.2.2 had to be subtracted in order to yield the SFs. Furthermore, the SFs, as shown in this section, are yet expressed as radiative fluxes (Wm^{-2}). Feedback parameters ($Wm^{-2}K^{-1}$), which set SFs in relation to surface temperature change are shown later (see Sect. 4.2.6).

Fig. 4.13 shows the SFs calculated for ATR-12, displayed together with the ERF and the remaining mean radiative imbalance at equilibrium. If all SFs (left box) are added to the ERF (middle box), the radiative imbalance (right box) is yielded. As contrail cirrus, due to its interactive nature, may also be able to adjust to surface temperature changes and related follow up effects, a corresponding SF was added. The residuum explains the flux difference between radiative forcing calculations and feedback analysis, which could not be fully closed. Despite the necessity to subtract RAs, the extent of the statistical uncertainties stays within reasonable limits, allowing to interpret the SF mean values.

Similar to RAs, the total SF is largely determined by the natural cloud, water vapor, lapse rate and Planck components. The natural cloud SF is negative and contributes

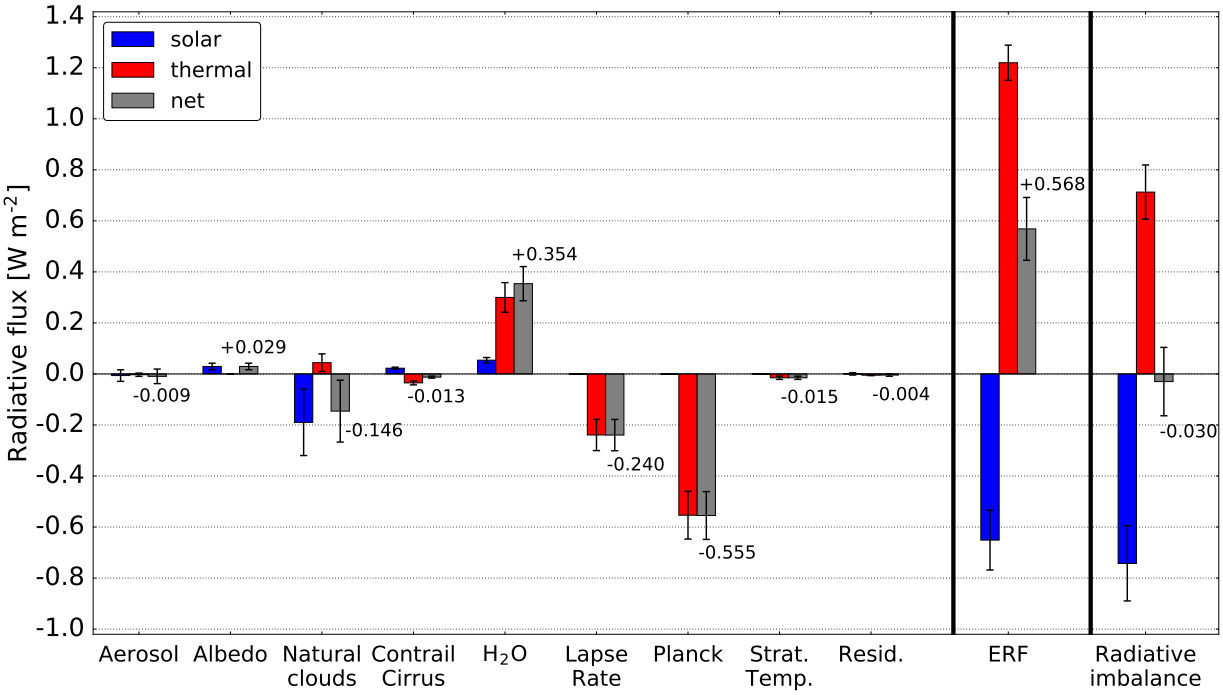

Figure 4.13: Slow feedbacks (SF) determined by feedback analysis of the ATR-12 EMAC-MLO simulation (left box). The respective radiative fluxes (gray bars) are subdivided into a shortwave part (blue bars) and a longwave part (red bars). Whiskers show the 95 % confidence intervals based on the interannual variabilities.

the largest portion to SW radiative flux reduction, which already indicates that changing low clouds gain in importance when analyzing contrail cirrus induced surface temperature changes. In contrast, the corresponding RA (Fig. 4.5) was larger in magnitude (-249 mWm^{-2}) and mainly driven by the LW part.

As usual for SF, the Planck contribution features the main part to counteract the ERF (Vial et al., 2013; Klocke et al., 2013; Rieger et al., 2017; Sherwood et al., 2020). The Planck SF is a direct consequence of rising surface temperatures (+0.192 K), which increases LW

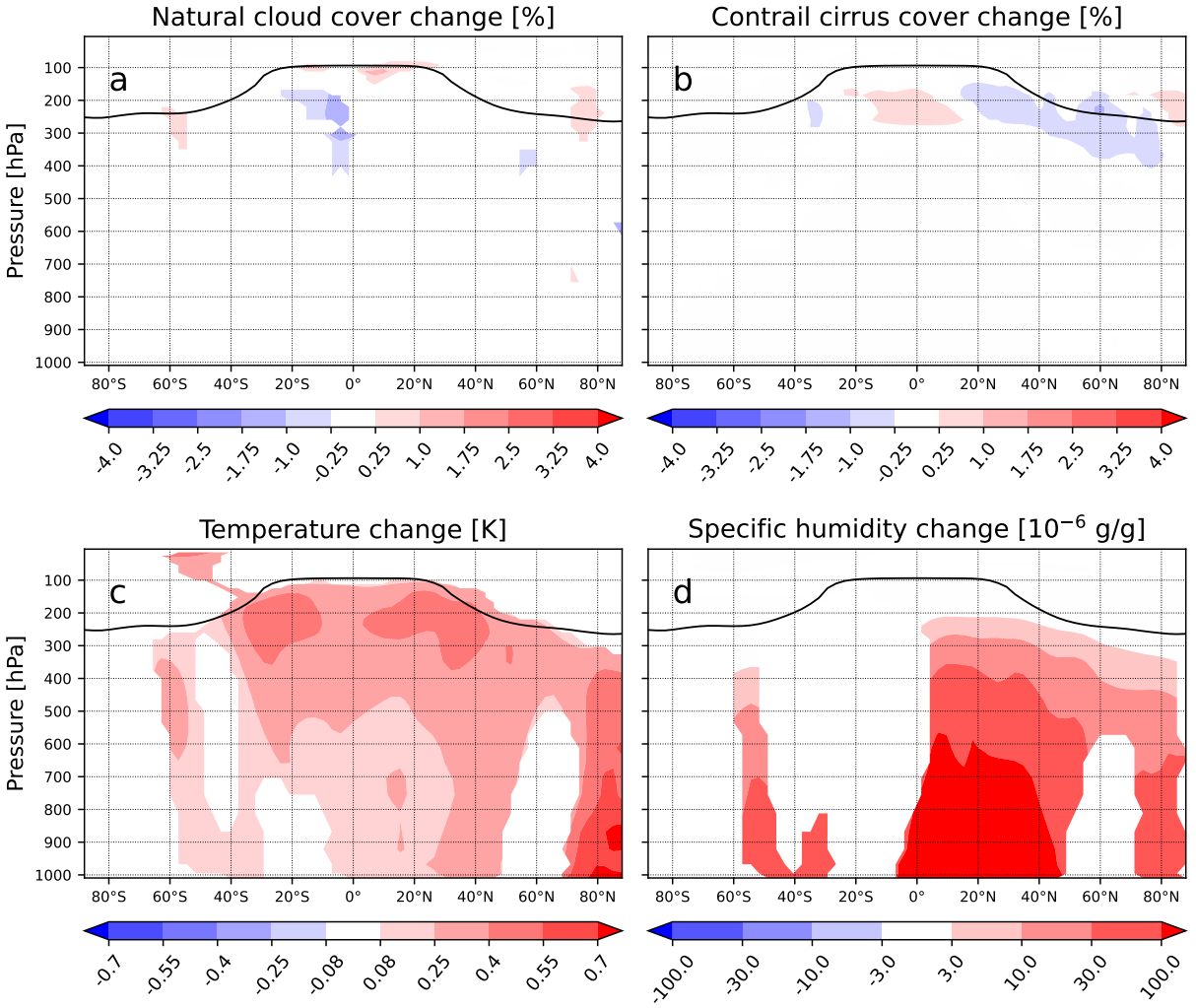

Figure 4.14: Zonal mean vertical cross section of natural cloud cover change (a), contrail cirrus cover change (b), temperature change (c) and specific humidity change (d) in response to a contrail cirrus induced surface temperature increase. To exclude the impact of RAs, data from the EMAC-FSST ATR-12 simulation was subtracted from the EMAC-MLO ATR-12 simulation. The black solid line shows the climatological tropopause height. Data is only plotted for areas where the deviation from the reference simulation is significant to the 99 % confidence interval with respect to interannual variability.

emission to space. As it can be assumed that the lower levels of the atmosphere are well mixed the surface temperature change is extended through the whole troposphere for calculating the Planck SF. The remaining deviations from that temperature profile are depicted by the lapse-rate SF.

Water vapor and Lapse rate SF are again different in sign, as common in global climate simulations. However, the water vapor SF is overcompensating the Lapse rate SF by about 50 %, leading to an overall positive contribution. The overcompensation is most likely the result of the larger part of tropospheric temperature increase already being included in the Planck SF (see below). For that reason a growth of water vapor can be attributed to the lapse rate as well as the to the Planck SF (in contrast to the FSST simulations where the Planck RA was close to zero and most water vapor changes were a consequence of the lapse rate RA).

With regard to the overall positive effect of the combined water vapor and lapse rate SF, the Planck SF dominates the LW and net radiative flux reduction that restores equilibrium. The contrail cirrus SF is just slightly negative with the typical dominating LW and an opposing smaller SW part, which indicates a decrease of contrail cirrus cover. Thus the feedback of contrails to themselves via surface temperature change is weak, which is consistent with previous evidence of only a moderate sensitivity of contrail radiative forcing to background climate change (Marquart et al., 2003; Chen and Gettelman, 2016; Bock and Burkhardt, 2019).

Similar to the RAs the origin of SFs can be traced back to adaptions of the underlying physical quantities. As explained above, the MLO simulations primarily yield a combination of RA and SF components. To remove the RAs component, the changes of physical quantities, calculated for the FSST simulations (see Sect. 4.2.2), were subtracted from the corresponding changes derived for the MLO simulations. Accordingly, Fig. 4.14 shows the so adjusted changes of some key variables for ATR-12, representing their slow reaction to surface temperature response.

Contrail cirrus cover slightly decreases between 20°N and 80°N (see Fig. 4.14 b). Decomposition of the radiative SF into upward and downward fluxes reveals that the origin of the negative contrail cirrus SF develops exactly at these latitudes and heights (not shown here). There is hardly any significant signal in the pattern of natural cloud cover change (see Fig. 4.14 a). The main contribution to negative SW natural cloud SF originates from increasing low and mid level clouds between 60°N and 80°N, but these structures lack sufficient local significance and thus are not visible in the figure. Hence, although the global net cloud feedback in ATR-12 is significantly negative, it is not possible to attribute its origin to a specific process. The temperature response distribution (see Fig. 4.14 c) retains some striking similarity with the corresponding FSST case. Nevertheless, the temperature increase is no longer constrained by FSST and thus spreads over the entire troposphere. Surprisingly, the largest contribution to the negative lapse rate SF originates between 30°S and 10°N, substantially further south than the maximum of air traffic density. This indicates that the vertical temperature response gradient developing in the FSST simulations is largely retained and penetration of warming downward towards the ground is limited. Specific humidity increases almost throughout the entire troposphere, but remains barely

significant in regions south of the equator. In contrast to the lapse rate SF, the largest contribution to the water vapor SF can be found between 0° and 40°N, in accordance with the largest increase of water vapor, which is more related to the full temperature response (lapse rate + Planck SF) rather than to the maximum lapse rate change.

The MLO simulation performed for CO_2-12 is now used to compare the results of ATR-12 to a standard CO_2 increase simulation with similar initial RF_{adj}. The simulation was supported by a CO_2 doubling simulation (CO_2-2×) in order to backup the statistics from CO_2-12 (this, however, has proven to be not necessary). The SFs of CO_2-12, calculated with the PRP feedback analysis, can be found in Fig. 4.15. Again, the sum of all SFs (left box) and the ERF (middle box) yields the radiative imbalance (right box). Despite, the RAs were subtracted, in order to derive the SFs, the residuum and statistical uncertainties are fairly small. In contrast to the ATR-12 case where some feedback of atmospheric warming to the contrail cirrus itself occurred, there is - as expected - no corresponding feedback on CO_2 in CO_2-12.

Overall, the dominating feedbacks again consist of the Planck, water vapor, natural cloud and lapse rate SF. Similar to the RA counterpart, the natural cloud SF is mainly influenced by the SW part. Thus, in combination with the water vapor and albedo SF, the increase in the SW part of the radiative imbalance can be explained. The water vapor SF

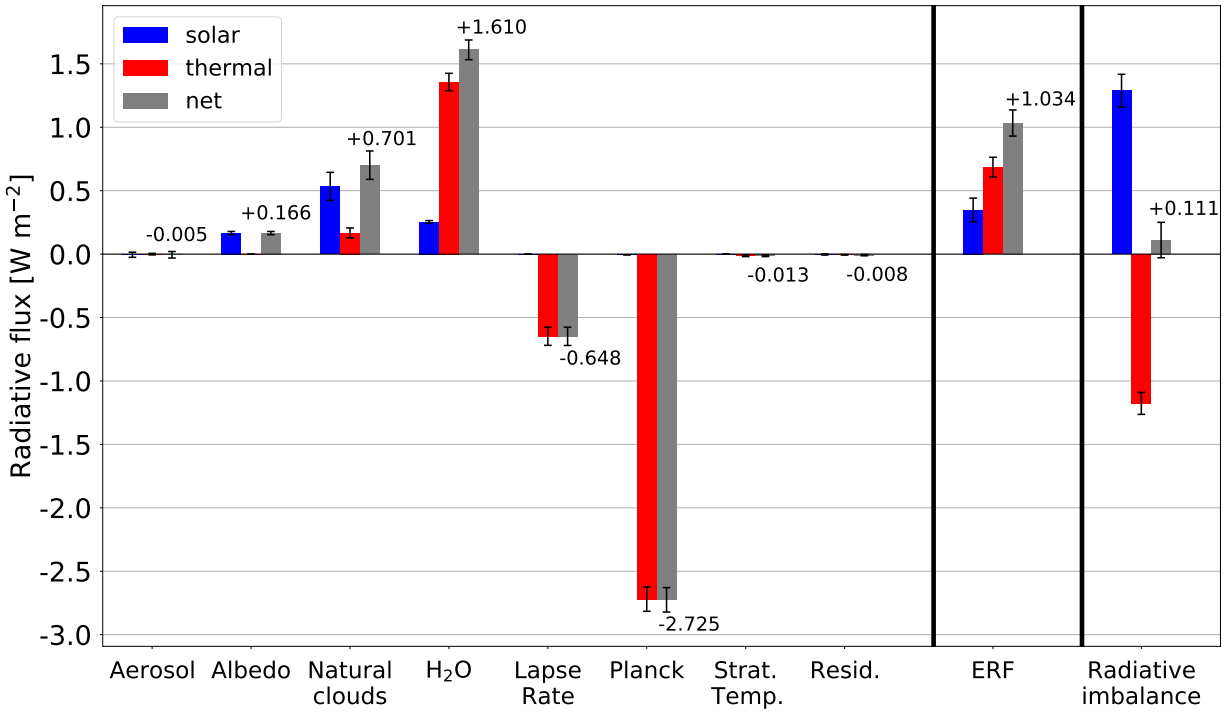

Figure 4.15: Slow feedbacks (SF) determined by feedback analysis of the CO_2-12 EMAC-MLO simulation (left box). The respective radiative fluxes (gray bars) are subdivided into a shortwave part (blue bars) and a longwave part (red bars). Whiskers show the 95 % confidence intervals based on the interannual variabilities.

exceeds the lapse rate SF by a factor of almost 3 in magnitude, which may be again the consequence of a fair amount of tropospheric temperature increase being included in the Planck SF. The overall positive contributions of the cloud and combined water vapor and lapse rate SFs are largely compensated by the Planck SF, which is the direct consequence of the surface temperature increase of +0.916 K for CO_2-12 (again, extended through the whole troposphere to calculate the Planck SF).

The natural cloud SF deserves special attention as it represents the major difference between ATR-12 and CO_2-12. For CO_2-12 it is almost 5 times larger and thus dominating the deviation from ATR-12. To determine the radiative origin of the strong positive natural cloud RA in case of CO_2-12 the respective upward and downward radiative fluxes were analyzed (see Fig. 4.17). The positive SW part of the natural cloud SF forms mainly between 0° and 50°S and between 20°N and 60°N at altitudes between 600 hPa and ground (see vertical gradients in the left panels of Fig. 4.17). Those regions are characterized by decreasing low and mid-level cloud cover (see Fig. 4.16 a). The positive contribution between 0° and 20°N is exclusively driven by adaptions of the LW radiative flux profile as a consequence of increasing cirrus clouds at about 300 hPa (see Fig. 4.17, strong vertical gradient in the bottom middle panel). Thus, while for the natural cloud RA it was a process in ATR-12 (compensation between contrail cirrus increase and natural cirrus decrease) that marked the difference to CO_2-12, for the natural cloud SF it is the low and mid-level cloud

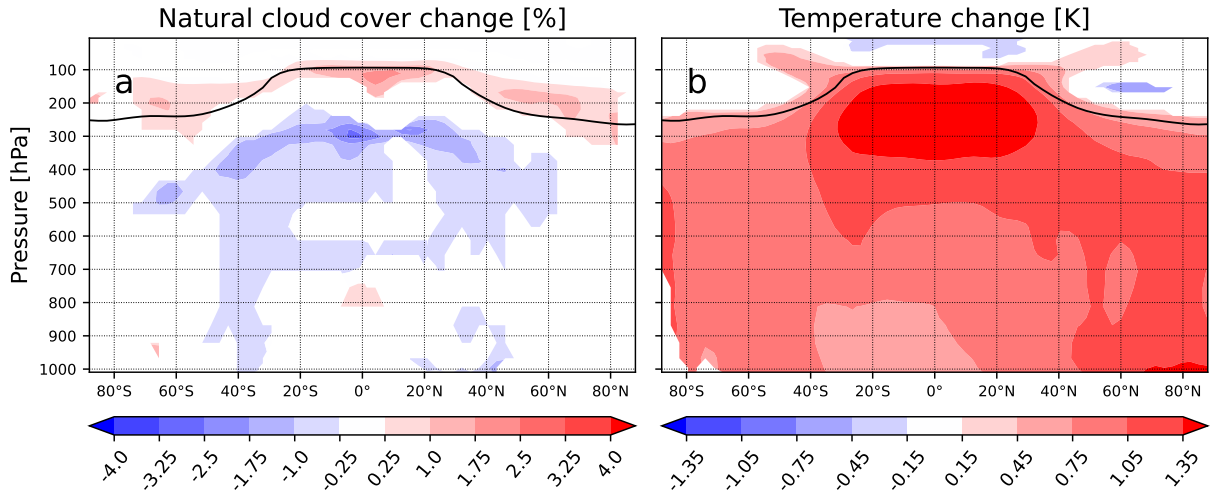

Figure 4.16: Zonal mean vertical cross section of natural cloud cover change (a) and temperature change (b) in response to a surface temperature increase induced by a CO_2 perturbation. To exclude the impact of RAs data from the EMAC-FSST CO_2-12 simulation was subtracted from the EMAC-MLO CO_2-12 simulation. The black solid line shows the climatological tropopause height. Data is only plotted for areas where the deviation from the reference simulation is significant to the 99 % confidence interval with respect to interannual variability.

decrease in CO_2-12 (which is largely absent in ATR-12) that explains the positive natural cloud SF in case of CO_2.

Strongest warming rates, which can be attributed to changes in the vertical temperature profile, are found between 30°S and 30°N in the upper troposphere, largely consistent with the distribution of the lapse-rate SF. The counteracting water vapor SF shows a similar behavior, with largest contributions around the equator. The negative albedo SF forms almost exclusively below 55°S and above 40°N, mainly due to a reduction of sea ice cover, but also land ice sheets. In contrast to ATR-12 the SFs and underlying changes of the basic variables are statistically considerably more significant for CO_2-12.

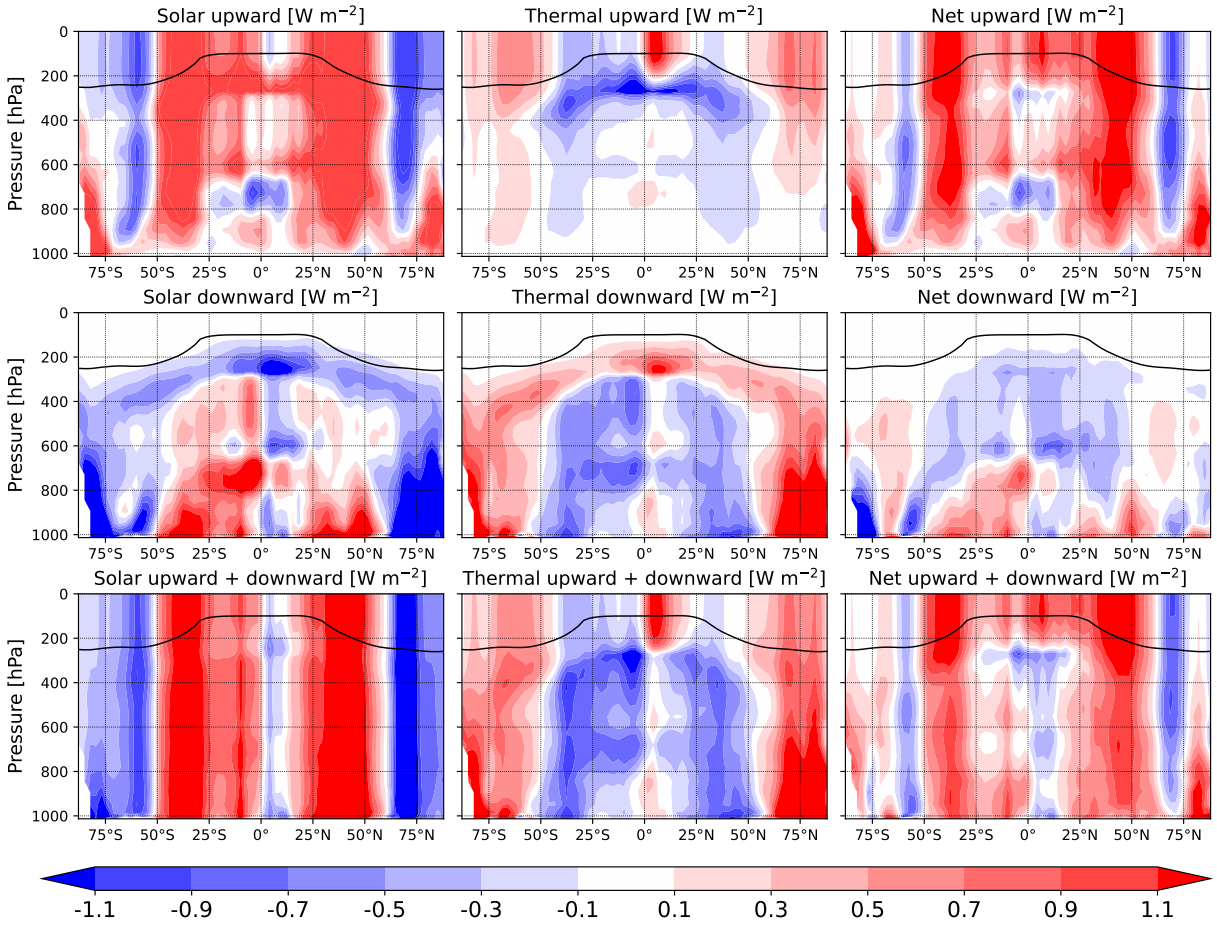

Figure 4.17: Zonal section of the natural cloud SF for CO_2-12 subdivided into upward (first row), downward (second row) and combined upward and downward vertical fluxes (third row). The respective fluxes are further decomposed into solar (left column), thermal (middle column) and net fluxes (right column). If averaging the uppermost level, at TOA, of the net, combined upward and downward fluxes (bottom right), the natural cloud SF of $+701\,\mathrm{mWm^{-2}}$ is yielded. The origin of natural cloud SF formation can be identified with the help of vertical gradients.

4.2.6 Feedback parameters

The origins of the reduced climate response of contrail cirrus could be pointed out in Sect. 4.2.5 on the basis of SFs. However, a direct comparison between the contrail cirrus and CO_2 related feedbacks is difficult as both simulations are based on different ERFs and, particularly, on surface temperature changes of different magnitude. To overcome this problem, the SFs were normalized by the corresponding global mean surface temperature change to yield the feedback parameters (FP, see Sect. 2.7). Fig. 4.18 shows the FPs calculated for contrail cirrus (blue) and CO_2 (gray). FPs describe the radiative flux change that is forced per unit surface temperature change. The sum of all FPs (left box) yields the total feedback parameter (α, right box) which equals the negative inverse of the climate sensitivity (see Sect. 2.8). Thus, the origin of deviating climate sensitivity parameters and therefore the reduced efficacy parameter of contrail cirrus, can be directly related to differing specific feedbacks when considering FPs.

As the FP calculation depends on surface temperature change and on the results of the FSST and MLO feedback analysis, their statistical uncertainties noticeably increase with respect to corresponding SFs (compare Fig. 4.18 with Fig. 4.13 and Fig. 4.15). However, the important natural cloud FP and the sum of all FPs remain significantly different between

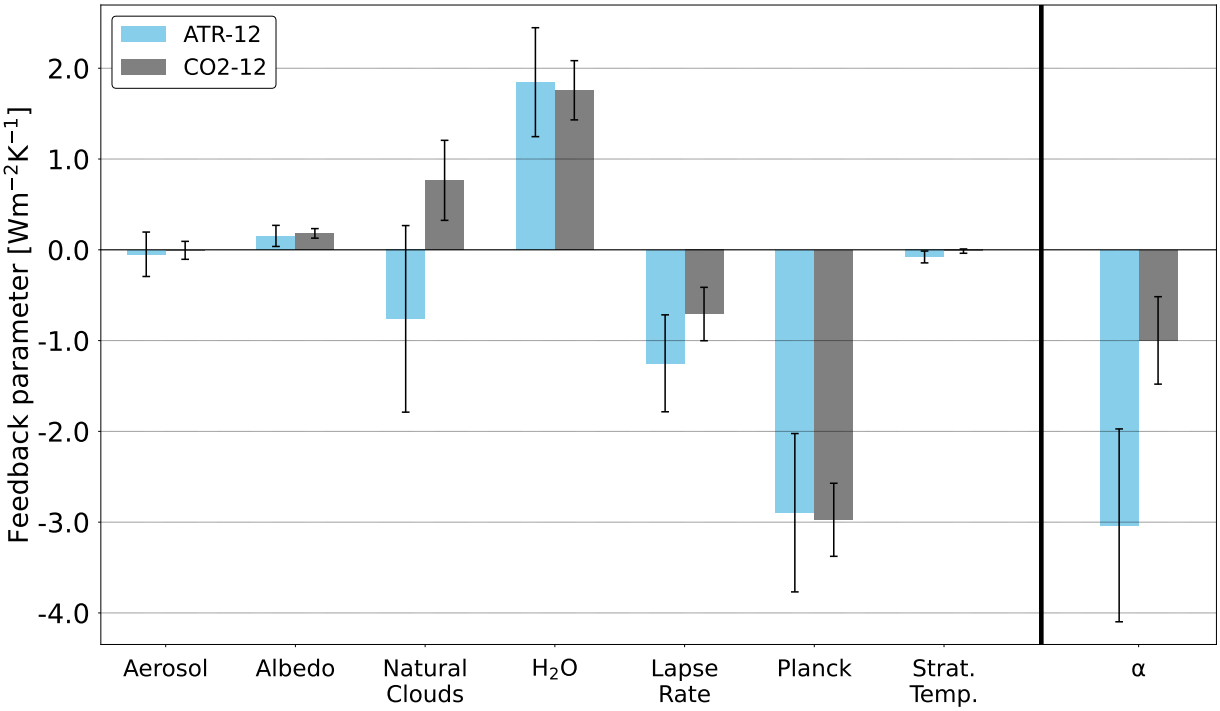

Figure 4.18: Comparison of feedback parameters (FP) derived for contrail cirrus (blue) and for a CO_2 perturbation (gray). The results are based on the ATR-12 and CO_2-12 EMAC MLO simulations. Whiskers show the standard deviations based on the interannual variabilities.

the contrail cirrus and CO_2 case. The capability to induce a surface temperature change is almost identical in ATR-12 and CO_2-12 for the albedo, water vapor and Planck FPs, while aerosol and stratospheric temperature FPs do hardly contribute anyway. The largest difference between contrail cirrus and CO_2, even in sign, can be found for the natural cloud FP. As described above, the deviations are related to low and mid level clouds, which are increasing in case of contrail cirrus and decreasing for CO_2.The remaining one quarter to explain the reduced climate sensitivity parameter of contrail cirrus is contributed by the lapse rate FP. The deviation originates mainly from a different behavior of warming Earth's troposphere. Relative to the respective surface temperature rise, the temperature increase with height is stronger for contrail cirrus than for CO_2. That might be connected with an attenuated vertical mixing of upper tropospheric air to ground levels (Schumann and Mayer, 2017). The zonal distributions of the lapse rate FPs are very similar for contrail cirrus and CO_2, with largest negative contributions around the equator and positive values near the poles (in good agreement with Chung and Soden (2015) and Rieger et al. (2017), see their Fig. 2).

Chapter 5

Discussion

This chapter aims to discuss the results of the present thesis and to set them in relation to state-of-the-art knowledge. First the consequences of air traffic scaling on contrail cirrus climate impact are discussed, as the validity of the results described in Ch. 4 for the case of unscaled air traffic is important for the conclusion of the present thesis. Second, ECHAM5-CCMod and EMAC-CCMod results are compared against each other and against literature. The chapter closes with a discussion on the consequences of the substantially reduced climate impact of contrail cirrus and its importance for future mitigation scenarios.

5.1 Consequences of scaling

Scaling of air traffic is essential to reach sufficient statistical significance levels for contrail cirrus impacts beyond conventional radiative forcing. Scaling experiments (see Sect. 4.1.1) revealed that a 12× increase of the underlying AEDT 2050 air traffic dataset is sufficient for ECHAM5-CCMod simulations. A lower scaling would have been possible for the EMAC-CCMod simulations, however, it was not changed for consistency reasons. Contrail cirrus occurrence largely follows the pattern of air traffic density, which is widely non-uniformly distributed. Even if the global mean climate impact of contrail cirrus is relatively low (e. g. compared to standard CO_2 doubling simulations), saturation effects can be reached locally (e. g. Bock and Burkhardt, 2019). In combination with scaling, the saturation effect gains in relevance, because stronger relative growth rates of contrail cirrus coverage and radiative forcing in regions with low air traffic density are yielded. Thus the scaled results may to some extent be distorted compared to the original unscaled case. Analogously, adaptions of natural cloud cover and related radiative feedbacks may also be affected by scaling to some extent, e. g., because of non-linearities becoming apparent with growing radiative forcing. This section aims to address these consequences of air traffic scaling and their relevance for interpreting results of the present thesis.

5.1.1 Contrail cirrus properties

Fig. 5.1 shows the relative contrail cirrus cover increase as a result of the 12 times scaled air traffic. The distribution is derived by dividing the maximum-random-overlapped contrail cirrus cover*, simulated in ATR-12, by the corresponding cover of ATR-1. Low values indicate that the contrail cirrus cover increase is weaker than what the underlying scaling suggests, while larger values depict a more linear scaling response. Overall, the ratio is considerably correlated with air traffic density (see Fig. 3.1). For example, regions with low air traffic density (e. g. in the tropics), where hardly any contrail cirrus cover exists in the unscaled case, show a relatively linear response to air traffic scaling. In contrast, over central Europe and the eastern part of the USA the 12 times scaled air traffic leads to a contrail cirrus cover increase by a factor of only 1.4. One simple reason for this saturation effect is that the total cloud cover extent (natural clouds and contrail cirrus) is limited to a maximum of 100 %. After reaching this threshold, natural cirrus clouds and contrail cirrus can only change their radiative effect via IWC, ICNC and ice particle radius.

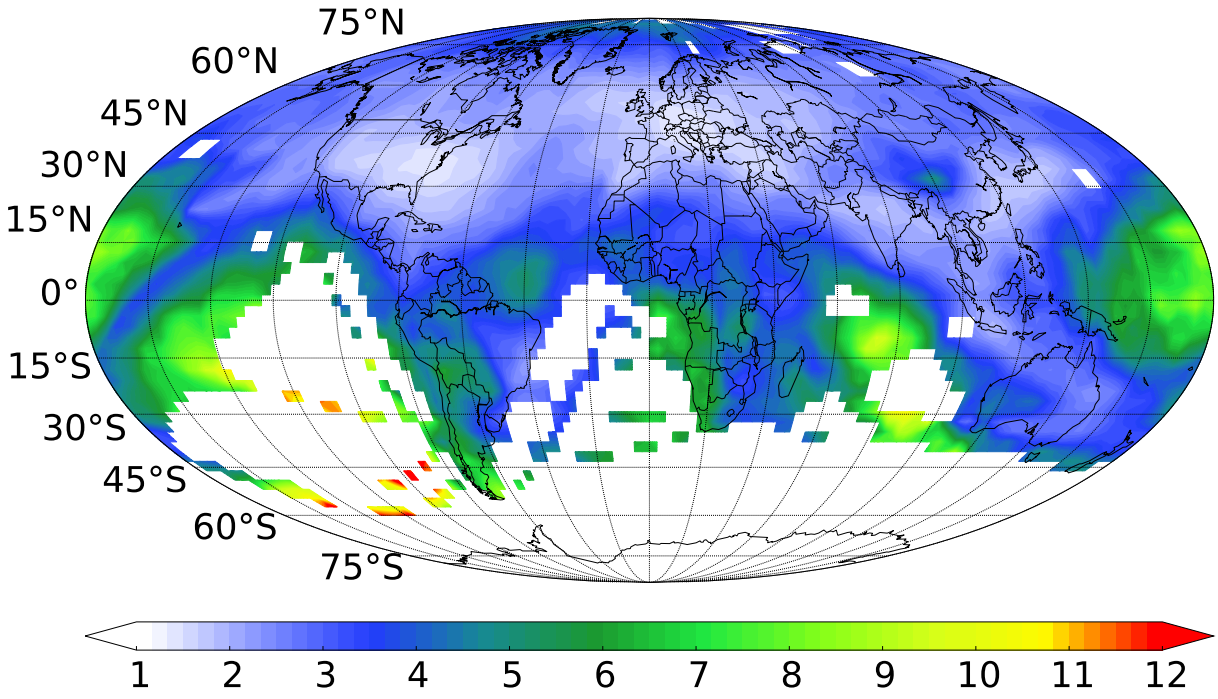

Figure 5.1: Global distribution of the relative growth factor of the maximum-random-overlapped contrail cirrus cover* due to a 12 times upscaling of air traffic in ECHAM5. For this purpose the overlapped contrail cirrus cover of ATR-12 was divided by the corresponding cover of ATR-1. Larger values indicate a more linear scaling response, while smaller values depict regions with saturation, where contrail cirrus cover increase is weaker than what the underlying scaling suggests. (Source: Bickel et al., 2020)

*maximum overlap for adjacent layers and random overlap for separated layers

Additionally, natural cloud and contrail cirrus formation is limited by the available amount of ambient water vapor in the upper troposphere and lower stratosphere, for which both compete. If completely consumed, formation of new clouds is restricted, even if air traffic scaling is further increased. Those saturation effects can be investigated by analyzing the growth factor of contrail cirrus IWC along with air traffic scaling (analogously to Fig. 5.1, not shown). While the growth rates of in-box* IWC largely follow the patterns seen in Fig. 5.1, the corresponding in-cloud distribution is far more uniform, without any maxima in the equatorial regions and hardly any factors larger than 3. Accordingly, the global mean in-cloud growth factor of contrail cirrus IWC at 240 hPa (1.5) is less than the corresponding one of overlapped contrail cirrus cover (2.7). The main reason for this behavior is that the large in-box IWC growth factors in the tropical regions are mainly driven by an extension of contrail cirrus cover. Thus scaling distorts the in-cloud contrail cirrus IWC far less than the contrail cirrus cover scaling response in Fig. 5.1 might suggest.

In addition, ambient water vapor is very limited at flight levels, which increases the deviations between scaled and unscaled simulations. Contrail cirrus in-cloud ICNC and optical depth follow these patterns closely. In summary, the contrail cirrus reaction to scaling can be subdivided into two major geographic regimes. Regions with large air traffic density (e. g. main flight corridors between 30°N and 60°N) where scaling predominantly induces contrail cirrus to grow through its microphysical properties (IWC, ICNC and ice particle radius) as contrail cirrus cover is already near its maximum. And regions with low air traffic density (mostly south of 15°N), where scaling causes contrail cirrus to grow by increasing both its coverage and microphysical properties.

Fig. 5.2 shows the corresponding zonal profiles of the maximum-random-overlapped contrail cirrus cover (a) and RF_{adj} (b) for different scalings of air traffic. Data depicted as solid lines are derived from the ECHAM5-CCMod simulations (Fig. 4.1). For larger scalings, a second maximum forms at around 20°N for both quantities. While the largest contributions to global contrail cirrus cover remain between 55 and 60°N, the maximum of RF_{adj} moves continuously to the south for larger scalings, to about 20°N for ATR-12. Compared to the contrail cirrus quantities shown above, the growth rate of RF_{adj} shows a response considerably closer to linearity of 4.2 (compared to 2.7 for contrail cirrus cover) to the 12 times scaling of air traffic. The larger growth rates in the tropics are the main reason for this feature. The zonal deviations between the maximum of cloud cover and RF_{adj} can be partly explained by the latitudinal dependence of incoming solar radiation, which cause a stronger specific shortwave radiative effect at low latitudes. Towards the equator the incoming solar radiation is markedly larger compared to mid latitudes, thus contrail cirrus gets an increasing specific impact (compare also to Fig. 4.3 b).

The zonal profile of the maximum-random-overlapped contrail cirrus cover derived from the EMAC-CCMod ATR-12 simulation (green dashed line) deviates markedly from its ECHAM5-CCMod counterpart. While the shape between 40 and 60°N is fairly well reproduced, contrail cirrus cover is overall lower in the tropics and subtropics. Additionally,

*Variables in a climate model can be averaged over the entire grid-box (in-box) or over the cloudy part of the grid-box (in-cloud), which represent the actual state within the cloud

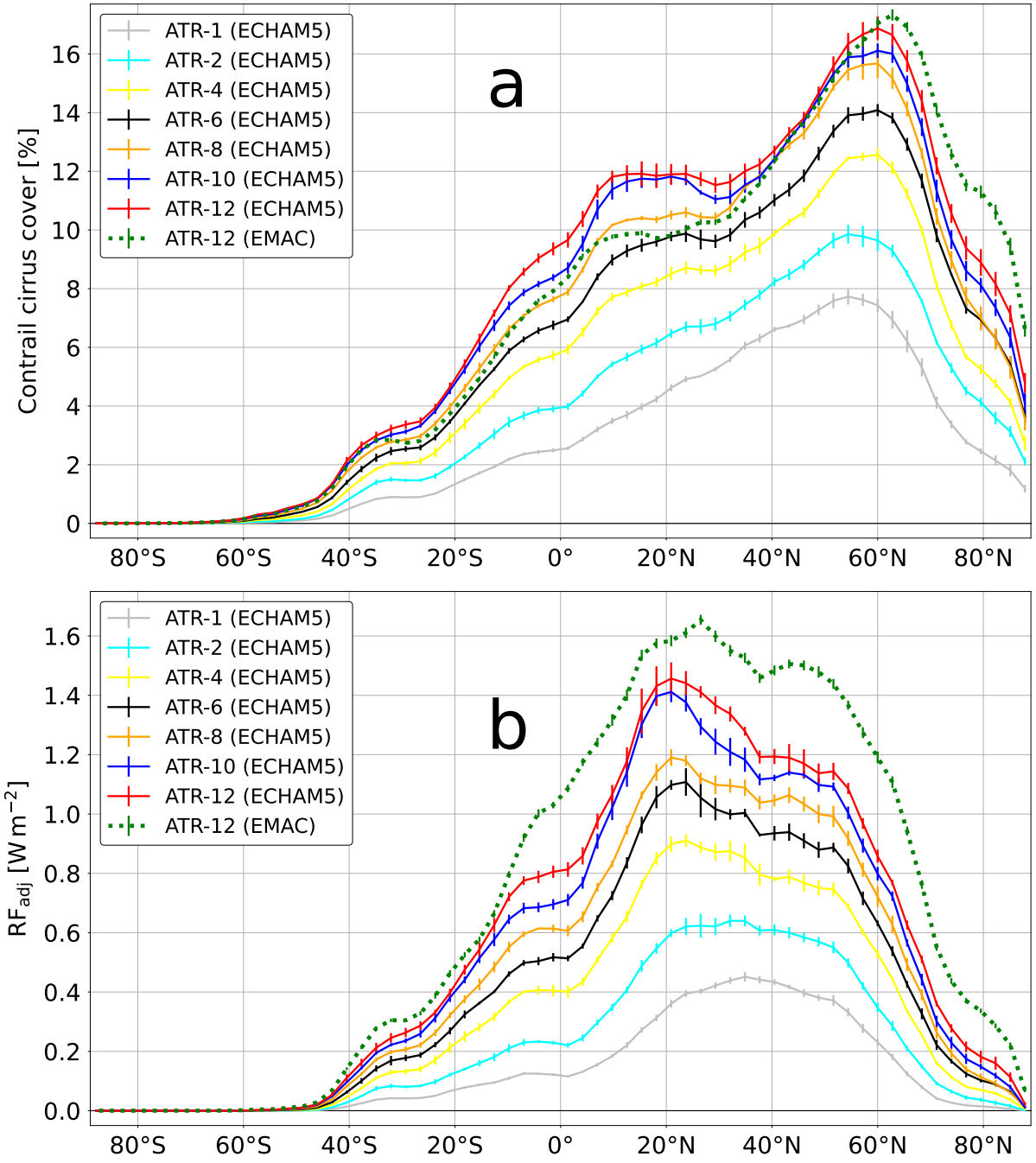

Figure 5.2: Zonal profiles of maximum-random-overlapped contrail cirrus cover (a) and RF_{adj} (b) for different scalings of the 2050 AEDT air traffic dataset. Solid curves are based on the ECHAM5-CCMod simulation while the green dashed line is derived from the EMAC-CCMod ATR-12 simulation. Statistical uncertainties (vertical lines) are depicted as the 95 % confidence intervals based on the interannual variabilities. (Source: Bickel et al., 2020)

there is almost no second maximum in the tropics, as to be noticed for ATR-10 and ATR-12 simulated with the ECHAM5-CCMod model. As pointed out in Sect. 4.2.1 the RF_{adj} based on the ATR-12 simulation of EMAC-CCMod (0.858 Wm^{-2}) is larger than for the corresponding ECHAM5-CCMod simulation (0.701 Wm^{-2}), but the excess of the tropical over the extratropical contribution is weaker in EMAC-CCMod than in ECHAM5-CCMod. Additional contributions originate across all latitudes, but mainly between 10°S and 70°N. The maximum at around 27°N for EMAC-CCMod is shifted to the north in comparison to ATR-10 and ATR-12 derived with ECHAM5-CCMod. For a more detailed discussion of the differences between ECHAM5-CCMod and EMAC-CCMod, see Sect. 5.2.

5.1.2 Rapid radiative adjustments

One major result of the present thesis is the reduced efficacy parameter of contrail cirrus (see Sect. 4.2.4). Efficacy parameters comprise the ERF/RF ratio (if the efficacy is analyzed in relation to conventional RFs) as well as the actual efficacy of ERF to warm earth's surface. For contrail cirrus both components work towards a smaller climate sensitivity of contrail cirrus and originate mainly from a decreasing natural cloud RA and SF. While the natural cloud RA is mainly affected by a compensation of natural cirrus clouds, the natural cloud SF is determined by a missing decrease of low and mid-level clouds (compared to the CO_2 reference case, as shown in Sect. 4.2.2 and 4.2.5). One important question is, whether and to which extent the scaling of air traffic affects the compensation effects of natural clouds and thus the reduction of efficacy.

The behavior is analyzed in detail on basis of the ECHAM5-CCMod scaling experiments for the natural cloud RA. For ATR-12 a natural cirrus cover decrease of -1.4 % evolves from a contrail cirrus cover of 3.1 % at 240 hPa, resulting in a relative compensation of 46.5 %. In the unscaled case (ATR-1) a slightly larger compensation of 46.9 % is found. A corresponding visualization of the evolution of natural cloud cover and contrail cirrus cover with scaling can be found in Fig. 2 of Ponater et al. (2021) and largely confirms these findings. Burkhardt and Kärcher (2011) calculated a lower natural cirrus compensation of 20 % in their simulations without air traffic scaling, however, only locally over Europe and the US and with a high level of statistical uncertainty.

The corresponding altitude dependence of the compensation of contrail cirrus cover increase, mentioned above, is shown in Fig. 5.3. While the compensation effect is roughly comparably sized at and above 240 hPa, deviations markedly increase below. E. g., at 300 hPa a contrail cirrus cover compensation of 27.7 % for ATR-1 faces a compensation of 60.4 % for ATR-12. This suggests a tendency for an increasing negative natural cloud RA for larger scalings of air traffic at lower altitudes and thus a stronger ERF reduction. However, this region is already located below the maximum of natural cloud cover reduction (see Fig. 4.3 a) and thus only has a secondary influence on the natural cloud RA. Furthermore, those deviations in cloud compensation between ATR-1 and ATR-12 are located considerably lower than the maximum occurrence of contrail cirrus cover (see middle panel of Fig. 5.3). Above 240 hPa the effect is even reversed so that the compensation of contrail cirrus cover becomes stronger for smaller scalings. Therefore, it can be concluded, that

air traffic scaling may to some extent strengthen the negative natural cloud RA, but the scaling effect is far from dominating the magnitude of the ERF reduction of -63 %.

Compensation effects on the basis of parameters that are equally relevant for radiation, e. g., IWC or optical depth, were also analyzed. For ATR-1 about 73 % of global mean contrail cirrus IWC is compensated by a decrease of global mean natural cirrus IWC at 240 hPa. For ATR-12 a slightly larger compensation of 76 % was calculated. The vertical distribution shows a similar behavior as for the contrail cirrus cover compensation, described above, with larger deviations towards lower altitudes.

5.1.3 Slow feedbacks

The potential sensitivity of simulated surface temperature change to air traffic scaling cannot be further analyzed as only one respective MLO simulation was performed. Surely, surface temperature change will be affected by saturation effects as well, due to its close

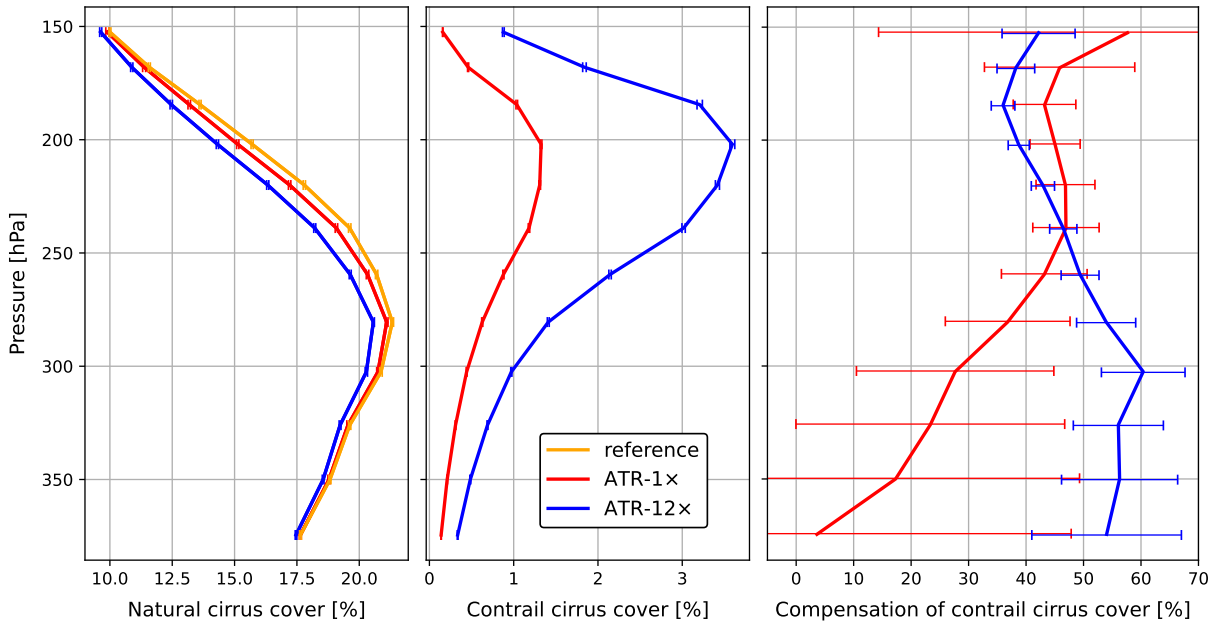

Figure 5.3: Contrail cirrus cover partly forms at the expense of natural cirrus cover. The right plot shows the relative amount of contrail cirrus cover, which is compensated by a decrease of natural cirrus cover (natural cirrus cover decrease divided by contrail cirrus cover). For example, a compensation rate of 100 % would result in a zero net cloud cover increase. The middle plot shows the contrail cirrus cover and should primarily serve for highlighting those levels where compensation effects potentially have the largest absolute impact. All three simulations were performed with the ECHAM5-CCMod model in combination with the AEDT 2050 air traffic dataset. Note that the simulations are based on the relatively short FSST simulations, however, were extended to 23 years in order to yield significant results for the compensation of contrail cirrus cover. Whiskers show the 95 % confidence intervals based on the interannual variabilities.

relation to radiative forcing. In this sense, regarding the climate sensitivity and efficacy parameters some qualitative conclusions may be drawn.

For example, no compensation effects (contrail cirrus cover grows at the expense of natural cirrus cover, as obvious for RA) can be observed for SFs as the respective cloud covers at those levels hardly change (see Fig. 4.14 a, b). The natural cloud SF is almost completely determined by a change of mid and low level clouds. Thus, the compensation effect is mainly a phenomenon covered by RAs and therefore already included in the ERF.

Nevertheless, the magnitude of the SFs and FPs is dependent on the ERF and thus is indirectly affected by compensation effects induced by air traffic scaling. However, for the climate sensitivity parameter, which is defined as the ratio of the surface temperature change to the radiative forcing, the effect of scaling largely vanishes, because both quantities will be affected in the same direction. For this reason efficacy calculations are probably less affected by the consequences of air traffic scaling than the previous sections might suggest.

5.1.4 General conclusions on the consequences of scaling

In summary, scaling affects the development of contrail cirrus and the response of the model in various ways. The upper boundary for cloud cover and the limited availability of ambient water for cloud formation result in distinct saturation effects. Besides the damped growth of contrail cirrus with increasing scaling, the region of largest radiative impact, in terms of RF_{adj}, is shifted to the south. In addition, evidence was found, that the compensation of natural cirrus clouds, which counteracts contrail cirrus formation, is affected by scaling. Especially for lower flight levels (below 240 hPa) air traffic scaling increases the reduction of natural cirrus and therefore results in a strengthened negative natural cloud RA. However, as discussed above, the resulting ERF reduction is by far larger than what can be explained by the influence of the increased compensation effect that is induced by air traffic scaling. Thus, even if the ERF reduction were overestimated to some extent it remains severe compared to other recently reported outliers (Richardson et al., 2019, see their Fig. 1). Less influence is expected for the climate sensitivity and efficacy parameters, which are calculated from the ratio of the surface temperature change to the radiative forcing, as scaling affects both quantities in the same direction.

Based on these findings, there is strong evidence that the efficacy of contrail cirrus, to warm Earth's surface, is substantially reduced. Direct verification, with an unscaled simulation, is not feasible in free-running simulations due to the excessive background noise. For future simulations the nudging approach represents an opportunity to achieve a better signal to noise ratio without scaling. However, it is necessary to ensure that RA and SF are fully evolving under these conditions, which has been questioned by Forster et al. (2016). The EMAC model setup developed for the present thesis provides an ideal basis for such further research work (refer to Righi et al., 2021, where the technique has been used to identify significant signals for aerosol-cirrus effects from aviation).

5.2 Comparison of ECHAM5-CCMod with EMAC-CCMod results

For the second part of the present thesis the model system was switched to the EMAC/MESSy model environment, which provides a well established and ready to use MLO sub-model (see Sect. 3.1.5). In EMAC the contrail cirrus parameterization (CCMod) was implemented into the Kuebbeler et al. (2014) (K14) cloud scheme instead of the Lohmann et al. (2010) scheme (LF10), which is used for the ECHAM5 simulations. Additionally, the aerosol module (see Sect. 3.1.2) is different. The associated PRP feedback analysis, to determine RAs and SFs, was fully revised for EMAC, yet only in the technical sense. As the tuning parameter setup of ECHAM5-CCMod resulted in an inadequate large radiative imbalance when applied to the EMAC-CCMod model, a retuning of the model was required to enable the coupling of the MLO. Some of these differences, are potential sources for deviating model results between ECHAM5-CCMod and EMAC-CCMod. A detailed comparison of both models, including a description of the tuning process and an evaluation against literature, can be found in Appendix A. This section focuses on comparing contrail cirrus properties derived with the ECHAM5-CCMod and EMAC-CCMod model, as well as radiative forcings and RAs, and discusses the origin of differences.

5.2.1 Contrail cirrus cover

As obvious from the previous section, the differences between both model setups lead to deviations in the radiative forcing (see Table 4.1 and Table 4.2) and RA results (see Fig. 4.2 and Fig. 4.5), which demands an extra discussion. The global mean overlapped contrail cirrus cover is smaller for EMAC-CCMod (7.41 %) than for ECHAM5-CCMod (8.27 %), based on the ATR-12 evaluation simulations presented in Appendix A. Fig. 5.2 shows a lower contrail cirrus cover of EMAC-CCMod mostly between 0° and 30°N. This might be a consequence of a positively biased natural cloud cover around the tropics in EMAC, as described by Righi et al. (2020), leaving less space for contrail cirrus. The global mean natural cloud cover at 240 hPa (see Table A.2) and respective zonal profiles around the equator (not shown) are indeed larger for EMAC-CCMod and therefore underpin this hypothesis.

5.2.2 Contrail cirrus radiative forcing

In some contrast to the contrail cover results contrail cirrus radiative forcing of all types are consistently larger for EMAC-CCMod, in case of the ATR-12 simulations. First speculations about the origin were directed towards the increased inhomogenity factor for ice clouds (zinhomi) in EMAC-CCMod (see Table A.1), which is a typical tuning factor in the radiation scheme of ECHAM5 and EMAC (Jöckel et al., 2016; Mauritsen and Roeckner, 2020, supplement). The ice cloud inhomogenity factor enters the calculation of LW optical depth as a linear factor for both natural and contrail cirrus and thus larger values

directly result in an increased LW optical depth. However, no evidence for larger LW parts of the radiative forcing were found in the simulation data. The ratio between SW and LW RF_{adj} ($RF^{SW}_{adj}/RF^{LW}_{adj}$) of the EMAC-CCMod simulations (0.50) is in fact slightly larger than for ECHAM5-CCMod (0.48), indicating a stronger LW radiative forcing proportion for ECHAM5-CCMod. However, as shown in Appendix A, the RF_{adj} values are not deviating at all for the unscaled ATR-1 simulation (ECHAM5-CCMod: 60.0 Wm^{-2}, EMAC-CCMod: 60.7 Wm^{-2}). The corresponding zonal distributions of ECHAM5-CCMod and EMAC-CCMod agree well for ATR-1 (not shown). This strongly suggests that the scaling behavior of both models is different and might be somehow connected to the improved natural cirrus cover around the equator in EMAC-CCMod. Another clear physical origin of the greater RF_{adj} for EMAC-CCMod (ATR-12) can be found in a 8 % larger contrail cirrus in-box IWC, compared to ECHAM5-CCMod (vertically integrated, not at 240 hPa). Along with that, the respective effective radius is about 6 % smaller for ECHAM5-CCMod.

5.2.3 Contrail cirrus rapid radiative adjustments

As shown in Tables 4.1 and 4.2, the reduction of ERF, with respect to RF_{adj}, is noticeably stronger for ECHAM5-CCMod in the ATR simulations. Application of the feedback analysis revealed that the largest contributions to ERF reduction is provided by the natural cloud RA, which is almost twice as large in ECHAM5-CCMod compared to EMAC-CCMod. Nevertheless, the corresponding ratios between the SW and LW parts of both natural cloud RAs are in good agreement for both models. While the land surface temperature dependent Planck RA is comparably sized, the lapse rate RAs is considerably larger for the EMAC-CCMod simulation. Accordingly, the surface temperature increase of both models is similar (+0.012 K in ECHAM5-CCMod, +0.011 K in EMAC-CCMod), while the tropospheric temperature increase is significantly greater for EMAC-CCMod (compare Fig. 4.3 c and Fig. 4.6 c). Partly, this effect might be a consequence of the overall optically thicker contrail cirrus in EMAC-CCMod, which also leads to an increased RF_{adj}, as explained above. In parallel, the water vapor adjusts to the tropospheric temperature change and results in a corresponding smaller water vapor RA for ECHAM5-CCMod. However, both models agree well, when the directly and indirectly on temperature dependent Planck, lapse rate and water vapor RAs are combined. Overall, the impact of these three RAs is close to zero, which is similar to the behavior often found in CO_2 perturbed simulations (Cess, 1975; Bony et al., 2006).

Therefore, the negative natural cloud RA is the main contributor to ERF reduction in the ATR simulations. This effect, however, is substantially stronger for ECHAM5-CCMod (-63 %) than for EMAC-CCMod (-34 %). The physical origin can be traced back to a weaker reduction of natural cirrus cover in EMAC-CCMod (compare Fig. 4.3 a and Fig. 4.6 a). Deviations might arise from the utilization of two different cloud schemes (LF10 in ECHAM5-CCMod and K14 in EMAC-CCMod), which is qualitatively confirmed by the fact that both natural cloud RAs also differ substantially (even in sign) in CO_2-12 (see Fig. 4.4 and Fig. 4.8). Cloud RA derived for other forcers than contrail cirrus are already well known for their large spread among models, with deviations even in sign (compare to

Vial et al. (2013), their Fig. 2 and Smith et al. (2018), their Fig. S3 in the supplement). Compared to those multi-model ensembles the positive natural cloud RA found for the EMAC-CCMod CO_2 increase simulations are substantially more matching than the negative natural cloud RA determined for ECHAM5-CCMod. Thus, for a fair comparison of both models with respect to the reduction of contrail cirrus ERF, the ERF/RF_{adj} ratios have to be set in relation to their corresponding CO_2 reference simulations. As later shown in Sect. 5.3.3, the ERF reductions of both models agree considerably better if normalized with the respective CO_2 results (ECHAM5-CCMod: -58 %, EMAC-CCMod: -45 %).

In summary, the discrepancies between the ECHAM5-CCMod and EMAC-CCMod model regarding contrail cirrus properties may be surprising for two models that have so much in common, but can be attributed to model differences that nonetheless exist. The utilization of a different cloud scheme and aerosol module in combination with a required retuning are most likely responsible for noticeable, deviations in contrail cirrus physical and optical properties between both models which seem, however, not to be crucial for the RF_{adj} results. Larger deviations were found for the ERFs, i. e. for the feedback and response behavior of the model. This is not unusual in multi-model comparisons (see Smith et al., 2018; Richardson et al., 2019). While one may feel somewhat uneasy about the considerable differences in ERF/RF_{adj} between the two models for both contrail cirrus and CO_2, more important for the purpose of the present thesis is the $ERF(ATR)/ERF(CO_2)$ ratio which is far more consistent in indicating a substantially reduced climate impact of contrail cirrus. Yet, the comparison between ECHAM5-CCMod and EMAC-CCMod once more emphasizes the large potential inter-model spread with simulating RAs and SFs, and it recalls the importance of having more than one model result available to ensure reliable conclusions, as was already expressed by Bickel et al. (2020).

5.3 Comparison with literature

In recent years, much effort was invested to improve the level of scientific understanding of contrail cirrus, which is still considered to be low (Lee et al., 2021; Szopa et al., 2021). This includes the contribution of contrail cirrus to the global climate change, which is still characterized by large uncertainties (compare to the ERF estimation derived by Lee et al. (2021) of 57.4 mWm^{-2} with an inter-model spread expressed as 5-95 % confidence interval of $\pm 40.5\,mWm^{-2}$). So far the climate impact of contrail cirrus was almost exclusively analyzed on the basis of conventional radiative forcings (RF_{adj} and RF_{inst}). Only very few recent studies provide estimations for the successor metric and recommended for use ERF (IPCC, 2013). Direct determination of the contrail cirrus induced surface temperature change with coupled ocean simulations had not been available at all by the beginning of my work. The same applies to contrail induced RAs and SFs, which were for the first time completely determined in the context of the present thesis. For this reason, the evaluation against literature is mainly limited to findings concerning radiative forcings. However, the CO_2 increase simulations can be accessed as reference to evaluate the general model

performance. CO_2 represents the best understood climate forcing agent and results for all quantities under consideration here are widely available.

5.3.1 RF_{adj}, ERF and rapid radiative adjustments of contrail cirrus

The original version of the contrail cirrus parameterization (CCMod) for ECHAM5 was developed by Bock (2014), who also calculated RF_{adj} for the 2006 and 2050 AEDT air traffic dataset: 56 mWm^{-2} (Bock and Burkhardt, 2016b) and 160 mWm^{-2} (Bock and Burkhardt, 2019), respectively. Also based on ECHAM5-CCMod, respective RF_{adj} of 60 mWm^{-2} (calculated as part of the evaluation simulations in Appendix A) and 169 mWm^{-2} were derived within the present thesis. Both values are slightly larger than in the simulations performed by Bock and Burkhardt (2016b, 2019), but still very close. The deviations mainly originate in a different setup of the two radiative transfer calls, with only the first one feeding back into the model and the second one being purely analytical. While the present thesis performs the radiative double calling technique in a backward setup, where the perturbation (contrail cirrus) is removed in the second radiation calculation, Bock and Burkhardt (2016b, 2019) used the forward approach, where the perturbation is added in the second radiation call, meaning that the radiative impact of contrail cirrus has no effect on the model. The backward approach used here seems to be more consistent, as the model "feels" both, the thermodynamical and radiative presence of contrail cirrus, in contrast to Bock and Burkhardt (2016b) and Bock and Burkhardt (2019), where only the thermodynamical impact is fed back into the model.

For EMAC-CCMod unscaled RF_{adj}s were calculated for the 2006 air traffic (61 mWm^{-2}, calculated as part of the evaluation simulations in Appendix A) and for the 2050 air traffic (188 mWm^{-2}). The RF_{adj} derived with 2006 air traffic suggests a high degree of consistency between the ECHAM5 and EMAC model. For the ATR-1 and ATR-12 simulations with 2050 air traffic, EMAC-CCMod leads to a somewhat larger RF_{adj} (+11 % and +18 %), which is most likely a consequence of different scaling behavior between both models, as described in Sect. 5.1. Considering the high level of parameter uncertainty in contrail cirrus radiative forcing modeling (e. g. Lee et al., 2010; Kärcher, 2018; Lee et al., 2021), the overall estimations for the year 2006 from the EMAC-CCMod and ECHAM5-CCMod model world agree well with each other and also with the majority of estimates provided by literature (e. g. Schumann and Graf (2013): 50 mWm^{-2} for 2006, Burkhardt and Kärcher (2011): 37.5 mWm^{-2} for 2005).

Due to the natural variability in the applied FSST simulations, the ERFs derived for ECHAM5, were only statistically significant (i. e. statistically larger than zero) for air traffic scalings larger than 8, which complicates a direct comparison with literature results. Nevertheless, the ERF/RF_{adj} ratios derived for ATR-12 in both models (see Table 4.1 and 4.2) can, with some justification, be applied to the respective unscaled RF_{adj} of ATR-1 (Ponater et al., 2021). That results in an estimated ERF of 63 mWm^{-2} (124 mWm^{-2}) for the 2050 inventory in ECHAM5 (EMAC), when applying the ATR-12 ratio. So far direct

ERF calculations were only determined by Chen and Gettelman (2013) who derived an ERF of 13 $\mathrm{mWm^{-2}}$ for the year 2006. In a later study, where they applied the identical air traffic dataset, as utilized here, an ERF of 87 $\mathrm{mWm^{-2}}$ was yielded for the year 2050 (Chen and Gettelman, 2016, compare to their Fig. 3a). Thus the estimations derived by Chen and Gettelman (2013) range between the ECHAM5-CCMod and EMAC-CCMod results. However, due to debatable initialization conditions of their contrail crystal size properties, the simulations performed by Chen and Gettelman (2013) were repeated for the Lee et al. (2021) Assessment Report. Their probably more consistent ERF estimate, calculated for the year 2018, has substantially increased (57 $\mathrm{mWm^{-2}}$) from the implied initialization changes. If linearly scaled to the year 2050, according to Fig. 3a of Chen and Gettelman (2016), a considerably larger ERF than for EMAC-CCMod is yielded (approximately +25 %).

Deviations might arise from different methods, which were applied, to derive the ERF. While the present thesis sticks to the FSST approach using a free-running climate model (as recommended by Forster et al., 2016), Chen and Gettelman (2013, 2016) used specified dynamics simulations, where distinct variables in the model are predefined by a climatology (nudging method). That reduces the signal-to-noise ratio substantially and enables to yield a significant ERF even without scaling. However, as pointed out by Forster et al. (2016) it is unclear whether the RAs do fully evolve under nudging conditions and thus are unlikely to form a fully valid method for determining ERFs. The noticeably smaller ERF derived in the present thesis, might be viewed as an indication for suppressed RAs in Chen and Gettelman (2016).

One key finding of the present thesis is the substantial reduction of ERF, in comparison to $\mathrm{RF_{adj}}$ by about -63 % (-34 %) in ECHAM5 (EMAC). Feedback analysis revealed that the negative natural cloud RA is mainly responsible. The effect that aircraft induced cirrus and natural cirrus compete for the water vapor available for condensation is reasonably represented in the model, as the contrail cirrus parameterization CCMod is fully embedded in the hydrological cycle (Burkhardt and Kärcher, 2009; Bock and Burkhardt, 2016a). The simulated decreases in natural cloud cover, specific humidity and radiative effect logically explain the finding of a negative natural cloud RA, which was already pointed out previously by Burkhardt and Kärcher (2011, their Fig. 4a). This dehydration effect, connected with a redistribution of humidity to lower levels, has also been found in an independent climate model setup described by Schumann et al. (2015). The competition effects were also observed in the less parameterized, high-resolution model of Unterstrasser et al. (2017). Quantitative evidence of a natural cloud RA is only provided by (Burkhardt and Kärcher, 2011), with a compensation of about 20% (-7 $\mathrm{mWm^{-2}}$), which is significantly weaker than the reduction found here. However, as also pointed out by Burkhardt and Kärcher (2011), their natural cloud RA is only indirectly estimated, based on natural-cirrus cover decrease. It is also derived from unscaled aircraft density and thus rather uncertain. In contrast, the natural cloud RA presented here is determined directly from the radiative effect of cloud changes, including contributions from clouds at all altitudes.

While observation based measurements that address the radiative impact of contrail cirrus (Graf et al., 2012; Minnis et al., 2013; Vázquez-Navarro et al., 2015) are able, with

sophisticated methodology, to separate contrail cirrus from natural cirrus clouds, it remains unclear to which extent the natural cirrus RA is covered. This knowledge, however, is necessary for evaluating the climate model results. No method is currently obvious to check the simulated natural cloud adjustment with available observations.

5.3.2 Surface temperature change, climate sensitivity parameter, efficacy parameter and slow feedbacks of contrail cirrus

For the first time the impact of contrail cirrus on surface temperature was assessed by direct simulation as part of the present thesis. The equilibrium surface temperature increase induced by contrail cirrus (+0.192 K) was found to be substantially smaller than for a CO_2 experiment (+0.916 K) with similarly sized RF_{adj}. That indicates a significantly lower climate sensitivity parameter for contrail cirrus than for CO_2, which results in an efficacy parameter as small as 0.380 (using the ERF framework). A comparison with other efficacy parameters of non-CO_2 forcings as compiled in, e. g. Marvel et al. (2016) or Richardson et al. (2019), makes it clear how outstanding this finding is. Quantitatively comparable results were found by Rap et al. (2010) who calculated an efficacy parameter of 0.31 for linear contrails (based on conventional radiative forcing). Qualitatively the effect is confirmed by Ponater et al. (2005) and Ponater (2010) who calculated a somewhat larger efficacy parameter of 0.6, again for linear contrails. Those studies also utilized climate models equipped with a MLO, closely matching the approach used here. While these earlier efficacy studies used the conventional RF_{adj} framework, their findings largely motivated the present thesis, so that the substantially reduced efficacy, found for contrail cirrus, was at least not completely unexpected.

Lee et al. (2021) provide an estimation of the efficacy for contrail cirrus, partly based on the ratio between ERF and RF_{adj}. For this reason, their efficacy only accounts for RA, but not for SF (see also Ponater et al., 2021). Thus, the ratio can only be identified with the efficacy parameter, if the basic assumption of an efficacy parameter close to unity in the ERF framework is valid for contrail cirrus (as explained at the end of Sect. 2.8, with the help of Eq. 2.14). Or in other words, if comparably sized ERFs of contrail cirrus and CO_2 result in a similar surface temperature change. As seen in Fig. 4.11, that is obviously not the case. Therefore, it is questionable that the ratio between ERF and RF_{adj} forms a sufficient equivalent for the efficacy parameter of contrail cirrus, which is largely confirmed by the directly calculated efficacy parameter derived here. While the range of respective ERF/RF ratios determined within the present thesis (ECHAM5: 0.28, EMAC: 0.66) embrace the ratio of Lee et al. (2021) (0.42), the actual efficacy parameter in the conventional framework, derived from the EMAC simulations, is significantly lower (0.208). For this reason, the efficacy published in Lee et al. (2021) may be severely overestimated by a factor of about 2.

It should be emphasized that the ERF/RF ratio given by Lee et al. (2021) (0.42) is based on the RF_{adj} and thus needs to be compared to the here derived efficacy parameter calculated with respect to RF_{adj} (0.208) and not to the efficacy parameter determined

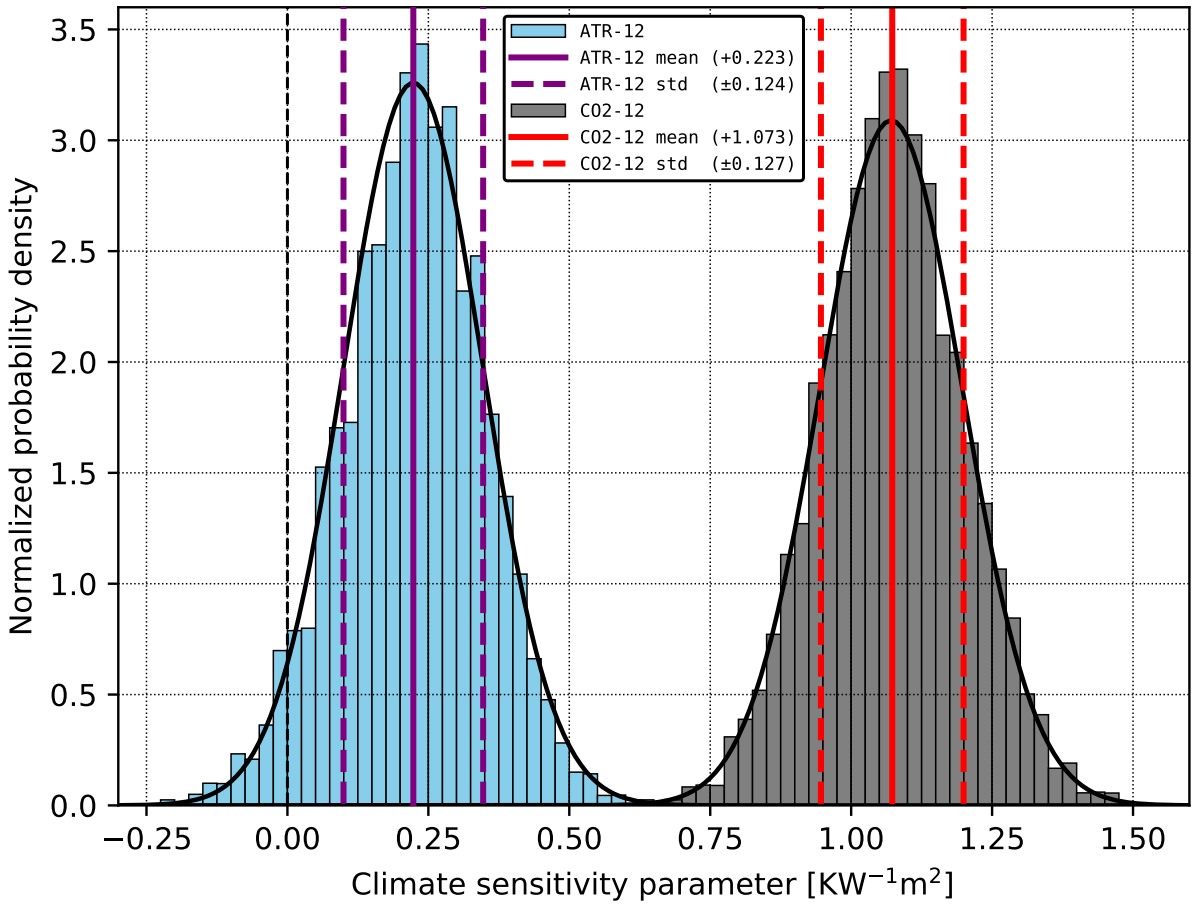

Figure 5.4: Distribution of climate sensitivity parameters derived from the ATR-12 (blue) and CO_2-12 (gray) simulations, calculated with the bootstrap method, analogously to Fig.4.11. Note that these climate sensitivity parameters were calculated with the RF_{adj}, instead of the ERF, which was the framework used in Fig. 4.11. The respective mean values are depicted by vertical solid lines and the standard deviations by vertical dashed lines (calculated after Díaz-Francés and Rubio, 2013).

within the ERF framework (0.380). The difference is highlighted in Fig. 5.4, which shows the distributions of climate sensitivity parameters, based on RF_{adj}, for contrail cirrus and CO_2. By dividing both climate sensitivity parameters, the substantially reduced efficacy parameter of 0.208 is yielded. Compared to Fig. 4.11, which shows the respective distributions for the ERF framework, both climate sensitivity parameters differ significantly stronger here and therefore emphasize the reduced impact of contrail cirrus to warm Earth's surface.

5.3.3 Role of CO_2 increase simulations

For reasons related to the historical development of the radiative forcing concept, the climate sensitivity and efficacy parameters of different forcers are usually compared relative to a CO_2 perturbation as the reference case (Hansen et al., 2005; Ramaswamy et al., 2018). Accordingly, the CO_2 increase simulations performed for the present thesis serve primarily as reference to evaluate the climate impact of contrail cirrus. By comparing the ERF/RF_{adj} ratio of contrail cirrus and CO_2 respectively first deviations between both forcing types regarding RAs can be estimated. However, to determine the actual efficacy parameter of contrail cirrus, not only the climate sensitivity parameter of contrail cirrus but also that of CO_2 is needed (see Eq. 2.13). That requires equivalent FSST simulations to determine the respective radiative forcings and consistent simulations with interactive ocean in order to calculate the surface temperature change. Results in literature indicate that the climate sensitivity parameter of CO_2 is not independent of the forcing magnitude, but rather tends to increase slightly with the forcing (e. g. Boer and Yu, 2003b; Hansen et al., 2005; Jonko et al., 2012; Meraner et al., 2013; Rieger et al., 2017). For this reason, the respective CO_2 perturbations were chosen so that the RF_{adj} of contrail cirrus and CO_2 are nearly equally sized, in order to guarantee a fair comparison*. The CO_2 doubling simulations were performed to consolidate the analysis of the CO_2-12 simulation in a statistical sense and to facilitate the comparison with results from literature. This section aims to highlight the importance of CO_2 simulations for the evaluation of contrail cirrus climate impact. A detailed comparison of the CO_2 radiative quantities against literature, can be found in Appendix B. However, some important findings are already mentioned here.

As discussed at the end of Sect. 2.8, on the basis of Eq. 2.14, the efficacy parameter can be identified with the ratio between ERF and RF_{adj} if certain conditions are fulfilled. One requirement was that the ERF of CO_2 should be approximately equal to the corresponding RF_{adj}. As shown in Table 4.1 and 4.2 this is neither the case for ECHAM5-CCMod nor for EMAC CCMod simulations. However, as pointed out in Appendix B, Smith et al. (2018) found almost similar RF_{adj} and ERF for the multi-model mean in their study of 11 independent climate models. For this reason, the ERF/RF_{adj} ratio of unity for CO_2 assumed in Lee et al. (2021) can be regarded as reasonable.

Deviations of the ECHAM5-CCMod and EMACCCMod model from literature might potentially be related to the reintroduced saturation adjustment (see Sect. 3.1.3), while deviations between both models are clearly a consequence of differently acting natural cloud RAs (compare Fig. 4.4 and Fig. 4.8). The natural cloud RA in ECHAM5-CCMod is slightly negative (-14 mWm^{-2}), while that in EMAC-CCMod is positive (+201 mWm^{-2}). Nevertheless, as the origin of those deviations is also included in the contrail cirrus simulations, they potentially cancel out to some extent when comparing contrail cirrus against CO_2. In order to account for this effect, the ERF/RF_{adj} ratio of contrail cirrus may be normalized with the corresponding inverse ratio of CO_2 (analogously to the efficacy parameter

*This implies that the magnitudes of the equivalent CO_2 increases used for the CO_2 simulations in the present thesis are independent of CO_2 increases actually induced by aircraft emissions

calculation shown in Eq. 2.13):

$$\text{ratio}_{\text{normalized}} = \frac{\text{ERF}_{\text{contrail cirrus}}}{\text{RF}_{\text{contrail cirrus}}} \cdot \frac{\text{RF}_{\text{CO}_2}}{\text{ERF}_{\text{CO}_2}} \tag{5.1}$$

As evident from Table 4.1 and 4.2, the ERF to RF_{adj} ratio for ATR-12 turns out to be significantly smaller in ECHAM5-CCMod (0.37) than in EMAC-CCMod (0.66). If normalized following Eq. 5.1, a $\text{ERF}/\text{RF}_{\text{adj}}$ ratio of 0.42 (0.55) for contrail cirrus can be calculated for ECHAM5-CCMod (EMAC-CCMod). Thus the overall weaker contrail cirrus ERF reduction in the EMAC-CCMod model is partly compensated by accounting for increasing natural cloud RA and their effect on ERF also in the corresponding CO_2-12 simulation (see Sect. 5.2.3). Therefore, the deviation between both models, with respect to the contrail cirrus versus CO_2 response, is smaller. Both ratios, derived here, do not only match better with each other, but also fit considerably better to the ratio provided by Lee et al. (2021, 0.42).

5.4 Is the climate impact of contrail cirrus still important?

5.4.1 Contribution of contrail cirrus to global warming

So far, contrail cirrus has been regarded to be the largest contributor to aviation induced conventional radiative forcing (RF_{adj}) and effective radiative forcing (ERF), even larger than accumulated aviation CO_2 (Lee et al., 2021, and references therein). The corresponding ratio of the conventional radiative forcing induced by contrail cirrus to the conventional radiative forcing of CO_2 is 3.2 (see Table 5.1). The respective ratio based on ERF is 1.7 (see also Table 5.1).

No surface temperature change estimates are given by Lee et al. (2021) and most of the results of the present thesis are derived from scaled 2050 air traffic inventories, thus no direct comparison of numbers is possible. However, climate sensitivity and efficacy parameters enter the relation, linking radiative forcing and surface temperature change, as multiplication factors (see Eq. 2.11 and e. g. Fuglestvedt et al., 2010). Thus, the climate sensitivity parameters, derived here for contrail cirrus and CO_2, can be multiplied with the corresponding radiative forcings of Lee et al. (2021), to estimate the equilibrium surface temperature response for the year 2018[†]. If combined, a surface temperature increase of about +0.025 K and +0.037 K is yielded for contrail cirrus and CO_2 respectively, based on RF_{adj}. For ERF the estimated surface temperature increase yields +0.019 K for contrail cirrus and +0.030 K for CO_2, respectively (see Fig. 5.5). The corresponding ratios between

[†]Note that the equilibrium surface temperature response is derived by applying constant perturbations for the respective target year and does not correspond with the actual surface temperature change that could be expected for that year. To derive the real surface temperature response for the respective year a transient simulation with adapting perturbations is required (e. g. Frömming et al., 2012, see their Fig. 11)

Table 5.1: Ratios between contrail cirrus and CO_2 radiative forcings and surface temperature changes. The radiative forcings are based on Lee et al. (2021) while the surface temperature changes are derived by multiplying those forcings with the respective climate sensitivities yielded in the present thesis (compare also to Fig. 5.5)

	Ratio (contrail cirrus / CO_2)
RF	3.2
ERF	1.7
$RF \cdot \lambda_{RF}$	0.7
$ERF \cdot \lambda_{ERF}$	0.6

the contrail cirrus and CO_2 surface temperature change are 0.7 in the conventional framework and 0.6 in the ERF framework (see Table 5.1). Thus, the climate impact on surface temperature change is larger for CO_2 than for contrail cirrus, even if both radiative forcings suggest the opposite. For this reason, the new results presented here, with respect to feedbacks, climate sensitivity and efficacy parameters of contrail cirrus, challenge the current notion of a leading role of contrail cirrus in controlling aviation climate impact. Note that the statistical uncertainties of the radiative forcings shown in Fig. 5.5 are those of Lee et al. (2021) and based on the inter-model spread, while those of the climate sensitivity are derived from the statistical variability simulated in the present thesis.

These findings suggest important consequences for future mitigation strategies, regarding the climate impact of aviation. In the current IPCC Assessment Report re-routing of air traffic is considered to have high potential to avoid the formation of persistent contrails in ice super-saturated areas (Jaramillo et al., 2022). However, the gains in terms of aviation climate impact reduction become less distinct when reflected in the context of the present thesis. Non-contrail forcers like CO_2 or NO_x potentially gain in importance. To evaluate the actual consequences of the reduced climate impact of contrail cirrus for future mitigation scenarios, a complete re-assessment, including all forcers induced by air traffic, is once again needed. In order to account for all possible trade-offs, the method presented by Yamashita et al. (2020) might provide an ideal basis for this purpose. Anyway, avoidance of contrails with a positive radiative forcing will remain desirable if it can be achieved without significant additional CO_2 emissions. If contrail avoidance demands higher fuel consumption for a particular situation, then the results of the present thesis strongly question the effectiveness of respective mitigation attempts.

5.4.2 Regional climate mitigation measures versus global climate impact

As expressed by, e. g., Ramaswamy et al. (2018), radiative forcing is basically a global climate metric. However, it originates from regional contributions that may strongly vary in space and time, especially for contrails and contrail cirrus. The ratios given in Table 5.1 are meaningful on the global scale only and are not applicable to the respective parameters on

the regional scale. There is no such thing like a constant climate sensitivity parameter valid for all regions or seasons (e. g. Boer and Yu, 2003a). This implies that measures developed for contrail mitigation on the regional scale may still be evaluated using RF as a metric. Only assessments aiming at measures for limiting global warming have to consider the reduced contrail cirrus efficacy determined in the present thesis. Hereafter, some examples are discussed to illustrate deviations of the regional from the global perspective.

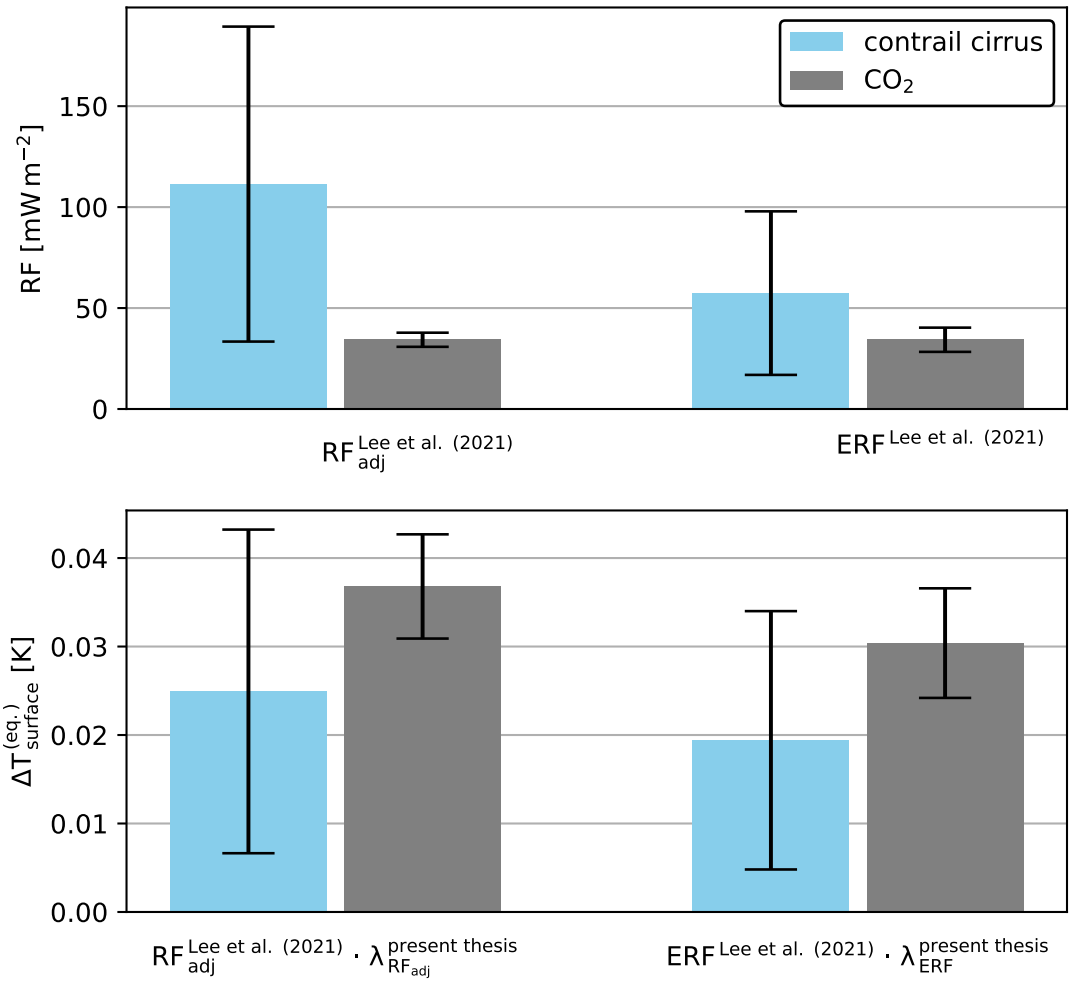

Figure 5.5: Estimation of the actual contrail cirrus climate impact on surface temperature. The top panel recalls, as the starting point, the conventional and effective radiative forcings given by Lee et al. (2021) for the year 2018. The bottom panel shows the equilibrium surface temperature changes†, which were derived by multiplying the climate sensitivities of the present thesis with the radiative forcings of Lee et al. (2021). Whiskers of the radiative forcings show the 5-95 % confidence intervals of the inter-model spread given by Lee et al. (2021). Whiskers of the surface temperature change were estimated by combining the uncertainties of the radiative forcings mentioned above with the statistical uncertainties derived for the climate sensitivity parameters of the present thesis.

One aspect closely related to the results of the present thesis is, that feedback analysis has revealed negative natural cloud RA to be in large parts responsible for the reduced efficacy. This implies that contrails developing in regions where no natural cirrus clouds are expected to form will have a larger impact. The contrail cirrus itself is adequately described by its RF, but the contrail cirrus net impact depends on the local feedbacks, and (like the climate sensitivity parameter) the ERF/RF ratio must not be assumed to be constant in space and time.

This insight is somewhat linked to the considerations of Teoh et al. (2020) and Wilhelm et al. (2021), who pointed out that only very few contrail events are responsible for a disproportionately large climate impact ("big hits"). For this reason, re-routing of a very limited number of flights might still represent a considerable potential for mitigating the climate impact of contrail cirrus. As first described in Mannstein et al. (2005) a flight level change of only a few hundreds of meters is often sufficient to avoid super-saturated regions. For the respective big hits this would be worthwhile anyway without additional fuel consumption, but – if properly assessed – may still involve a global warming reduction in case of slightly increased CO_2 emissions.

Another feature of contrail cirrus impact from a confined space/time domain, that has only been addressed briefly in Sect. 4.2.1, is the different radiative impact during day and night. Contrail cirrus RF_{adj} is about one magnitude larger during night periods because of the absent reflection of SW radiation. Thus, the potential of contrail cirrus to contribute to global Earth's surface warming is largely increased during night. Stuber et al. (2006) and Stuber and Forster (2007), who analyzed this behavior for linear contrails, have emphasized the importance of contrails during night periods. For this reason, avoiding evening and night flights were assumed to bear a great potential to mitigate the climate impact of contrail cirrus and thus aviation in general. This conclusion is not affected by the results of the present thesis, as there is no obvious necessity for additional fuel consumption.

Chapter 6

Conclusion and Outlook

Air traffic is expected to continue growing exponentially in the coming decades (Jaramillo et al., 2022). So far contrail cirrus has been considered to be the largest contributor to aviation induced climate impact (e. g. Lee et al., 2009; Grewe et al., 2017; Lee et al., 2021). However, this has been demonstrated only in terms of conventional radiative forcings (RF) and effective radiative forcing (ERF). Does it remain true, if the induced temperature change is considered?

Motivated by previous studies, which indicated a reduced efficacy for linear contrails (Ponater et al., 2005; Rap et al., 2010), the present thesis set the goal to clarify whether this may also be an issue for contrail cirrus. Based on the state-to-the-art contrail cirrus parameterization CCMod (Bock and Burkhardt, 2016a), various global climate simulations were performed with two climate models (ECHAM5-CCMod and EMAC-CCMod). Besides simulations with fixed sea surface temperatures (FSST) to calculate the different types of radiative forcings, simulations with a coupled mixed-layer ocean (MLO) were performed to determine the actual surface temperature change induced by contrail cirrus. On the basis of these results, the climate sensitivity and efficacy parameters of contrail cirrus were determined for the first time. The simulations were extensively evaluated by feedback analysis in order to gain a fundamental understanding about the physical processes leading from the radiative forcings to the final surface temperature change. Altogether, the present thesis provides a comprehensive overview of the relevant radiative processes and parameters to assess the climate impact of contrail cirrus and to highlight possible consequences for mitigation strategies. Parts of the present thesis* contributed to the Lee et al. (2021) Assessment Report and to the 6$^{\text{th}}$ IPCC Assessment Report (Szopa et al., 2021), which summarize the state-of-the-art understanding of contrail cirrus climate impact.

*as far as published in Bickel et al. (2020)

6.1 Questions, Answers and Conclusions

In the following, the main findings of the present thesis are summarized by answering the questions raised in the introduction. The section closes with some concluding remarks regarding the updated climate impact of contrail cirrus.

Q1: What is the magnitude of contrail cirrus ERF when determined by the most appropriate method? How much does the ERF deviate from the conventional radiative forcing values?

To answer this question an optimal method has to be selected, above all fitting to the ERF concept and at the same time allowing to extract statistically significant signals from internal climate model variability. While ERFs for contrail cirrus have already been calculated by Chen and Gettelman (2013, 2016), their applied nudging method has been suspected to suppress the full development of rapid radiative adjustments (RA), potentially leading to an overestimated ERF (Forster et al., 2016). For this reason the present thesis sticks to the FSST method using a free-running climate model, which is recommended by Forster et al. (2016), because a correct representation of the RAs and thus of the ERF can be realized. Due to larger statistical uncertainties, coming along with this method (in comparison to the nudging approach), the underlying air traffic dataset for the year 2050 needed to be scaled by a factor of 12. Careful analysis shows that, the scaling results in different saturation and compensation effects which, however, only marginally influences the essential results.

The ERFs, based on a 12 times scaling of air traffic were found to be $568\,\mathrm{mWm^{-2}}$ (± 0.125) for EMAC-CCMod and $261\,\mathrm{mWm^{-2}}$ (± 0.102) for ECHAM5-CCMod. Both ERFs are substantially smaller compared to their corresponding conventional radiative forcings ($\mathrm{RF_{adj}}$) which have a value of $858\,\mathrm{mWm^{-2}}$ (EMAC-CCMod) and $701\,\mathrm{mWm^{-2}}$ (ECHAM5-CCMod). For comparably sized CO_2 simulations the ERFs deviated much less from $\mathrm{RF_{adj}}$. If directly compared to the corresponding CO_2 experiments, the contrail cirrus ERF is reduced by 45 % forEMAC-CCMod and by 58 % for ECHAM5-CCMod, compared to the respective conventional radiative forcing. According to the basic conceptual ideas promoting the ERF framework, these findings already indicate a reduced climate impact of contrail cirrus.

Q2: Which physical processes (rapid radiative adjustments) are responsible for the deviation between the ERF and the conventional radiative forcings?

In literature the kernel method represents the predominately used technique to derive radiative feedbacks, even though the method has only limited capabilities to determine cloud feedbacks. As clouds are in focus of the present thesis, the partial radiative perturbation (PRP) method was chosen to be used here. The PRP method determines feedbacks by a direct recalculation of the respective radiative fluxes and therefore surpasses the consistency and accuracy of the kernel method. Here the PRP method is applied in its centered version as recommended by Klocke et al. (2013) and Rieger et al. (2017). Applying it to

the FSST simulations, RAs are derived, which explain the differences between the various radiative forcings and therefore the origin of the strong reductions of contrail cirrus ERFs.

Contrail cirrus especially warms the upper part of the troposphere, directly below those regions with largest air traffic density, with a decreasing warming impact towards Earth's surface. Along with temperature, the water vapor concentration is increasing, but in this case strongest in the middle and lower troposphere. These patterns result in the directly and indirectly on temperature dependent Planck, lapse-rate and water vapor RAs to almost cancel out each other in both models. For this reason, the deviation between RF_{adj} and ERF can be attributed almost completely to the considerably large negative natural cloud RA in both models. The physical origin crucially results from a decrease of natural cirrus clouds, especially in those regions with largest contrail cirrus cover. Therefore, the reduced ERF of contrail cirrus is to a large extent caused by a compensation between evolving contrail cirrus cover that develops from available supersaturated water vapor at the expense of natural cirrus cover. This result can be subjected to verification with process models and observations.

Q3: How much does contrail cirrus warm Earth's surface ($\Delta T_{surface}$, climate sensitivity parameter)?

For the surface temperature change simulations, an interactive ocean represented by a MLO module replaced the FSST approach, in order to allow the complete Earth's surface temperature to adjust to the perturbation. These simulations were only performed with the EMAC-CCMod model.

For 12 times scaled air traffic a global mean equilibrium surface temperature increase of about +0.19 K was calculated for contrail cirrus. A CO_2 increase experiment with a similarly sized conventional radiative forcing yielded a much larger global mean surface temperature change of about +0.92 K. If combined with the corresponding ERFs, a climate sensitivity of $0.34\,KW^{-1}m^2$ and $0.89\,KW^{-1}m^2$ was derived for contrail cirrus and CO_2 respectively. The climate sensitivity parameter of contrail cirrus is thus significantly lower (by about 62 %) than that of CO_2, indicating the reduced potential of contrail cirrus to warm Earth's surface.

Q4: Does the expected global mean surface temperature change, based on radiative forcings, correspond with the directly calculated surface temperature change (efficacy parameter)?

The reduced climate impact of contrail cirrus manifests in a very low efficacy parameter of only about 0.38, if determined in the ERF framework. Such a low efficacy parameter is among the lowest values mentioned in literature for non-CO_2 radiative forcings (Marvel et al., 2016; Richardson et al., 2019). For this reason the theoretically expected surface temperature change, based on ERF and efficacy parameters close to unity, is clearly inconsistent with the directly determined surface temperature change. If based on RF_{adj} the efficacy parameter decreases even further (0.21) and falls below the ERF/RF ratio provided

by Lee et al. (2021) by a factor of more than 2. Due to the efficacy parameter strongly deviating from unity, the ERF framework fails as a reliable predictor for contrail cirrus surface temperature change. Therefore, it is essential to directly determine the climate impact of contrail cirrus from surface temperature change simulations or at least account for the low efficacy parameters calculated here. This holds, in particular, for contrail cirrus mitigation approaches that involve increased fuel consumption.

Q5: Which physical processes (slow feedbacks) explain a potentially deviating response of the surface temperature in the case of contrail cirrus and CO_2?

The surface temperature change simulations with interactive ocean were also investigated with the PRP feedback analysis method. The derived feedback parameters (FP) explain the origin of the low surface temperature response in case of contrail cirrus.

Deviations of contrail cirrus from the reference CO_2 simulations were mainly found for the natural cloud and lapse-rate FP. The smaller lapse-rate FP of contrail cirrus can be explained by a different temperature response structure induced by contrail cirrus, with largest temperature increase directly below the maximum air traffic altitude. In contrast, CO_2 warms the atmosphere more uniformly. However, the largest deviations, even in sign, were found for the natural cloud FPs, which originate from low and mid level clouds reacting differently in contrail cirrus and CO_2 forced simulations. While those clouds, in the global mean, show a slight growth in the contrail cirrus simulation, they significantly decrease for the CO_2 simulation. The natural cloud and lapse-rate SF are working in the same direction, thus inducing the substantially reduced contrail cirrus efficacy and weak surface temperature response.

6.2 An important conclusion of the five answers

The implications of the reduced efficacy of contrail cirrus can be clearly demonstrated by multiplying the radiative forcings provided by Lee et al. (2021) with the climate sensitivity parameters derived in the present thesis. If combined in this way, the equilibrium surface temperature change induced by contrail cirrus is about 35 % lower than that of the air traffic CO_2 emissions. A similar reduction factor can be expected for the temperature response all along the way towards temperature equilibrium (Ponater et al., 2005). For this reason the supposed role of contrail cirrus as the leading forcer of aviation climate impact is questioned by the findings of the present thesis, even if the radiative forcings suggest the opposite. It has to be mentioned, however, that previous inter-model comparison projects for other forcers (CO_2 as well as non-CO_2 effects) often revealed partially strong deviations between the individual climate models (Andrews et al., 2012; Vial et al., 2013; Smith et al., 2018). Therefore, independent simulations with other climate models and contrail cirrus parameterizations are highly desirable to confirm the results derived here.

6.3 Outlook

While the principle questions of the present thesis could all be answered satisfactorily, there is potential to further consolidate the results presented here possibly even making improvements, in both the statistically and the methodological sense.

One matter of concern is the scaling of the underlying air traffic density by a factor of 12 that was needed in order to ensure statistically significant results. That leads to different saturation and compensation effects, which evidently influence the results only to a marginally extent. While lower scalings of air traffic might be possible with the EMAC-CCMod setup, scaling can not be completely avoided when using the free-running model. As an alternative to scaling, the nudging method might be worth testing (e. g. Feichter and Lohmann, 1999; He et al., 2017; Righi et al., 2021). Nudging reduces the statistical uncertainties by prescribing or relaxing certain variables in the model (e. g. pressure or wind). Chen and Gettelman (2013, 2016) have already demonstrated that this method is capable of calculating statistically significant contrail cirrus ERFs completely without scaling. However, Forster et al. (2016) expressed a warning that RAs may not fully evolve under nudged conditions. Yet, as the RAs were already determined with the appropriate FSST method using the free-running GCM here (Forster et al., 2016), the EMAC-CCMod framework provided by the present thesis represents an ideal basis for a comparison between both methods as nudging is a tested option in the EMAC model (Jöckel et al., 2016; Righi et al., 2021). If successfully evaluated with respect to its feedback characteristics, the nudging method creates the opportunity to determine unscaled and statistically significant ERFs and RAs for contrail cirrus. Furthermore, the nudging method might also be applied to the temperature change simulations with interactive ocean, in order to directly determine the contrail cirrus climate impact on surface temperature without scaling. This, however, would enter largely unexplored territory in climate research.

As mentioned at the end of Sect. 5.4 the air traffic dataset utilized in the present thesis features no diurnal cycle. While this allows for a fair evaluation of contrail cirrus radiative impact between day and night periods (which resulted in a radiative forcing close to zero for day periods and in an approximately doubled net forcing for night periods) it is not sufficient to address mitigation options targeting at contrail avoidance at night (Myhre and Stordal, 2001; Stuber et al., 2006; Newinger and Burkhardt, 2012). However, in order to realistically reproduce the real world aviation climate impact and to evaluate realistic mitigation attempts, the representation of the actual diurnal cycle of air traffic is highly desirable. For this purpose, air traffic datasets with diurnal cycles are already in preparation.

By using feedback analysis to identify physical reasons for varying ERF/RF ratios and efficacy parameters, the present thesis provides a basis for respective process evaluation. This encourages, in particular, the use of process models (and eventually observations) to verify the competition between contrail cirrus and natural cirrus for available supersaturated water vapor. The same holds for differences in the lapse-rate feedback induced by contrail cirrus and CO_2, building on, e. g., studies like Schumann and Mayer (2017). However, evaluation of cloud radiative effects and their origins has been a main focus of the

present thesis. For this purpose the corresponding vertical radiative flux profiles have been decomposed into upward and downward fluxes. To further improve the understanding of cloud radiative effects, Salvi et al. (2021) introduced a method to explain differences in natural cloud RA between two forcers with the help of vertical heating rate profiles. That evaluation method might be worth testing in future simulations to be analyzed.

Finally it has to be mentioned that the radiative transfer parameterization utilized in both, the ECHAM5 and EMAC model, is pretty much at its limits when working with contrail cirrus. Due to the transition from geometric to Mie scattering for small particles, the smallest possible ice particle radius is set to 10 µm in both models (for a detailed description see Appendix A of Bock and Burkhardt, 2016a). However, the effective radius of contrail cirrus particles is often slightly below this threshold, especially in regions with large air traffic density, were the ice particles can't grow due to limited ambient water vapor. For this reason, an optimized radiative transfer parameterization, that can handle contrail cirrus effective radii smaller than 10 µm would be a valuable improvement for both climate models used here.

On the whole, the present thesis provides enough new evidence to include the aspect of efficacy reduction in further mitigation studies of contrail cirrus, often having been omitted so far (e. g. Fuglestvedt et al., 2008; Klöwer et al., 2021). This is especially important if contrail avoidance requires higher CO_2 emissions, as has been demonstrated in few previous publications (e. g. Deuber et al., 2013; Irvine et al., 2014).

Appendix A

Model tuning and evaluation

The CCMod implementation in EMAC is largely based on the EMAC-MADE3 setup (Righi et al., 2020). In addition to the contrail cirrus parameterization, the saturation adjustment had to be reintroduced (see Sect. 3.1.3), which means that the coding of the modifications described by Bock and Burkhardt (2016a) for the Lohmann and Ferrachat (2010) cloud parameterization in ECHAM5 had to be repeated for the Kuebbeler et al. (2014) scheme used in EMAC-MADE3. The saturation adjustment severely affects the model's cloud physics, so that a complete retuning of the model was required. There are typical tuning parameters to be used for this purpose (e. g. Mauritsen et al., 2012; Righi et al., 2020). A central objective was to keep the TOA radiative imbalance below $\pm 0.5\,\mathrm{Wm}^{-2}$, in order to enable the coupling of a MLO (see Sect. 3.1.5). However the tuning parameters should also be kept as close as possible to the ECHAM5-CCMod model which was carefully tuned and evaluated against observations by Bock and Burkhardt (2016a,b). Adapted tuning parameters were exclusively changed in the direction of the underlying EMAC-MADE3 tuning setup (Righi et al., 2020).

Table A.1: Summary of the chosen tuning parameters for the ECHAM5-CCMod and EMAC-CCMod model.

tuning parameter	**model variable**	**ECHAM5-CCMod**	**EMAC-CCMod**
cloud cover scheme	lcover	Sundqvist (1978)	Sundqvist (1978)
autoconversion rate	ccraut	0.5	4.0
aggregation rate	ccsaut	400	400
minimum CDNC [cm^{-3}]	cdncmin	40	50
diameter of newly nucleated particles [nm]	nucsize	-	10
inhomogenity factor ice clouds	zinhomi	0.7	0.85
inhomogenity factor liquid clouds	zinhoml	1.0	parameterized
asymmetry factor of ice clouds	zasic	0.85	0.85
correction for asymmetry factor of ice clouds	zinpar	-	0.08
entrainment rate for penetrative convection	entrpen	$2.5{\cdot}10^{-4}$	$1.0{\cdot}10^{-4}$
entrainment rate for shallow convection	entrscv	$3.0{\cdot}10^{-4}$	$10.0{\cdot}10^{-4}$
critical rel. humidity for cloud formation	crt	0.7	0.7
ice cloud emissivity parameterization	loice	(Rockel et al., 1991)	(Rockel et al., 1991)

First EMAC-CCMod test simulations with the original ECHAM5-CCMod tuning parameters (see Table A.1, third column) resulted in a radiative imbalance of about -5 Wm^{-2}. In addition to that, the global mean liquid water path (LWP) for natural clouds was about twice as large as results from observations. A change of the autoconversion rate (ccraut) from 0.5 to 4.0 (see Table A.1, fourth column), as set in the original EMAC-MADE3 setup, solved much of this problem. To further improve the LWP problem, the entrainment rate for penetrative and shallow convection was chosen in accordance with the EMAC-MADE3 tuning settings. The inhomogenity factor for ice clouds (zinhomi) was mainly used for tuning of the radiative imbalance at TOA and was again set after the EMAC-MADE3 tuning (0.85). However, zinhomi should be handled with utmost caution as it directly affects the radiative quantities of ice clouds, including contrail cirrus and their radiative impact. The inhomogenity factor for liquid clouds (zinhoml) is set to 1.0 in ECHAM5-CCMod, while it is parameterized in EMAC-CCMod depending on the LWP and the correction for the asymmetry factor of ice clouds (zinpar). Overall, a perfect tuning with the fulfillment of the requirements stated above is hard to achieve. Especially with the necessity of a very low radiative imbalance compromises have to be taken. The EMAC-CCMod tuning shown in Table A.1 was chosen with greatest possible care after over 30 test simulations and was utilized consistently in all EMAC-CCMod simulations of the present thesis.

Besides radiative imbalance and LWP, various model variables were monitored and evaluated against observations during those tuning tests. A subset of those variables, averaged to global mean values, is shown in Table A.2. The table features three simulations performed with the ECHAM5-CCMod model, one with the standard EMAC-MADE3 and three with the EMAC-CCMod version (all based on the FSST method). Note that the EMAC-MADE3 simulation was carried out with the tuning setup shown in the fourth column of Table A.1 and not with the original MADE3 tuning used in Righi et al. (2020). The evaluation simulations with ECHAM5-CCMod and EMAC-CCMod were performed once without air traffic, once with AEDT 2006 air traffic, and once with a 12 times scaling of the AEDT 2050 air traffic. The results were compared to observational data, consisting of satellite observations and in situ measurements (see last column of Table A.2). Note that satellite observations need to be evaluated against in-box model variables, while in situ measurements need to be compared to in-cloud variables.

The aim of both CCMod reference simulations is to verify the low radiative imbalance, as these simulations are used to calibrate the coupled MLO. A radiative imbalance of only 0.153 Wm^{-2} in case of the EMAC-CCMod simulation confirms a successful tuning effort. In comparison the radiative imbalance of the ECHAM5-CCMod model (+1.575 Wm^{-2}) would have been unsuitable for optimally coupling a MLO. The EMAC-MADE3 simulation was mainly performed as reference for comparison with EMAC-CCMod, to prove a properly working saturation adjustment in the EMAC-CCMod model. This can be verified on the basis of the natural cirrus relative humidities to ice for the cloudy and clear-sky case. Both are significantly lower in the EMAC-CCMod simulations, indicating a correct deposition of humidity above saturation.

Table A.2: Summary of global mean cloud and radiation variables for natural and contrail cirrus quantities.

		ECHAM5 CCMod 0×ATR	ECHAM5 CCMod 1×ATR[1]	ECHAM5 CCMod 12×ATR[2]	EMAC MADE3	EMAC CCMod 0×ATR	EMAC CCMod 1×ATR[1]	EMAC CCMod 12×ATR[2]	Observations
Cloud cover overlapped	[%]	64.7	64.7	64.0	66.3	68.6	68.7	68.3	68 ±5[a]
Cloud cover 240 hPa	[%]	20.3	20.1	19.3	21.6	21.7	21.7	20.9	
LWP oceans (vertical integrated; in-box)	[g m^{-2}]	83.7	84.1	84.6	97.9	96.6	96.1	97.0	83.0 ±10.2[b]
IWP (vertical integrated; in-box)	[g m^{-2}]	15.0	15.0	14.8	11.6	12.4	12.4	12.2	25 ±7[c]
WVM (vertical integrated water vapor)	[kg m^{-2}]	25.4	25.3	25.5	25.7	26.0	26.0	26.2	25.2[d]
CDNC (vertical mean; in-cloud)	[cm^{-3}]	95.2	94.4	95.0	97.7	104.3	103.6	103.6	74.0 ±41.1[e]
ICNC (vertical mean; in-cloud)	[cm^{-3}]	1.35	1.35	1.37	0.24	0.26	0.25	0.25	
Natural cirrus IWC (in-cloud)	[ppmv]				9.5	10.2	10.3	10.3	7.19 [1.66; 29.22][f]
Natural cirrus ICNC (in-cloud)	[cm^{-3}]				0.064	0.070	0.070	0.068	0.027 [0.006; 0.101][f]
Natural cirrus particle radius	[μm]				17.2	16.1	16.0	16.2	23.6 [17.0; 32.6][f]
Natural cirrus relative humidity to ice (cloudy-sky)	[%]				100.9	90.6	90.6	90.7	93.87 [84.03; 103.71][f]
Natural cirrus relative humidity to ice (clear-sky)	[%]				56.5	42.5	47.5	47.7	47.87 [30.16; 69.18][f]
Precipitation convective	[mm d^{-1}]	1.79	1.79	1.78	2.10	2.04	2.05	2.02	
Precipitation stratiform	[mm d^{-1}]	1.16	1.16	1.16	1.06	1.06	1.06	1.07	
Precipitation total	[mm d^{-1}]	2.95	2.95	2.93	3.16	3.10	3.10	3.08	2.7 ±0.2[g]
SWCRE (TOA)	[W m^{-2}]	−42.9	−43.2	−43.7	−53.4	−54.5	−54.5	−55.4	−45.9 ±5.5[h]
LWCRE (TOA)	[W m^{-2}]	+21.2	+21.2	+21.9	+24.1	+26.5	+26.6	+27.7	+28.1 ±4.4[h]
Radiative imbalance (TOA)	[W m^{-2}]	+1.575	+1.296	+0.911	−0.660	+0.153	+0.197	−0.388	
Aerosol optical depth oceans (550 nm)		0.150	0.146	0.149	0.107	0.110	0.112	0.110	0.116[i]
Contrail cirrus cover overlapped	[%]		1.22	8.27			0.91	7.41	
Contrail cirrus cover 240 hPa	[%]		0.55	3.05			0.43	2.81	
Contrail cirrus IWC 240 hPa (in-cloud)	[mg m^{-3}]		1.366	2.593			1.607	2.862	[0.1; 100][j]
Contrail cirrus ICNC 240 hPa (in-cloud)	[cm^{-3}]		0.89	12.12			0.88	10.69	[0.1; 100][j]
Contrail cirrus effective radius 240 hPa	[µm]		11.75	8.19			12.53	9.33	[0.05; 30][j]
Contrail cirrus optical depth 240 hPa (in-cloud)			0.119	0.399			0.133	0.415	[0.05; 0.8][j]
Contrail cirrus optical depth total (in-box)			0.0028	0.0612			0.0024	0.0646	
Contrail cirrus RF_{adj}	[mW m^{-2}]		60.0	715.1			60.7	858.5	

[1] based on the 2006 AEDT air traffic dataset
[2] based on the 2050 AEDT air traffic dataset
[a] after Stubenrauch et al. (2013), derived from multiple satellite observations
[b] after Righi et al. (2020), based on the MAC dataset (Elsaesser et al., 2017), derived from satellite observations
[c] after Neubauer et al. (2019), based on satellite observations compiled by Li et al. (2012b)
[d] after Vonder Haar et al. (2012), based on the NASA Water Vapor Project (NVAP) dataset, derived from satellite observations
[e] after Righi et al. (2020), based on in situ measurements by Karydis et al. (2011, 2017); Flamant et al. (2018); Taylor et al. (2019)
[f] after Righi et al. (2020), based on in situ aircraft measurements by Krämer et al. (2009, 2016, 2020)
[g] after Neubauer et al. (2019), based on results from Adler et al. (2012, 2018)
[h] after Righi et al. (2020), based on the CERES-EBAF dataset (Loeb et al., 2018), derived from satellite observations
[i] after Alfaro-Contreras et al. (2017), derived from satellite observations
[j] after Schumann et al. (2017); Schumann and Heymsfield (2017), derived from various airborne, satellite and ground-based observations

Finally, two CCMod simulations with the unscaled AEDT 2006 air traffic dataset were performed, in order to intercompare and evaluate the contrail cirrus quantities against observations. Air traffic density is about 28 times and water vapor emissions are about 58 times smaller for the unscaled 2006 AEDT air traffic dataset than for the 12 times scaled 2050 AEDT one applied in the main part of the present thesis.

The overlapped contrail cirrus cover is about 0.3 % (0.9 %) larger for ECHAM5-CCMod than for EMAC-CCMod with the unscaled AEDT 2006 (12 times scaled AEDT 2050) dataset. Contrail cirrus coverage grows partly at the expense of natural cirrus clouds (see second line of Table A.2), which is more pronounced for the simulations with scaled air traffic. Contrail cirrus IWC, ICNC and effective radius agree relatively well for both models when comparing simulations with the same scaling respectively. However, in EMAC-CCMod the contrail cirrus ice particles seem to be larger, in combination with a smaller ICNC. Similar to the IWC, the contrail cirrus optical depth is slightly larger in EMAC-CCMod. Locally, e. g. over Europe, the eastern part of the USA or Japan, the total optical depth can reach values up to 0.1 (1.0) for the unscaled AEDT 2006 (12 times scaled AEDT 2050) dataset. Changing the air traffic scaling has a larger impact on contrail cirrus ICNC than on IWC. Overall, the contrail cirrus properties derived by both CCMod models, with both air traffic setups, are well within the range of observational data compiled by Schumann et al. (2017) and Schumann and Heymsfield (2017). Unfortunately, to date, there are no global mean measurements available for evaluating contrail cirrus properties.

Most of the remaining variables of ECHAM5-CCMod agree well with the observational data. Due to the tuning of the radiative imbalance, some variables diverge more strongly for the EMAC-CCMod setup, but are mostly within the range of observational uncertainties. The IWP is underestimated in both models, which motivated Bier and Burkhardt (2019) to lower the aggregation rate to 75. This might be worth testing in future tuning efforts, although Righi et al. (2020) indicate that smaller aggregation rates result in larger deviations for natural cirrus IWC and ICNC. In addition, the MLO simulations, presented in Section 4.2.3, revealed a considerably large surface temperature reaction for the CO_2 increase experiments in comparison to previous results, derived with the EMAC model (compare to Dietmüller et al., 2014, , their Table 3), which might be a consequence of the new tuning in combination with the reintroduced saturation adjustment.

Another key variable regarding contrail cirrus formation is the frequency of ice supersaturation. This parameter determines the maximum amount of persistent contrail cirrus coverage that can be formed within a grid box (Burkhardt et al., 2008). Fig. A.1 shows the frequency of ice supersaturation of the ECHAM5-CCMod and EMAC-MADE3 reference simulation, compared to Atmospheric Infrared Sounder (AIRS) satellite observations (Lamquin et al., 2012). Similar plots have been shown in Bock (2014) and Bock and Burkhardt (2016a).

Overall the results of the EMAC-CCMod model agree exceptionally well with those of the ECHAM5-CCMod model. Between 200 hPa and 250 hPa, where most of the air traffic takes place, the models are able to reproduce the frequency of ice supersaturation successfully. One layer above, between 150 hPa and 200 hPa, model predictions are considerably overestimating the AIRS observations above 30°N and below 30°S. Compared to Fig. 3.1

there is quite a substantial amount of air traffic flying in those regions. Thus contrail cirrus occurrence might be overestimated at these altitudes. The maximum around the equator between 100 hPa and 150 hPa is well reproduced and might be of importance for future simulations which consider super-sonic air traffic. Below 250 hPa the frequency of ice supersaturation maxima near the poles are largely underestimated.

The frequency of ice supersaturation has also been calculated for the EMAC-MADE3 setup, which features no saturation adjustment (not shown here). Almost all grid boxes show frequencies larger than 40 % above 300 hPa, what wouldn't be acceptable for contrail cirrus simulations. However the ice supersaturation maxima near the poles, below 300 hPa are reproduced substantially better than in both CCMod simulations.

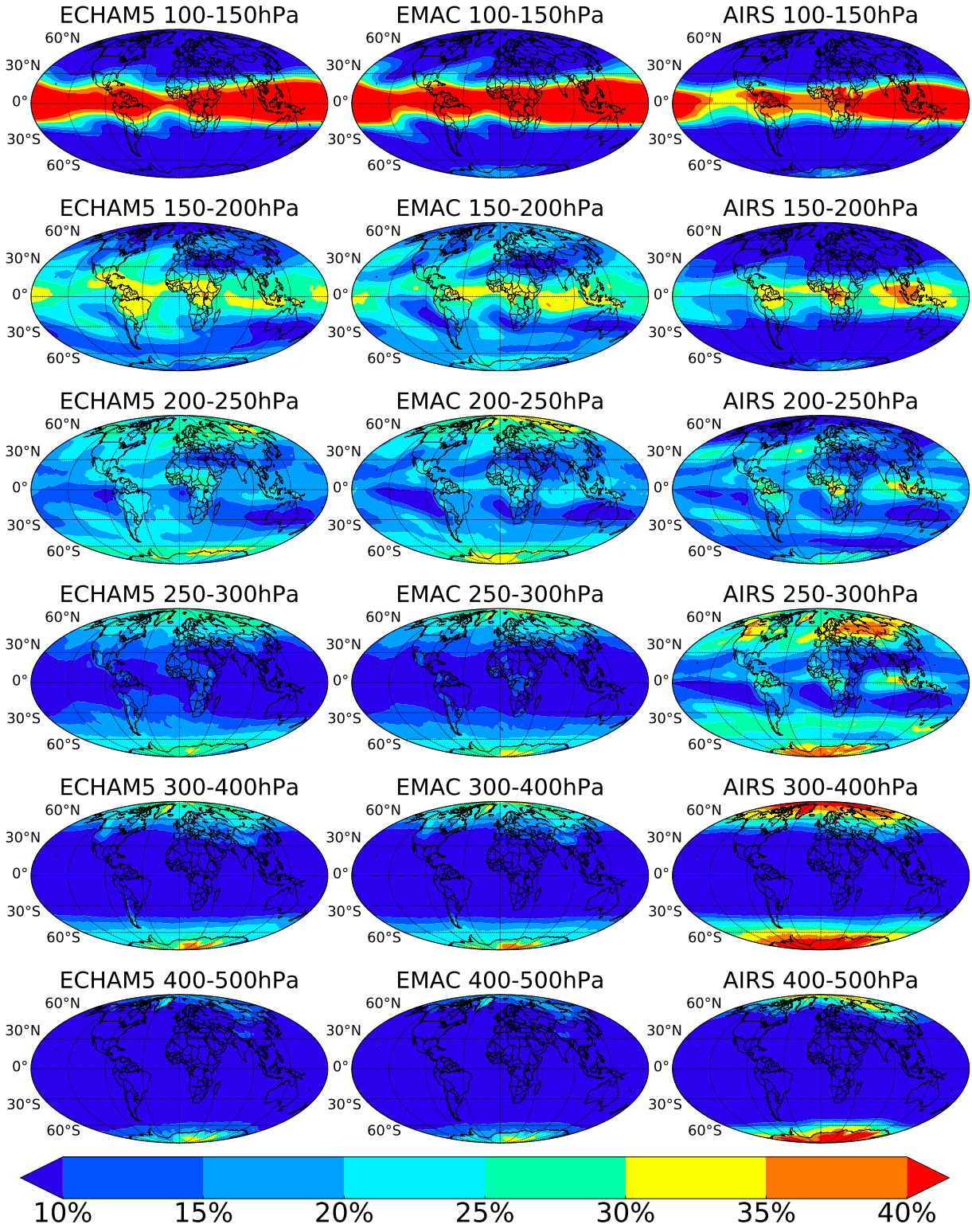

Figure A.1: Global distribution of the frequency of ice supersaturation derived by ECHAM5-CCMod and EMAC-CCMod model simulations and AIRS satellite measurements (Lamquin et al., 2012).

Appendix B

Evaluation of CO_2 radiative forcings and feedback processes against literature

In the present thesis the CO_2 simulations only serve as reference, in order to reveal the characteristics of the climate impact of contrail cirrus by comparison. For this reason, the evaluation of the CO_2 results against literature was largely assigned to this appendix. In order to ensure a fair comparison, in terms of climate sensitivity and feedback parameters, between contrail cirrus and CO_2, the CO_2 experiments presented in the main part of the present thesis were primarily based on rather small CO_2 perturbations. To allow for a better comparison with literature and to increase statistical significance, the CO_2 results discussed in this section are all based on (or scaled to) CO_2 doubling simulations. However, it is important to note that the reference CO_2 concentration used for the present thesis (348 ppmv) might differ from those used in the studies presented in the following (CO_2 reference concentrations are sometimes not explicitly provided in literature). For this reason, a CO_2 doubling might result in slightly different radiative forcings and feedbacks. Anyway, in view of the known inter-model dependency of CO_2 induced feedbacks (e. g. Bony et al., 2006), it is the qualitative agreement that matters here.

Table B.1 shows the different radiative forcings and rapid radiative adjustments (RA) derived within this study and for two multi-model studies (Vial et al., 2013; Smith et al., 2018). RF_{inst} calculated with ECHAM5-CCMod ($2.411\,Wm^{-2}$) and EMAC-CCMod ($2.919\,Wm^{-2}$) differ both noticeably because the radiation calculations of the ECHAM5-CCMod CO_2 simulations were setup after the forward approach while the EMAC-CCMod CO_2 simulations were run backwards in order to be more consistent with the contrail cirrus simulations (see Sect. 3.1.4). However, the backwards calculated RF_{inst} for CO_2 can be derived from the feedback analysis, yielding $2.589\,Wm^{-2}$ and agrees much better with the EMAC-CCMod equivalent.

Compared to the multi model mean value derived by Smith et al. (2018) ($2.61\,Wm^{-2}$) the ECHAM5-CCMod RF_{inst} estimated by feedback analysis corresponds relatively well while that derived from the EMAC-CCMod simulation is noticeably too large. Note that

Table B.1: Comparison of rapid radiative adjustments (RA) and radiative forcings (in Wm^{-2}) derived with ECHAM5-CCMod (present thesis) and EMAC-CCMod (present thesis), and after Vial et al. (2013) and Smith et al. (2018). The RAs and radiative forcings of the present thesis and of Smith et al. (2018) are based on CO_2 doubling experiments, while those of Vial et al. (2013) are based on CO_2 quadrupling simulations and therefore divided by two. The results of Vial et al. (2013) and Smith et al. (2018) are each derived from 11 different climate models. Values in brackets indicate the minimum and maximum RAs of the individual models. Note that the ECHAM5-CCMod RF_{inst} and RF_{adj} radiation calls were setup forwards (fwd) while those of EMAC-CCMod were performed backwards (bwd, a further description is provided in the text).

	ECHAM5-CCMod	EMAC-CCMod	Vial et al. (2013)[a]	Smith et al. (2018)[b]
feedback analysis method	PRP	PRP	kernel	mainly kernel
albedo RA	+0.050	+0.053	+0.09 [+0.03, +0.27]	+0.12 [0.00, +0.32]
natural cloud RA	−0.244	+0.721	+0.41 [−0.21, +0.72]	+0.43 [+0.03, +0.82]
water vapor RA	+0.336	+0.458	+0.22 [+0.14, +0.28]	+0.24 [+0.05, +0.47]
lapse-rate RA	−0.249	−0.425	−0.05 [−0.17, +0.04]	−0.58 [−0.87, −0.26]
Planck RA	−0.499	−0.502	−0.76 [−0.99, −0.58]	−0.23 [−0.38, −0.17]
strat. temp. RA	+1.568	+1.411	-	+1.12 [+0.85, +1.60]
RF_{inst}	2.411 (fwd)	2.919 (bwd)	-	2.61
RF_{adj}	4.083 (fwd)	4.177 (bwd)	-	3.73*
ERF	3.548	4.574	3.75 [3.12, 4.42]	3.70

[a] see their Table 2, divided by two due to CO_2 quadrupling simulations
[b] estimated from their Fig. 3 and Fig. S3 in the supplement
* estimated by adding the stratospheric temperature RA to RF_{inst}

it is not clear whether the multi model mean RF_{inst} of Smith et al. (2018) refers to a doubling of pre-industrial or present-day CO_2 levels (their Table S1 in their appendix even suggests a combination of both scenarios). Furthermore, it is not evident from most of the literature whether the RF_{inst} and RF_{adj} values are derived after the forward or backward approach.

Notably, the RF_{inst} derived with EMAC-CCMod after the backward approach is considerably larger than the RF_{inst} provided by Rieger et al. (2017, $2.54\,Wm^{-2}$, see their Table 2), who used the EMAC model as well, but without the extensions and modifications related to CCMod (see Sects. 3.1.2 and 3.1.3). The deviation might again be related to the direction of the radiation calculation as the EMAC-CCMod forward RF_{inst} ($2.63\,Wm^{-2}$, derived by feedback analysis) agrees much better with Rieger et al. (2017). Nevertheless, both RF_{inst} are still well within the expected range when considering the inter-model variability reported by Smith et al. (2020, compare to their Table 3). Both RF_{adj} of the present thesis are considerably overestimated, which might be mainly related to lower (pre-industrial) CO_2 concentrations chosen in Smith et al. (2018). Dietmüller (2011), who used the EMAC model as well (without CCMod), largely confirms the results derived here ($4.13\,Wm^{-2}$ for a slightly larger CO_2 increase of +368 ppmv). Note that in Smith et al. (2018) the multi-model mean ERF almost equals the RF_{adj}, which does not hold for either ECHAM5-CCMod or EMAC-CCMod. For ECHAM5-CCMod (EMAC-CCMod) the ERF is about $0.5\,Wm^{-2}$ smaller (larger) than the corresponding RF_{adj}. Those deviations are most likely

connected to differently acting natural cloud RA in both models. Especially the negative natural cloud RA in ECHAM5-CCMod somewhat deviates from multimodel behavior (Smith et al., 2018), even in sign. Nevertheless, as cloud radiative processes are subject to great uncertainties, both natural cloud RA of the models used here are not complete outliers when comparing to the individual models in Vial et al. (2013) and Chung and Soden (2015, compare to their Fig. 6a). However, the evaluated models in Smith et al. (2018) only provide positive natural cloud RA. Potential reasons for those large deviations in both CCMod models might be related to the saturation adjustment, which drastically influences the water budget in the upper troposphere (see Sect. 3.1.3). Further CO_2 simulations with deactivated saturation adjustment might help to clarify this. The remaining RAs partly deviate somewhat from the respective literature values, but are overall well within range of the individual model variabilities of Vial et al. (2013) and Smith et al. (2018).

Table B.2: Comparison of feedback parameters (FP, in $Wm^{-2}K^{-1}$) derived with EMAC-CCMod (present thesis) and with literature values from Klocke et al. (2013), Rieger et al. (2017) and Vial et al. (2013). The FPs of the present thesis and of Klocke et al. (2013) and Rieger et al. (2017) are based on CO_2 doubling experiments, while those of Vial et al. (2013) are calculated from CO_2 quadrupling simulations. The results of Vial et al. (2013) are derived from 11 different climate models. Values in brackets indicate the minimum and maximum FPs of the individual models.

	EMAC-CCMod	Klocke et al. (2013)[a]	Rieger et al. (2017)[b]	Klocke et al. (2013)[c]	Vial et al. (2013)[d]
feedback analysis method	PRP	PRP	PRP	kernel	kernel
albedo FP	+0.181	+0.19	+0.23	+0.17	+0.28 [+0.16, +0.39]
natural cloud FP	+0.765	+0.25	+0.28	+0.33	+0.27 [−0.36, +1.21]
water vapor FP	+1.757	+1.78	+2.01	+2.08	+1.68 [+1.43, +1.94]
lapse-rate FP	−0.707	−0.42	−0.85	−0.68	−0.60 [−0.97, −0.23]
Planck FP	−2.974	−3.20	−3.11	−3.08	−3.18 [−3.27, −3.10]

[a] combination of the forward and backward PRP results of their Table 1
[b] estimated from their Fig. 5
[c] kernel results of their Table 1
[d] NCAR (National Center for Atmospheric Research) kernel results of their Table 3

The origin of the restoration of radiative equilibrium can be assessed by means of the individual slow feedbacks (SF). SFs are usually normalized with the absolute surface temperature change in order to derive the feedback parameters (FP), which are best suited for a direct comparison. In this case slightly deviating CO_2 reference concentrations do not play a crucial role for FPs. Table B.2 shows the respective FPs derived from CO_2 doubling simulations within the present thesis and of three literature studies (Klocke et al., 2013; Vial et al., 2013; Rieger et al., 2017). The simulation and evaluation setup of the present thesis is closest to those of Klocke et al. (2013) and Rieger et al. (2017), as both applied the PRP feedback analysis method in combination with the ECHAM5 climate model (Rieger et al. (2017) even within the MESSy framework). Overall, the albedo, water vapor and lapse-rate FPs are well in range with the results of the other studies. The Planck FP deviates slightly from the results in literature, which are well constrained.

As already pointed out for RAs, the natural cloud FP is also characterized by large deviations between all three studies presented in Table B.2. While models with even larger

natural cloud FP are included in Vial et al. (2013), the EMAC-CCMod natural cloud FP is overestimated by a factor of three compared to Klocke et al. (2013) and Rieger et al. (2017). Again, the reintroduced saturation adjustment and the associated changes of tuning parameters (see Sect. 3.1.3 and Appendix A) might provide an explanation.

The global mean surface temperature increase of +5.013 K, due to a CO_2 doubling, calculated with EMAC-CCMod, turns out to be significantly larger than that of Dietmüller (2011, +2.81 K, see Table 8.1 therein) and Rieger et al. (2017, +2.79 K, estimated from their Table 2). A considerably lower global mean surface temperature increase of +3.37 K, based on 15 different climate models, was also derived by Andrews et al. (2012) (compare to their Table 1) and is partly a consequence of the comparatively high natural cloud FP. Nevertheless, due to the overall larger ERF yielded in EMAC-CCMod, the resulting climate sensitivity parameter (1.096 $KW^{-1}m^2$) is not far off from that derived by Andrews et al. (2012, 0.93 $KW^{-1}m^2$, estimated from their Table 1).

In summary it can be stated that the CO_2 doubling simulations carried out with the EMAC-CCMod setup perform sufficiently well to serve as a sensible reference in the framework of this study. RA and FP mostly agree well with results of other studies. However, radiative effects concerning natural clouds display certain deviations from multimodel means in literature. Further research is needed to isolate the origin of these deviations, which might be connected to the reintroduction of the saturation adjustment. Nevertheless, as contrail cirrus and CO_2 simulations were performed with the same model setup, these deviations are working in the same direction and so will cancel out when the contrail cirrus response is evaluated relative to the CO_2 reference response.

Appendix C

Origin of strong variations between forward and backward PRP calculations

The PRP feedback analysis method (a detailed description can be found in Sect. 3.2.1) combines a forward and a backward calculation of perturbation induced radiative flux changes to derive rapid radiative adjustments (RA) and slow feedbacks (SF). However, large deviations between the forward and backward PRP calculations were found for the cloud, water vapor and lapse-rate RA in Bickel et al. (2020, see their Fig. A1). This phenomenon has already been pointed out by Rieger et al. (2017, see their Fig. 4). The radiative budget regarding the feedbacks is only balanced if forward and backward PRP calculations were combined. This so called centered version of the PRP feedback analysis was for this reason strongly recommended to be used by Rieger et al. (2017). In contrast to that, results derived with the kernel method are mostly calculated in a way that corresponds to the forward calculation of the PRP method (see also Sect. 3.2.1). For this reason, the feedbacks derived with the PRP method might sometimes differ from those calculated with the kernel method. To investigate the issue, Bickel et al. (2020) have suggested to test the forward/backward approach for the kernel method as well. Motivated by this, Martin (2021) calculated backward kernels for SF (except for clouds) and partly disproved the hypothesis mentioned above. Forward and backward calculations were found to be very similar for the albedo, lapse-rate and water vapor SF, while a relatively large deviation of $0.49\,\mathrm{Wm^{-2}K^{-1}}$ was obtained for the Planck SF (Martin, 2021).

Fig. A1 of Bickel et al. (2020) already revealed that, almost exclusively, the LW parts of the natural cloud, water vapor and lapse-rate RA are affected by strong deviations between forward and backward calculations (based on ECHAM5 simulations). Further tests with the PRP feedback tool clearly showed that those deviations are linked to clouds. If clouds are removed from feedback calculations (cloud cover, IWC and ICNC set to zero), the deviations between forward and backward calculations are strongly reduced. Fig. C.1 shows the PRP feedback analysis results of the ECHAM5-CCMod CO_2-2× simulation, subdivided into clear-sky and cloudy-sky parts. The strongest deviations between forward

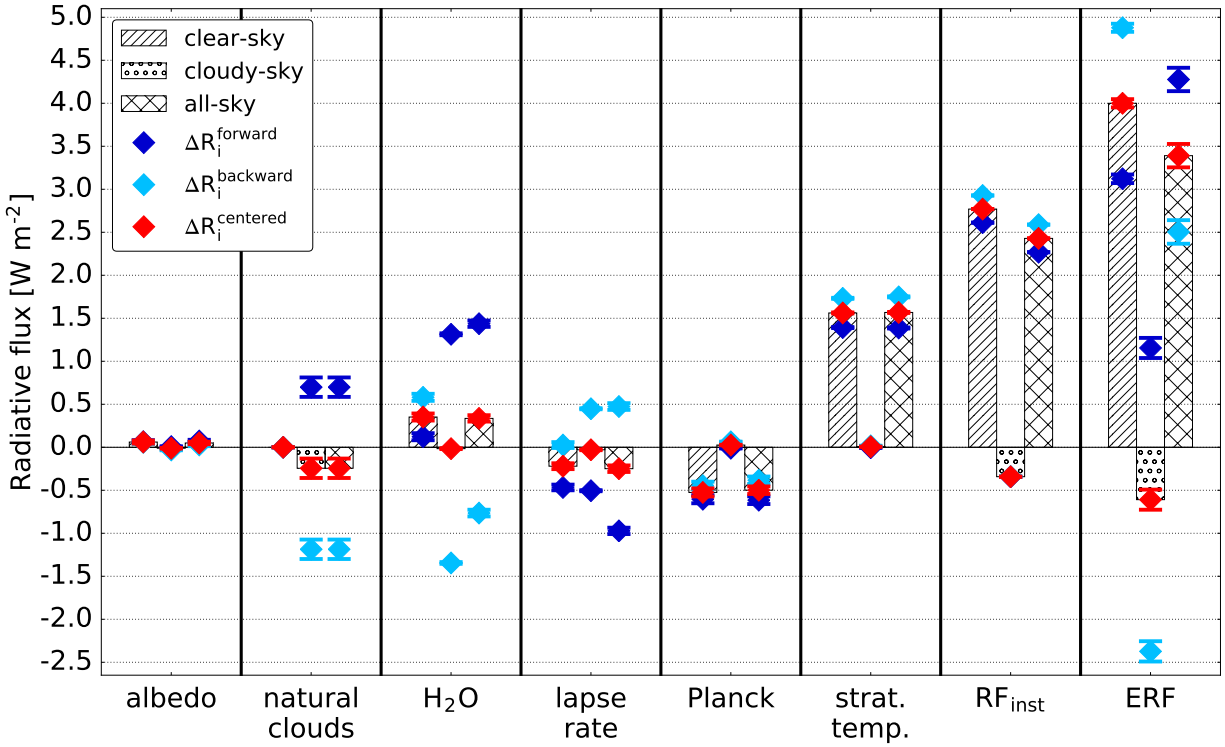

Figure C.1: Results of the PRP feedback analysis for rapid radiative adjustments (RA) based on the CO_2-2× ECHAM5-CCMod FSST simulation. Radiative fluxes are subdivided into clear-sky (striped infill), cloudy-sky (dotted infill) and all-sky (crossed infill) parts. Furthermore, the associated radiative fluxes of the forward (dark blue), backward (light blue) and centered (red) calculation are shown. Whiskers show the 95 % confidence intervals based on the interannual variabilities. Natural cloud, water vapor and lapse-rate RA are characterized by strong variations in their cloudy-sky fluxes for the respective forward and backward calculation, even in sign.

and backward calculations can be traced back to the cloudy sky parts of the natural cloud, water vapor and lapse-rate RA. However, only the natural cloud RA is driven by the cloudy-sky part, while the water vapor and lapse-rate RAs yield a net cloudy-sky part of approximately zero. Thus the impact of clouds can be unambiguously identified as the source for the considerably strong deviations between forward and backward calculations of the PRP feedback analysis.

Physically, the origin of these deviations is rooted in the principal setup of the radiation calls of the PRP feedback analysis method. RAs and SFs are determined by exchanging the variables of the underlying feedbacks in the respective radiation calls. However, the impact of clouds is not only reflected in cloud cover, IWC and ICNC, but also indirectly included in the temperature and therefore in the water vapor profile. E. g. contrail cirrus and natural cirrus warm the atmosphere below, while deep stratiform clouds cool the layers beneath. Thus the footprint of clouds is more or less contained in all PRP feedback variables to be

exchanged. If calculating the individual feedbacks the primary cloud impact (cloud cover, IWC and ICNC changes) is separated from follow-up effects (temperature and water vapor changes induced by clouds), which leads to non-linearities in the radiation calculations and thus to deviations between forward and backward calculations. In a similar way those deviations find their way into the clear-sky parts (see Fig. C.1). The model itself does not differentiate between clear-sky and cloudy-sky temperature and water vapor profiles. For this reason the effect of clouds is indirectly included in the clear-sky fluxes of the lapse-rate and water vapor feedback as well and leads to the corresponding deviations between forward and backward calculations.

Nevertheless, if combining forward and backward calculations those deviations cancel out each other relatively well due to their contrary construction. When this principle is taken into account RAs and SFs can be determined reasonably well, as shown in Appendix B. This again demonstrates that the combination of forward and backward calculations is essential when applying the PRP feedback analysis method.

Acronyms

AEDT	Aviation Environmental Design Tool
AIRS	Atmospheric InfraRed Sounder (on board the NASA Aqua satellite)
ATR	acronym used for air traffic induced contrail cirrus simulations
CCMod	contrail cirrus parameterization developed by Bock (2014)
CDNC	cloud droplet number concentration
CH_4	methane
CO_2	carbon dioxide
CRE	cloud radiative effect
ECHAM5	5^{th} generation of the ECMWF model, Hamburg version
EMAC	ECHAM/MESSy Atmospheric Chemistry model
ERF	effective radiative forcing
ERF_{FSST}	effective radiative forcing based on fixed sea surface temperature simulations
FP	feedback parameter
FSST	fixed sea surface temperature
GCM	general circulation model
ICNC	ice crystal number concentration
IPCC	Intergovernmental Panel on Climate Change
IWC	ice water content
IWP	ice water path (cloud ice water)
K14	cloud scheme after Kuebbeler et al. (2014)
LF10	cloud scheme after Lohmann and Ferrachat (2010)
LW	longwave
LWCRE	long wave cloud radiative effect
LWP	liquid water path (cloud liquid water)
MADE3	Modal Aerosol Dynamics model for Europe, adapted for global applications, third generation developed by Kaiser et al. (2019)

MESSy	Modular Earth Submodel System
MLO	mixed-layer ocean
NO_x	nitrogen oxides
O_3	ozone
OLR	outgoing longwave radiation
ppmv	parts per million volume
PRP	partial radiative perturbation method
RA	rapid radiative adjustment
RF	radiative forcing
RF_{adj}	stratosphere adjusted radiative forcing
RF_{inst}	instantaneous radiative forcing
SF	slow feedback
SST	sea surface temperature
SW	shortwave
SWCRE	short wave cloud radiative effect
TOA	top of atmosphere
WMO	World Meteorological Organization
WVM	water vapor mixing ratio

Variables

$\mathbf{r}$	climate efficacy parameter
$\mathbf{r}_{\text{eff}}$	effective radius of particles
$\Delta \text{T}_{\text{surface}}$	surface temperature change
α	feedback parameter
λ	climate sensitivity parameter
λ_{CO_2}	climate sensitivity parameter of carbon dioxide

List of Figures

List of Tables

Bibliography

Ackerman, T. P., K.-N. Liou, F. P. J. Valero, and L. Pfister, 1988: Heating Rates in Tropical Anvils. *Journal of the Atmospheric Sciences*, 45 (10), 1606–1623, https://doi.org/10.1175/1520-0469(1988)045⟨1606:HRITA⟩2.0.CO;2.

Adler, R. F., G. Gu, and G. J. Huffman, 2012: Estimating Climatological Bias Errors for the Global Precipitation Climatology Project (GPCP). *Journal of Applied Meteorology and Climatology*, 51 (1), 84 – 99, https://doi.org/10.1175/JAMC-D-11-052.1.

Adler, R. F., M. R. P. Sapiano, G. J. Huffman, J.-J. Wang, G. Gu, D. Bolvin, L. Chiu, U. Schneider, A. Becker, E. Nelkin, P. Xie, R. Ferraro, and D.-B. Shin, 2018: The Global Precipitation Climatology Project (GPCP) Monthly Analysis (New Version 2.3) and a Review of 2017 Global Precipitation. *Atmosphere*, 9 (4), https://doi.org/10.3390/atmos9040138.

Airlines for America, 2021: World Airlines Traffic and Capacity. https://www.airlines.org/dataset/world-airlines-traffic-and-capacity-2/, accessed: 2021-11-10.

Alfaro-Contreras, R., J. Zhang, J. S. Reid, and S. Christopher, 2017: A study of 15-year aerosol optical thickness and direct shortwave aerosol radiative effect trends using MODIS, MISR, CALIOP and CERES. *Atmospheric Chemistry and Physics*, 17 (22), 13 849–13 868, https://doi.org/10.5194/acp-17-13849-2017.

Allan, R. P., 2011: Combining satellite data and models to estimate cloud radiative effect at the surface and in the atmosphere. *Meteorological Applications*, 18 (3), 324–333, https://doi.org/10.1002/met.285.

Allen, M., and W. Ingram, 2002: Constraints on Future Changes in Climate and the Hydrologic Cycle. *Nature*, 419, 224–32, https://doi.org/10.1038/nature01092.

Andrews, T., J. M. Gregory, M. J. Webb, and K. E. Taylor, 2012: Forcing, feedbacks and climate sensitivity in CMIP5 coupled atmosphere-ocean climate models. *Geophysical Research Letters*, 39 (9), https://doi.org/10.1029/2012GL051607.

Appleman, H., 1953: The Formation of Exhaust Condensation Trails by Jet Aircraft. *Bulletin of the American Meteorological Society*, 34 (1), 14 – 20, https://doi.org/10.1175/1520-0477-34.1.14.

Berntsen, T. K., J. S. Fuglestvedt, M. M. Joshi, K. P. Shine, N. Stuber, M. Ponater, R. Sausen, D. A. Hauglustaine, and L. Li, 2005: Response of climate to regional emissions of ozone precursors: sensitivities and warming potentials. *Tellus, Series B: Chemical and Physical Meteorology*, 57, 283–304, https://doi.org/10.1111/j.1600-0889.2005.00152.x.

Bickel, M., M. Ponater, L. Bock, U. Burkhardt, and S. Reineke, 2020: Estimating the Effective Radiative Forcing of Contrail Cirrus. *Journal of Climate*, 33 (5), 1991 – 2005, https://doi.org/10.1175/JCLI-D-19-0467.1.

Bier, A., and U. Burkhardt, 2019: Variability in Contrail Ice Nucleation and Its Dependence on Soot Number Emissions. *Journal of Geophysical Research: Atmospheres*, 124 (6), 3384–3400, https://doi.org/10.1029/2018JD029155.

Bock, L., 2014: Modellierung von Kondensstreifenzirren. Ph.D. thesis, Ludwig-Maximilians-Universität München, https://doi.org/10.5282/edoc.17026.

Bock, L., and U. Burkhardt, 2016a: The temporal evolution of a long-lived contrail cirrus cluster: Simulations with a global climate model. *Journal of Geophysical Research: Atmospheres*, 121 (7), 3548–3565, https://doi.org/10.1002/2015JD024475.

Bock, L., and U. Burkhardt, 2016b: Reassessing properties and radiative forcing of contrail cirrus using a climate model. *Journal of Geophysical Research: Atmospheres*, 121 (16), 9717–9736, https://doi.org/10.1002/2016JD025112.

Bock, L., and U. Burkhardt, 2019: Contrail cirrus radiative forcing for future air traffic. *Atmospheric Chemistry and Physics*, 19 (12), 8163–8174, https://doi.org/10.5194/acp-19-8163-2019.

Boer, G., and B. Yu, 2003a: Climate sensitivity and response. *Climate Dynamics*, 20 (4), 415–429, https://doi.org/10.1007/s00382-002-0283-3.

Boer, G. J., and B. Yu, 2003b: Climate sensitivity and climate state. *Climate Dynamics*, 21 (2), 167–176, https://doi.org/10.1007/s00382-003-0323-7.

Boltzmann, L., 1884: Ableitung des Stefan'schen Gesetzes, betreffend die Abhängigkeit der Wärmestrahlung von der Temperatur aus der electromagnetischen Lichttheorie. *Annalen der Physik*, 258 (6), 291–294, https://doi.org/10.1002/andp.18842580616.

Bony, S., R. Colman, V. M. Kattsov, R. P. Allan, C. S. Bretherton, J.-L. Dufresne, A. Hall, S. Hallegatte, M. M. Holland, W. Ingram, D. A. Randall, B. J. Soden, G. Tselioudis, and M. J. Webb, 2006: How Well Do We Understand and Evaluate Climate Change Feedback Processes? *Journal of Climate*, 19 (15), 3445 – 3482, https://doi.org/10.1175/JCLI3819.1.

Burkhardt, U., and B. Kärcher, 2009: Process-based simulation of contrail cirrus in a global climate model. *Journal of Geophysical Research: Atmospheres*, 114 (D16), https://doi.org/10.1029/2008JD011491.

Burkhardt, U., and B. Kärcher, 2011: Global radiative forcing from contrail cirrus. *Nature Climate Change*, 1 (1), 54–58, https://doi.org/10.1038/nclimate1068.

Burkhardt, U., B. Kärcher, M. Ponater, K. Gierens, and A. Gettelman, 2008: Contrail cirrus supporting areas in model and observations. *Geophysical Research Letters*, 35 (16), https://doi.org/10.1029/2008GL034056.

Burkhardt, U., B. Kärcher, and U. Schumann, 2010: Global Modeling of the Contrail and Contrail Cirrus Climate Impact. *Bulletin of the American Meteorological Society*, 91 (4), 479 – 484, https://doi.org/10.1175/2009BAMS2656.1.

Cess, R. D., 1975: Global climate change: an investigation of atmospheric feedback mechanisms. *Tellus*, 27 (3), 193–198, https://doi.org/10.1111/j.2153-3490.1975.tb01672.x.

Chen, C.-C., and A. Gettelman, 2013: Simulated radiative forcing from contrails and contrail cirrus. *Atmospheric Chemistry and Physics*, 13 (24), 12 525–12 536, https://doi.org/10.5194/acp-13-12525-2013.

Chen, C.-C., and A. Gettelman, 2016: Simulated 2050 aviation radiative forcing from contrails and aerosols. *Atmospheric Chemistry and Physics*, 16 (11), 7317–7333, https://doi.org/10.5194/acp-16-7317-2016.

Chung, E.-S., and B. J. Soden, 2015: An Assessment of Direct Radiative Forcing, Radiative Adjustments, and Radiative Feedbacks in Coupled Ocean-Atmosphere Models. *Journal of Climate*, 28 (10), 4152–4170, https://doi.org/10.1175/JCLI-D-14-00436.1.

Colman, R. A., and B. J. McAvaney, 1997: A study of general circulation model climate feedbacks determined from perturbed sea surface temperature experiments. *Journal of Geophysical Research: Atmospheres*, 102 (D16), 19 383–19 402, https://doi.org/10.1029/97JD00206.

Colman, R. A., and B. J. Soden, 2021: Water vapor and lapse rate feedbacks in the climate system. *Rev. Mod. Phys.*, 93, 045 002, https://doi.org/10.1103/RevModPhys.93.045002.

Deuber, O., S. Matthes, R. Sausen, M. Ponater, and L. Lim, 2013: A physical metric-based framework for evaluating the climate trade-off between CO2 and contrails – The case of lowering aircraft flight trajectories. *Environmental Science & Policy*, 25, 176–185, https://doi.org/10.1016/j.envsci.2012.10.004.

Díaz-Francés, E., and F. J. Rubio, 2013: On the existence of a normal approximation to the distribution of the ratio of two independent normal random variables. *Statistical Papers*, 54 (2), 309–323, https://doi.org/10.1007/s00362-012-0429-2.

Dietmüller, S., 2011: Relative Bedeutung chemischer und physikalischer Rückkopplungen in Klimasensitivitätsstudien mit dem Klima-Chemie-Modellsystem EMAC/MLO. Ph.D. thesis, Ludwig-Maximilians-Universität München, https://doi.org/10.5282/edoc.13680.

Dietmüller, S., M. Ponater, and R. Sausen, 2014: Interactive ozone induces a negative feedback in CO2-driven climate change simulations. *Journal of Geophysical Research: Atmospheres*, 119 (4), 1796–1805, https://doi.org/10.1002/2013JD020575.

Dietmüller, S., P. Jöckel, H. Tost, M. Kunze, C. Gellhorn, S. Brinkop, C. Frömming, M. Ponater, B. Steil, A. Lauer, and J. Hendricks, 2016: A new radiation infrastructure for the Modular Earth Submodel System (MESSy, based on version 2.51). *Geoscientific Model Development*, 9 (6), 2209–2222, https://doi.org/10.5194/gmd-9-2209-2016.

Duda, D. P., P. Minnis, K. Khlopenkov, T. L. Chee, and R. Boeke, 2013: Estimation of 2006 Northern Hemisphere contrail coverage using MODIS data. *Geophysical Research Letters*, 40 (3), 612–617, https://doi.org/10.1002/grl.50097.

Elsaesser, G. S., C. W. O'Dell, M. D. Lebsock, R. Bennartz, T. J. Greenwald, and F. J. Wentz, 2017: The Multisensor Advanced Climatology of Liquid Water Path (MAC-LWP). *Journal of Climate*, 30 (24), 10 193 – 10 210, https://doi.org/10.1175/JCLI-D-16-0902.1.

Feichter, J., and U. Lohmann, 1999: Can a relaxation technique be used to validate clouds and sulphur species in a GCM? *Quarterly Journal of the Royal Meteorological Society*, 125 (556), 1277–1294, https://doi.org/10.1002/qj.1999.49712555609.

Fieller, E. C., 1954: Some Problems in Interval Estimation. *Journal of the Royal Statistical Society: Series B (Methodological)*, 16 (2), 175–185, https://doi.org/10.1111/j.2517-6161.1954.tb00159.x.

Flamant, C., P. Knippertz, A. H. Fink, A. Akpo, B. Brooks, C. J. Chiu, H. Coe, S. Danuor, M. Evans, O. Jegede, N. Kalthoff, A. Konaré, C. Liousse, F. Lohou, C. Mari, H. Schlager, A. Schwarzenboeck, B. Adler, L. Amekudzi, J. Aryee, M. Ayoola, A. M. Batenburg, G. Bessardon, S. Borrmann, J. Brito, K. Bower, F. Burnet, V. Catoire, A. Colomb, C. Denjean, K. Fosu-Amankwah, P. G. Hill, J. Lee, M. Lothon, M. Maranan, J. Marsham, R. Meynadier, J.-B. Ngamini, P. Rosenberg, D. Sauer, V. Smith, G. Stratmann, J. W. Taylor, C. Voigt, and V. Yoboué, 2018: The Dynamics-Aerosol-Chemistry-Cloud Interactions in West Africa Field Campaign: Overview and Research Highlights. *Bulletin of the American Meteorological Society*, 99 (1), 83 – 104, https://doi.org/10.1175/BAMS-D-16-0256.1.

Forster, L., C. Emde, B. Mayer, and S. Unterstrasser, 2012: Effects of Three-Dimensional Photon Transport on the Radiative Forcing of Realistic Contrails. *Journal of the Atmospheric Sciences*, 69 (7), 2243 – 2255, https://doi.org/10.1175/JAS-D-11-0206.1.

Forster, P. M., T. Richardson, A. C. Maycock, C. J. Smith, B. H. Samset, G. Myhre, T. Andrews, R. Pincus, and M. Schulz, 2016: Recommendations for diagnosing effective radiative forcing from climate models for CMIP6. *Journal of Geophysical Research: Atmospheres*, 121 (20), 12,460–12,475, https://doi.org/10.1002/2016JD025320.

Frömming, C., M. Ponater, K. Dahlmann, V. Grewe, D. S. Lee, and R. Sausen, 2012: Aviation-induced radiative forcing and surface temperature change in dependency of the emission altitude. *Journal of Geophysical Research: Atmospheres*, 117 (D19), https://doi.org/10.1029/2012JD018204.

Fuglestvedt, J., T. Berntsen, O. Godal, R. Sausen, K. Shine, and T. Skodvin, 2003: Metrics of Climate Change: Assessing Radiative Forcing and Emission Indices. *Climatic Change*, 58, 267–331, https://doi.org/10.1023/A:1023905326842.

Fuglestvedt, J., T. Berntsen, G. Myhre, K. Rypdal, and R. B. Skeie, 2008: Climate forcing from the transport sectors. *Proceedings of the National Academy of Sciences*, 105 (2), 454–458, https://doi.org/10.1073/pnas.0702958104.

Fuglestvedt, J., K. Shine, T. Berntsen, J. Cook, D. Lee, A. Stenke, R. Skeie, G. Velders, and I. Waitz, 2010: Transport impacts on atmosphere and climate: Metrics. *Atmospheric Environment*, 44 (37), 4648–4677, https://doi.org/10.1016/j.atmosenv.2009.04.044.

Gettelman, A., and C. Chen, 2013: The climate impact of aviation aerosols. *Geophysical Research Letters*, 40 (11), 2785–2789, https://doi.org/10.1002/grl.50520.

Graf, K., U. Schumann, H. Mannstein, and B. Mayer, 2012: Aviation induced diurnal North Atlantic cirrus cover cycle. *Geophysical Research Letters*, 39 (16), https://doi.org/10.1029/2012GL052590.

Gregory, J. M., and T. Andrews, 2016: Variation in climate sensitivity and feedback parameters during the historical period. *Geophysical Research Letters*, 43 (8), 3911–3920, https://doi.org/10.1002/2016GL068406.

Gregory, J. M., W. J. Ingram, M. A. Palmer, G. S. Jones, P. A. Stott, R. B. Thorpe, J. A. Lowe, T. C. Johns, and K. D. Williams, 2004: A new method for diagnosing radiative forcing and climate sensitivity. *Geophysical Research Letters*, 31 (3), https://doi.org/10.1029/2003GL018747.

Grewe, V., K. Dahlmann, J. Flink, C. Frömming, R. Ghosh, K. Gierens, R. Heller, J. Hendricks, P. Jöckel, S. Kaufmann, K. Kölker, F. Linke, T. Luchkova, B. Lührs, J. Van Manen, S. Matthes, A. Minikin, M. Niklaß, M. Plohr, M. Righi, S. Rosanka, A. Schmitt, U. Schumann, I. Terekhov, S. Unterstrasser, M. Vázquez-Navarro, C. Voigt, K. Wicke, H. Yamashita, A. Zahn, and H. Ziereis, 2017: Mitigating the Climate Impact from Aviation: Achievements and Results of the DLR WeCare Project. *Aerospace*, 4 (3), https://doi.org/10.3390/aerospace4030034.

Gruber, S., S. Unterstrasser, J. Bechtold, H. Vogel, M. Jung, H. Pak, and B. Vogel, 2018: Contrails and their impact on shortwave radiation and photovoltaic power production – a regional model study. *Atmospheric Chemistry and Physics*, 18 (9), 6393–6411, https://doi.org/10.5194/acp-18-6393-2018.

Hansen, J., M. Sato, and R. Ruedy, 1997: Radiative forcing and climate response. *Journal of Geophysical Research: Atmospheres*, 102 (D6), 6831–6864, https://doi.org/10.1029/96JD03436.

Hansen, J., M. Sato, L. Nazarenko, R. Ruedy, A. Lacis, D. Koch, I. Tegen, T. Hall, D. Shindell, B. Santer, P. Stone, T. Novakov, L. Thomason, R. Wang, Y. Wang, D. Jacob, S. Hollandsworth, L. Bishop, J. Logan, A. Thompson, R. Stolarski, J. Lean, R. Willson, S. Levitus, J. Antonov, N. Rayner, D. Parker, and J. Christy, 2002: Climate forcings in Goddard Institute for Space Studies SI2000 simulations. *Journal of Geophysical Research: Atmospheres*, 107 (D18), ACL 2–1–ACL 2–37, https://doi.org/10.1029/2001JD001143.

Hansen, J., M. Sato, R. Ruedy, L. Nazarenko, A. Lacis, G. A. Schmidt, G. Russell, I. Aleinov, M. Bauer, S. Bauer, N. Bell, B. Cairns, V. Canuto, M. Chandler, Y. Cheng, A. Del Genio, G. Faluvegi, E. Fleming, A. Friend, T. Hall, C. Jackman, M. Kelley, N. Kiang, D. Koch, J. Lean, J. Lerner, K. Lo, S. Menon, R. Miller, P. Minnis, T. Novakov, V. Oinas, J. Perlwitz, J. Perlwitz, D. Rind, A. Romanou, D. Shindell, P. Stone, S. Sun, N. Tausnev, D. Thresher, B. Wielicki, T. Wong, M. Yao, and S. Zhang, 2005: Efficacy of climate forcings. *Journal of Geophysical Research: Atmospheres*, 110 (D18), https://doi.org/10.1029/2005JD005776.

Hartmann, D., A. Klein Tank, M. Rusticucci, L. Alexander, S. Brönnimann, Y. Charabi, F. Dentener, E. Dlugokencky, D. Easterling, A. Kaplan, B. Soden, P. Thorne, M. Wild, and P. Zhai, 2013: *Observations: Atmosphere and Surface*, book section 2, 159–254. Cambridge University Press, Cambridge, United Kingdom and New York, NY, USA, https://doi.org/10.1017/CBO9781107415324.008.

Haywood, J. M., R. P. Allan, J. Bornemann, P. M. Forster, P. N. Francis, S. Milton, G. Rädel, A. Rap, K. P. Shine, and R. Thorpe, 2009: A case study of the radiative forcing of persistent contrails evolving into contrail-induced cirrus. *Journal of Geophysical Research: Atmospheres*, 114 (D24), https://doi.org/10.1029/2009JD012650.

He, J., T. Glotfelty, K. Yahya, K. Alapaty, and S. Yu, 2017: Does temperature nudging overwhelm aerosol radiative effects in regional integrated climate models? *Atmospheric Environment*, 154, 42–52, https://doi.org/10.1016/j.atmosenv.2017.01.040.

Heymsfield, A. J., R. P. Lawson, and G. W. Sachse, 1998: Growth of ice crystals in a precipitating contrail. *Geophysical Research Letters*, 25 (9), 1335–1338, https://doi.org/10.1029/98GL00189.

Hulley, G. C., S. J. Hook, E. Abbott, N. Malakar, T. Islam, and M. Abrams, 2015: The ASTER Global Emissivity Dataset (ASTER GED): Mapping Earth's emissivity at 100 meter spatial scale. *Geophysical Research Letters*, 42 (19), 7966–7976, https://doi.org/10.1002/2015GL065564.

ICAO, 1995–2021: Annual Reports of the Council of the International Civil Aviation Organization. International Civil Aviation Organization, https://www.icao.int/about-icao/Pages/annual-reports.aspx, accessed: 2023-03-03.

IPCC, 2013: *Climate Change 2013: The Physical Science Basis. Contribution of Working Group I to the Fifth Assessment Report of the Intergovernmental Panel on Climate Change*. Cambridge University Press, Cambridge, United Kingdom and New York, NY, USA, 1535 pp., https://doi.org/10.1017/CBO9781107415324.

Irvine, E. A., B. J. Hoskins, and K. P. Shine, 2014: A simple framework for assessing the trade-off between the climate impact of aviation carbon dioxide emissions and contrails for a single flight. *Environmental Research Letters*, 9 (6), 064 021, https://doi.org/10.1088/1748-9326/9/6/064021.

Jaramillo, P., S. Kahn Ribeiro, P. Newman, S. Dhar, O. Diemuodeke, T. Kajino, D. Lee, S. Nugroho, X. Ou, A. Hammer Strømman, and J. Whitehead, 2022: *Transport*, book section 10. Cambridge University Press, https://doi.org/10.1017/9781009157926.012.

Jöckel, P., H. Tost, A. Pozzer, C. Brühl, J. Buchholz, L. Ganzeveld, P. Hoor, A. Kerkweg, M. G. Lawrence, R. Sander, B. Steil, G. Stiller, M. Tanarhte, D. Taraborrelli, J. van Aardenne, and J. Lelieveld, 2006: The atmospheric chemistry general circulation model ECHAM5/MESSy1: consistent simulation of ozone from the surface to the mesosphere. *Atmospheric Chemistry and Physics*, 6 (12), 5067–5104, https://doi.org/10.5194/acp-6-5067-2006.

Jöckel, P., A. Kerkweg, A. Pozzer, R. Sander, H. Tost, H. Riede, A. Baumgaertner, S. Gromov, and B. Kern, 2010: Development cycle 2 of the Modular Earth Submodel System (MESSy2). *Geoscientific Model Development*, 3 (2), 717–752, https://doi.org/10.5194/gmd-3-717-2010.

Jöckel, P., H. Tost, A. Pozzer, M. Kunze, O. Kirner, C. A. M. Brenninkmeijer, S. Brinkop, D. S. Cai, C. Dyroff, J. Eckstein, F. Frank, H. Garny, K.-D. Gottschaldt, P. Graf, V. Grewe, A. Kerkweg, B. Kern, S. Matthes, M. Mertens, S. Meul, M. Neumaier, M. Nützel, S. Oberländer-Hayn, R. Ruhnke, T. Runde, R. Sander, D. Scharffe, and A. Zahn, 2016: Earth System Chemistry integrated Modelling (ESCiMo) with the Modular Earth Submodel System (MESSy) version 2.51. *Geoscientific Model Development*, 9 (3), 1153–1200, https://doi.org/10.5194/gmd-9-1153-2016.

Jonko, A. K., K. M. Shell, B. M. Sanderson, and G. Danabasoglu, 2012: Climate Feedbacks in CCSM3 under Changing CO2 Forcing. Part I: Adapting the Linear Radiative Kernel Technique to Feedback Calculations for a Broad Range of Forcings. *Journal of Climate*, 25 (15), 5260 – 5272, https://doi.org/10.1175/JCLI-D-11-00524.1.

Joshi, M., K. Shine, M. Ponater, N. Stuber, R. Sausen, and L. Li, 2003: A comparison of climate response to different radiative forcings in three general circulation models:

towards an improved metric of climate change. *Climate Dynamics*, 20 (7), 843–854, https://doi.org/10.1007/s00382-003-0305-9.

Kaiser, J. C., J. Hendricks, M. Righi, P. Jöckel, H. Tost, K. Kandler, B. Weinzierl, D. Sauer, K. Heimerl, J. P. Schwarz, A. E. Perring, and T. Popp, 2019: Global aerosol modeling with MADE3 (v3.0) in EMAC (based on v2.53): model description and evaluation. *Geoscientific Model Development*, 12 (1), 541–579, https://doi.org/10.5194/gmd-12-541-2019.

Kärcher, B., 2017: Cirrus Clouds and Their Response to Anthropogenic Activities. *Current Climate Change Reports*, 3 (1), 45–57, https://doi.org/10.1007/s40641-017-0060-3.

Kärcher, B., 2018: Formation and Radiative Forcing of Contrail Cirrus. *Nature Communications*, 9, https://doi.org/10.1038/s41467-018-04068-0.

Kärcher, B., J. Hendricks, and U. Lohmann, 2006: Physically based parameterization of cirrus cloud formation for use in global atmospheric models. *Journal of Geophysical Research: Atmospheres*, 111 (D1), https://doi.org/10.1029/2005JD006219.

Karydis, V. A., P. Kumar, D. Barahona, I. N. Sokolik, and A. Nenes, 2011: On the effect of dust particles on global cloud condensation nuclei and cloud droplet number. *Journal of Geophysical Research: Atmospheres*, 116 (D23), https://doi.org/10.1029/2011JD016283.

Karydis, V. A., A. P. Tsimpidi, S. Bacer, A. Pozzer, A. Nenes, and J. Lelieveld, 2017: Global impact of mineral dust on cloud droplet number concentration. *Atmospheric Chemistry and Physics*, 17 (9), 5601–5621, https://doi.org/10.5194/acp-17-5601-2017.

King, M. D., S. Platnick, W. P. Menzel, S. A. Ackerman, and P. A. Hubanks, 2013: Spatial and temporal distribution of clouds observed by modis onboard the terra and aqua satellites. *IEEE Transactions on Geoscience and Remote Sensing*, 51 (7), 3826–3852, https://doi.org/10.1109/TGRS.2012.2227333.

Klocke, D., J. Quaas, and B. Stevens, 2013: Assessment of different metrics for physical climate feedbacks. *Climate Dynamics*, 41 (5), 1173–1185, https://doi.org/10.1007/s00382-013-1757-1.

Klöwer, M., M. R. Allen, D. S. Lee, S. R. Proud, L. Gallagher, and A. Skowron, 2021: Quantifying aviation's contribution to global warming. *Environmental Research Letters*, 16 (10), 104 027, https://doi.org/10.1088/1748-9326/ac286e.

Koop, T., B. Luo, A. Tsias, and T. Peter, 2000: Water Activity as the determinant for homogeneous ice nucleation in aqueous solutions. *Nature*, 406, 611–4, https://doi.org/10.1038/35020537.

Kopp, G., and J. L. Lean, 2011: A new, lower value of total solar irradiance: Evidence and climate significance. *Geophysical Research Letters*, 38 (1), https://doi.org/10.1029/2010GL045777.

Krämer, M., C. Schiller, A. Afchine, R. Bauer, I. Gensch, A. Mangold, S. Schlicht, N. Spelten, N. Sitnikov, S. Borrmann, M. de Reus, and P. Spichtinger, 2009: Ice supersaturations and cirrus cloud crystal numbers. *Atmospheric Chemistry and Physics*, 9 (11), 3505–3522, https://doi.org/10.5194/acp-9-3505-2009.

Krämer, M., C. Rolf, A. Luebke, A. Afchine, N. Spelten, A. Costa, J. Meyer, M. Zöger, J. Smith, R. L. Herman, B. Buchholz, V. Ebert, D. Baumgardner, S. Borrmann, M. Klingebiel, and L. Avallone, 2016: A microphysics guide to cirrus clouds – Part 1: Cirrus types. *Atmospheric Chemistry and Physics*, 16 (5), 3463–3483, https://doi.org/10.5194/acp-16-3463-2016.

Krämer, M., C. Rolf, N. Spelten, A. Afchine, D. Fahey, E. Jensen, S. Khaykin, T. Kuhn, P. Lawson, A. Lykov, L. L. Pan, M. Riese, A. Rollins, F. Stroh, T. Thornberry, V. Wolf, S. Woods, P. Spichtinger, J. Quaas, and O. Sourdeval, 2020: A microphysics guide to cirrus – Part 2: Climatologies of clouds and humidity from observations. *Atmospheric Chemistry and Physics*, 20 (21), 12 569–12 608, https://doi.org/10.5194/acp-20-12569-2020.

Kuebbeler, M., U. Lohmann, J. Hendricks, and B. Kärcher, 2014: Dust ice nuclei effects on cirrus clouds. *Atmospheric Chemistry and Physics*, 14 (6), 3027–3046, https://doi.org/10.5194/acp-14-3027-2014.

Kunze, M., M. Godolt, U. Langematz, J. Grenfell, A. Hamann-Reinus, and H. Rauer, 2014: Investigating the early Earth faint young Sun problem with a general circulation model. *Planetary and Space Science*, 98, 77–92, https://doi.org/10.1016/j.pss.2013.09.011.

Lacis, A. A., G. A. Schmidt, D. Rind, and R. A. Ruedy, 2010: Atmospheric CO_2: Principal Control Knob Governing Earth's Temperature. *Science*, 330 (6002), 356–359, https://doi.org/10.1126/science.1190653.

Lamquin, N., C. J. Stubenrauch, K. Gierens, U. Burkhardt, and H. Smit, 2012: A global climatology of upper-tropospheric ice supersaturation occurrence inferred from the Atmospheric Infrared Sounder calibrated by MOZAIC. *Atmospheric Chemistry and Physics*, 12 (1), 381–405, https://doi.org/10.5194/acp-12-381-2012.

Lee, D. S., D. W. Fahey, P. M. Forster, P. J. Newton, R. C. Wit, L. L. Lim, B. Owen, and R. Sausen, 2009: Aviation and global climate change in the 21st century. *Atmospheric Environment*, 43 (22), 3520–3537, https://doi.org/10.1016/j.atmosenv.2009.04.024.

Lee, D. S., G. Pitari, V. Grewe, K. Gierens, J. Penner, A. Petzold, M. Prather, U. Schumann, A. Bais, T. Berntsen, D. Iachetti, L. Lim, and R. Sausen, 2010: Transport impacts on atmosphere and climate: Aviation. *Atmospheric Environment*, 44 (37), 4678–4734, https://doi.org/10.1016/j.atmosenv.2009.06.005.

Lee, D. S., D. Fahey, A. Skowron, M. Allen, U. Burkhardt, Q. Chen, S. Doherty, S. Freeman, P. Forster, J. Fuglestvedt, A. Gettelman, R. De León, L. Lim, M. Lund, R. Millar,

B. Owen, J. Penner, G. Pitari, M. Prather, R. Sausen, and L. Wilcox, 2021: The contribution of global aviation to anthropogenic climate forcing for 2000 to 2018. *Atmospheric Environment*, 244, 117 834, https://doi.org/10.1016/j.atmosenv.2020.117834.

Lelieveld, J., C. Brühl, P. Jöckel, B. Steil, P. J. Crutzen, H. Fischer, M. A. Giorgetta, P. Hoor, M. G. Lawrence, R. Sausen, and H. Tost, 2007: Stratospheric dryness: model simulations and satellite observations. *Atmospheric Chemistry and Physics*, 7 (5), 1313–1332, https://doi.org/10.5194/acp-7-1313-2007.

Li, C., J.-S. Storch, and J. Marotzke, 2012a: Deep-ocean heat uptake and equilibrium response. *Climate Dynamics*, 40, doi: https://doi.org/10.1007/s00382-012-1350-z.

Li, J.-L. F., D. E. Waliser, W.-T. Chen, B. Guan, T. Kubar, G. Stephens, H.-Y. Ma, M. Deng, L. Donner, C. Seman, and L. Horowitz, 2012b: An observationally based evaluation of cloud ice water in CMIP3 and CMIP5 GCMs and contemporary reanalyses using contemporary satellite data. *Journal of Geophysical Research: Atmospheres*, 117 (D16), https://doi.org/10.1029/2012JD017640.

Loeb, N. G., D. R. Doelling, H. Wang, W. Su, C. Nguyen, J. G. Corbett, L. Liang, C. Mitrescu, F. G. Rose, and S. Kato, 2018: Clouds and the Earth's Radiant Energy System (CERES) Energy Balanced and Filled (EBAF) Top-of-Atmosphere (TOA) Edition-4.0 Data Product. *Journal of Climate*, 31 (2), 895 – 918, https://doi.org/10.1175/JCLI-D-17-0208.1.

Lohmann, U., and S. Ferrachat, 2010: Impact of parametric uncertainties on the present-day climate and on the anthropogenic aerosol effect. *Atmospheric Chemistry and Physics*, 10 (23), 11 373–11 383, https://doi.org/10.5194/acp-10-11373-2010.

Lohmann, U., and B. Kärcher, 2002: First interactive simulations of cirrus clouds formed by homogeneous freezing in the ECHAM general circulation model. *Journal of Geophysical Research: Atmospheres*, 107 (D10), AAC 8–1–AAC 8–13, https://doi.org/10.1029/2001JD000767.

Lohmann, U., P. Spichtinger, S. Jess, T. Peter, and H. Smit, 2008: Cirrus cloud formation and ice supersaturated regions in a global climate model. *Environmental Research Letters*, 3 (4), 045 022, https://doi.org/10.1088/1748-9326/3/4/045022.

Lohmann, U., L. Rotstayn, T. Storelvmo, A. Jones, S. Menon, J. Quaas, A. M. L. Ekman, D. Koch, and R. Ruedy, 2010: Total aerosol effect: radiative forcing or radiative flux perturbation? *Atmospheric Chemistry and Physics*, 10 (7), 3235–3246, https://doi.org/10.5194/acp-10-3235-2010.

Manabe, S., and R. T. Wetherald, 1967: Thermal Equilibrium of the Atmosphere with a Given Distribution of Relative Humidity. *Journal of Atmospheric Sciences*, 24 (3), 241 – 259, https://doi.org/10.1175/1520-0469(1967)024⟨0241:TEOTAW⟩2.0.CO;2.

Mannstein, H., A. Brömser, and L. Bugliaro, 2010: Ground-based observations for the validation of contrails and cirrus detection in satellite imagery. *Atmospheric Measurement Techniques*, 3 (3), 655–669, https://doi.org/10.5194/amt-3-655-2010.

Mannstein, H., P. Spichtinger, and K. Gierens, 2005: A note on how to avoid contrail cirrus. *Transportation Research Part D: Transport and Environment*, 10 (5), 421–426, https://doi.org/10.1016/j.trd.2005.04.012.

Markowicz, K. M., and M. Witek, 2011: Sensitivity study of global contrail radiative forcing due to particle shape. *Journal of Geophysical Research: Atmospheres*, 116 (D23), https://doi.org/10.1029/2011JD016345.

Marquart, S., M. Ponater, F. Mager, and R. Sausen, 2003: Future Development of Contrail Cover, Optical Depth, and Radiative Forcing: Impacts of Increasing Air Traffic and Climate Change. *Journal of Climate*, 16 (17), 2890 – 2904, https://doi.org/10.1175/1520-0442(2003)016⟨2890:FDOCCO⟩2.0.CO;2.

Martin, A., 2021: Determination of Radiation Couplings in Climate Change Simulations: Analysis with two different Linearization Methods. Masterthesis, Faculty of Physics and Earth Science, University of Leipzig.

Marvel, K., G. A. Schmidt, R. L. Miller, and L. S. Nazarenko, 2016: Implications for climate sensitivity from the response to individual forcings. *Nature Climate Change*, 6 (4), 386–389, https://doi.org/10.1038/nclimate2888.

Mauritsen, T., and E. Roeckner, 2020: Tuning the MPI-ESM1.2 Global Climate Model to Improve the Match With Instrumental Record Warming by Lowering Its Climate Sensitivity. *Journal of Advances in Modeling Earth Systems*, 12 (5), e2019MS002 037, https://doi.org/10.1029/2019MS002037.

Mauritsen, T., B. Stevens, E. Roeckner, T. Crueger, M. Esch, M. Giorgetta, H. Haak, J. Jungclaus, D. Klocke, D. Matei, U. Mikolajewicz, D. Notz, R. Pincus, H. Schmidt, and L. Tomassini, 2012: Tuning the climate of a global model. *Journal of Advances in Modeling Earth Systems*, 4 (3), https://doi.org/10.1029/2012MS000154.

Meraner, K., T. Mauritsen, and A. Voigt, 2013: Robust increase in equilibrium climate sensitivity under global warming. *Geophysical Research Letters*, 40 (22), 5944–5948, https://doi.org/10.1002/2013GL058118.

Meyer, R., H. Mannstein, R. Meerkötter, U. Schumann, and P. Wendling, 2002: Regional radiative forcing by line-shaped contrails derived from satellite data. *Journal of Geophysical Research: Atmospheres*, 107 (D10), ACL 17–1–ACL 17–15, https://doi.org/10.1029/2001JD000426.

Minnis, P., D. F. Young, D. P. Garber, L. Nguyen, W. L. Smith Jr., and R. Palikonda, 1998: Transformation of contrails into cirrus during SUCCESS. *Geophysical Research Letters*, 25 (8), 1157–1160, https://doi.org/10.1029/97GL03314.

Minnis, P., S. T. Bedka, D. P. Duda, K. M. Bedka, T. Chee, J. K. Ayers, R. Palikonda, D. A. Spangenberg, K. V. Khlopenkov, and R. Boeke, 2013: Linear contrail and contrail cirrus properties determined from satellite data. *Geophysical Research Letters*, 40 (12), 3220–3226, https://doi.org/10.1002/grl.50569.

Modak, A., G. Bala, L. Cao, and K. Caldeira, 2016: Why must a solar forcing be larger than a CO2 forcing to cause the same global mean surface temperature change? *Environmental Research Letters*, 11 (4), 044 013, https://doi.org/10.1088/1748-9326/11/4/044013.

Myhre, G., and F. Stordal, 2001: On the tradeoff of the solar and thermal infrared radiative impact of contrails. *Geophysical Research Letters*, 28 (16), 3119–3122, https://doi.org/10.1029/2001GL013193.

Myhre, G., D. Shindell, F.-M. Breon, W. Collins, J. Fuglestvedt, J. Huang, D. Koch, J.-F. Lamarque, D. Lee, B. Mendoza, T. Nakajima, A. Robock, G. Stephens, T. Takemura, and H. Zhang, 2013: *Anthropogenic and Natural Radiative Forcing*, book section 8, 659–740. Cambridge University Press, Cambridge, United Kingdom and New York, NY, USA, doi: https://doi.org/10.1017/CBO9781107415324.018.

Neubauer, D., S. Ferrachat, C. Siegenthaler-Le Drian, P. Stier, D. G. Partridge, I. Tegen, I. Bey, T. Stanelle, H. Kokkola, and U. Lohmann, 2019: The global aerosol–climate model ECHAM6.3–HAM2.3 – Part 2: Cloud evaluation, aerosol radiative forcing, and climate sensitivity. *Geoscientific Model Development*, 12 (8), 3609–3639, https://doi.org/10.5194/gmd-12-3609-2019.

Newinger, C., and U. Burkhardt, 2012: Sensitivity of contrail cirrus radiative forcing to air traffic scheduling. *Journal of Geophysical Research: Atmospheres*, 117 (D10), https://doi.org/10.1029/2011JD016736.

NOAA National Centers for Environmental Information, 2022: State of the Climate: Monthly Global Climate Report for Annual 2021. https://www.ncei.noaa.gov/access/monitoring/monthly-report/global/202113.

Ponater, M., 2010: Distinctive efficacies of the components contributing to total aviation climate impact. *2nd International Conference on Transport, Atmosphere and Climate (TAC-2)*, R. Sausen, P. van Velthoven, C. Brüning, and A. Blum, Eds., Deutsches Zentrum für Luft- und Raumfahrt, Forschungsbericht, Vol. 2010, 227–232, https://elib.dlr.de/65284/.

Ponater, M., M. Bickel, L. Bock, and U. Burkhardt, 2021: Towards Determining the Contrail Cirrus Efficacy. *Aerospace*, 8 (2), https://doi.org/10.3390/aerospace8020042.

Ponater, M., S. Brinkop, R. Sausen, and U. Schumann, 1996: Simulating the Global Atmospheric Response to Aircraft Water Vapour Emissions and Contrails - A First Approach Using a GCM. *Annales Geophysicae*, 14, 941–960, https://elib.dlr.de/32150/.

Ponater, M., S. Dietmüller, and R. Sausen, 2012: *Greenhouse Effect, Radiative Forcing and Climate Sensitivity*, 85–100. Springer Berlin Heidelberg, https://doi.org/10.1007/978-3-642-30183-4_6.

Ponater, M., S. Marquart, and R. Sausen, 2002: Contrails in a comprehensive global climate model: Parameterization and radiative forcing results. *Journal of Geophysical Research: Atmospheres*, 107 (D13), ACL 2–1–ACL 2–15, https://doi.org/10.1029/2001JD000429.

Ponater, M., S. Marquart, R. Sausen, and U. Schumann, 2005: On contrail climate sensitivity. *Geophysical Research Letters*, 32 (10), https://doi.org/10.1029/2005GL022580.

Prša, A., P. Harmanec, G. Torres, E. Mamajek, M. Asplund, N. Capitaine, J. Christensen-Dalsgaard, É. Depagne, M. Haberreiter, S. Hekker, J. Hilton, G. Kopp, V. Kostov, D. W. Kurtz, J. Laskar, B. D. Mason, E. F. Milone, M. Montgomery, M. Richards, W. Schmutz, J. Schou, and S. G. Stewart, 2016: NOMINAL VALUES FOR SELECTED SOLAR AND PLANETARY QUANTITIES: IAU 2015 RESOLUTION b3. *The Astronomical Journal*, 152 (2), 41, https://doi.org/10.3847/0004-6256/152/2/41.

Qiao, C. G., G. R. Wood, C. D. Lai, and D. W. Luo, 2006: Comparison of two common estimators of the ratio of the means of independent normal variables in agricultural research. *Journal of Applied Mathematics and Decision Sciences*, 2006, 078 375, https://doi.org/10.1155/JAMDS/2006/78375.

Ramaswamy, V., W. Collins, J. Haywood, J. Lean, N. Mahowald, G. Myhre, V. Naik, K. P. Shine, B. Soden, G. Stenchikov, and T. Storelvmo, 2018: Radiative Forcing of Climate: The Historical Evolution of the Radiative Forcing Concept, the Forcing Agents and their Quantification, and Applications. *Meteorological Monographs*, 59, 14.1 – 14.101, https://doi.org/10.1175/AMSMONOGRAPHS-D-19-0001.1.

Rap, A., P. M. Forster, J. M. Haywood, A. Jones, and O. Boucher, 2010: Estimating the climate impact of linear contrails using the UK Met Office climate model. *Geophysical Research Letters*, 37 (20), https://doi.org/10.1029/2010GL045161.

Rayner, N. A., D. E. Parker, E. B. Horton, C. K. Folland, L. V. Alexander, D. P. Rowell, E. C. Kent, and A. Kaplan, 2003: Global analyses of sea surface temperature, sea ice, and night marine air temperature since the late nineteenth century. *Journal of Geophysical Research: Atmospheres*, 108 (D14), https://doi.org/10.1029/2002JD002670.

Reichler, T., M. Dameris, and R. Sausen, 2003: Determining the tropopause height from gridded data. *Geophysical Research Letters*, 30 (20), https://doi.org/10.1029/2003GL018240.

Richardson, T. B., P. M. Forster, C. J. Smith, A. C. Maycock, T. Wood, T. Andrews, O. Boucher, G. Faluvegi, D. Fläschner, Ø. Hodnebrog, M. Kasoar, A. Kirkevåg, J.-F. Lamarque, J. Mülmenstädt, G. Myhre, D. Olivié, R. W. Portmann, B. H. Samset,

D. Shawki, D. Shindell, P. Stier, T. Takemura, A. Voulgarakis, and D. Watson-Parris, 2019: Efficacy of Climate Forcings in PDRMIP Models. *Journal of Geophysical Research: Atmospheres*, 124 (23), 12 824–12 844, https://doi.org/10.1029/2019JD030581.

Rieger, V. S., S. Dietmüller, and M. Ponater, 2017: Can feedback analysis be used to uncover the physical origin of climate sensitivity and efficacy differences? *Climate Dynamics*, 49 (7), 2831–2844, https://doi.org/10.1007/s00382-016-3476-x.

Righi, M., J. Hendricks, and C. G. Beer, 2021: Exploring the uncertainties in the aviation soot–cirrus effect. *Atmospheric Chemistry and Physics*, 21 (23), 17 267–17 289, https://doi.org/10.5194/acp-21-17267-2021.

Righi, M., J. Hendricks, U. Lohmann, C. G. Beer, V. Hahn, B. Heinold, R. Heller, M. Krämer, M. Ponater, C. Rolf, I. Tegen, and C. Voigt, 2020: Coupling aerosols to (cirrus) clouds in the global EMAC-MADE3 aerosol–climate model. *Geoscientific Model Development*, 13 (3), 1635–1661, https://doi.org/10.5194/gmd-13-1635-2020.

Rockel, B., E. Raschke, and B. Weyres, 1991: A parameterization of broad band radiative transfer properties of water, ice, and mixed clouds. *Contributions to atmospheric physics*, 64, 1–12.

Roeckner, E., T. Siebert, and J. Feichter, 1995: Climatic response to anthropogenic sulfate forcing simulated with a general circulation model. *Aerosol forcing of climate : Report of the Dahlem Workshop on Aerosol Forcing of Climate, Berlin 1994, April 24-29*, Wiley, BERLIN, GERMANY, Dahlem Workshop Reports : environmental sciences research report, Vol. 17, 349–362.

Roeckner, E., G. Bäuml, L. Bonaventura, R. Brokopf, M. Esch, M. Giorgetta, S. Hagemann, I. Kirchner, L. Kornblueh, E. Manzini, A. Rhodin, U. Schlese, U. Schulzweida, and A. Tompkins, 2003: The atmospheric general circulation model ECHAM 5. PART I: model description. *Max Planck Institute for Meteorology Report*, 349, http://hdl.handle.net/11858/00-001M-0000-0012-0144-5.

Roeckner, E., R. Brokopf, M. Esch, M. Giorgetta, S. Hagemann, L. Kornblueh, E. Manzini, U. Schlese, and U. Schulzweida, 2006: Sensitivity of Simulated Climate to Horizontal and Vertical Resolution in the ECHAM5 Atmosphere Model. *Journal of Climate*, 19 (16), 3771 – 3791, https://doi.org/10.1175/JCLI3824.1.

Salvi, P., P. Ceppi, and J. M. Gregory, 2021: Interpreting the Dependence of Cloud-Radiative Adjustment on Forcing Agent. *Geophysical Research Letters*, 48 (18), e2021GL093 616, https://doi.org/10.1029/2021GL093616.

Sausen, R., K. Barthel, and K. Hasselmann, 1988: Coupled ocean-atmosphere models with flux correction. *Climate Dynamics*, 2 (3), 145–163, https://doi.org/10.1007/BF01053472.

Sausen, R., I. Isaksen, V. Grewe, D. Hauglustaine, D. S. Lee, G. Myhre, M. O. Köhler, G. Pitari, U. Schumann, F. Stordal, and C. Zerefos, 2005: Aviation radiative forcing in 2000: An update on IPCC (1999). *Meteorologische Zeitschrift*, 14 (4), 555–561, https://doi.org/10.1127/0941-2948/2005/0049.

Schmidt, E., 1941: Die Entstehung von Eisnebel aus den Auspuffgasen von Flugmotoren. *Schriften der Deutschen Akademie der Luftfahrtforschung, Verlag R. Oldenburg*, 44, 1–15.

Schröder, F., B. Kärcher, C. Duroure, J. Ström, A. Petzold, J.-F. Gayet, B. Strauss, P. Wendling, and S. Borrmann, 2000: On the Transition of Contrails into Cirrus Clouds. *Journal of the Atmospheric Sciences*, 57 (4), 464 – 480, https://doi.org/10.1175/1520-0469(2000)057⟨0464:OTTOCI⟩2.0.CO;2.

Schumann, U., 1996: On conditions for contrail formation from aircraft exhausts. *Meteorologische Zeitschrift*, 5 (1), 4–23, https://doi.org/10.1127/metz/5/1996/4.

Schumann, U., 2005: Formation, properties and climatic effects of contrails. *Comptes Rendus Physique*, 6 (4), 549–565, https://doi.org/10.1016/j.crhy.2005.05.002.

Schumann, U., and K. Graf, 2013: Aviation-induced cirrus and radiation changes at diurnal timescales. *Journal of Geophysical Research: Atmospheres*, 118 (5), 2404–2421, https://doi.org/10.1002/jgrd.50184.

Schumann, U., K. Graf, H. Mannstein, and B. Mayer, 2012a: *Contrails: Visible Aviation Induced Climate Impact*, 239–257. Springer Berlin Heidelberg, https://doi.org/10.1007/978-3-642-30183-4_15.

Schumann, U., and A. J. Heymsfield, 2017: On the Life Cycle of Individual Contrails and Contrail Cirrus. *Meteorological Monographs*, 58, 3.1 – 3.24, https://doi.org/10.1175/AMSMONOGRAPHS-D-16-0005.1.

Schumann, U., and B. Mayer, 2017: Sensitivity of surface temperature to radiative forcing by contrail cirrus in a radiative-mixing model. *Atmospheric Chemistry and Physics*, 17 (22), 13 833–13 848, https://doi.org/10.5194/acp-17-13833-2017.

Schumann, U., B. Mayer, K. Graf, and H. Mannstein, 2012b: A Parametric Radiative Forcing Model for Contrail Cirrus. *Journal of Applied Meteorology and Climatology*, 51 (7), 1391 – 1406, https://doi.org/10.1175/JAMC-D-11-0242.1.

Schumann, U., J. E. Penner, Y. Chen, C. Zhou, and K. Graf, 2015: Dehydration effects from contrails in a coupled contrail–climate model. *Atmospheric Chemistry and Physics*, 15 (19), 11 179–11 199, https://doi.org/10.5194/acp-15-11179-2015.

Schumann, U., R. Baumann, D. Baumgardner, S. T. Bedka, D. P. Duda, V. Freudenthaler, J.-F. Gayet, A. J. Heymsfield, P. Minnis, M. Quante, E. Raschke, H. Schlager,

M. Vázquez-Navarro, C. Voigt, and Z. Wang, 2017: Properties of individual contrails: a compilation of observations and some comparisons. *Atmospheric Chemistry and Physics*, 17 (1), 403–438, https://doi.org/10.5194/acp-17-403-2017.

Sherwood, S. C., M. J. Webb, J. D. Annan, K. C. Armour, P. M. Forster, J. C. Hargreaves, G. Hegerl, S. A. Klein, K. D. Marvel, E. J. Rohling, M. Watanabe, T. Andrews, P. Braconnot, C. S. Bretherton, G. L. Foster, Z. Hausfather, A. S. von der Heydt, R. Knutti, T. Mauritsen, J. R. Norris, C. Proistosescu, M. Rugenstein, G. A. Schmidt, K. B. Tokarska, and M. D. Zelinka, 2020: An Assessment of Earth's Climate Sensitivity Using Multiple Lines of Evidence. *Reviews of Geophysics*, 58 (4), e2019RG000 678, https://doi.org/10.1029/2019RG000678.

Shindell, D. T., 2014: Inhomogeneous forcing and transient climate sensitivity. *Nature Climate Change*, 4 (4), 274–277, https://doi.org/10.1038/nclimate2136.

Shine, K. P., J. Cook, E. J. Highwood, and M. M. Joshi, 2003: An alternative to radiative forcing for estimating the relative importance of climate change mechanisms. *Geophysical Research Letters*, 30 (20), https://doi.org/10.1029/2003GL018141.

Smith, C. J., R. J. Kramer, G. Myhre, P. M. Forster, B. J. Soden, T. Andrews, O. Boucher, G. Faluvegi, D. Fläschner, Ø. Hodnebrog, M. Kasoar, V. Kharin, A. Kirkevåg, J.-F. Lamarque, J. Mülmenstädt, D. Olivié, T. Richardson, B. H. Samset, D. Shindell, P. Stier, T. Takemura, A. Voulgarakis, and D. Watson-Parris, 2018: Understanding Rapid Adjustments to Diverse Forcing Agents. *Geophysical Research Letters*, 45 (21), 12,023–12,031, https://doi.org/10.1029/2018GL079826.

Smith, C. J., R. J. Kramer, G. Myhre, K. Alterskjær, W. Collins, A. Sima, O. Boucher, J.-L. Dufresne, P. Nabat, M. Michou, S. Yukimoto, J. Cole, D. Paynter, H. Shiogama, F. M. O'Connor, E. Robertson, A. Wiltshire, T. Andrews, C. Hannay, R. Miller, L. Nazarenko, A. Kirkevåg, D. Olivié, S. Fiedler, A. Lewinschal, C. Mackallah, M. Dix, R. Pincus, and P. M. Forster, 2020: Effective radiative forcing and adjustments in CMIP6 models. *Atmospheric Chemistry and Physics*, 20 (16), 9591–9618, https://doi.org/10.5194/acp-20-9591-2020.

Springer, M., 1979: *The Algebra of Random Variables*. Probability and Statistics Series, Wiley.

Stecher, L., F. Winterstein, M. Dameris, P. Jöckel, M. Ponater, and M. Kunze, 2021: Slow feedbacks resulting from strongly enhanced atmospheric methane mixing ratios in a chemistry–climate model with mixed-layer ocean. *Atmospheric Chemistry and Physics*, 21 (2), 731–754, https://doi.org/10.5194/acp-21-731-2021.

Stefan, J., 1879: Über die Beziehung zwischen der Wärmestrahlung und der Temperatur. *Sitzungsberichte der Kaiserlichen Akademie der Wissenschaften in Wien*, 79, 391–428.

Stier, P., J. Feichter, S. Kinne, S. Kloster, E. Vignati, J. Wilson, L. Ganzeveld, I. Tegen, M. Werner, Y. Balkanski, M. Schulz, O. Boucher, A. Minikin, and A. Petzold, 2005: The aerosol-climate model ECHAM5-HAM. *Atmospheric Chemistry and Physics*, 5 (4), 1125–1156, https://doi.org/10.5194/acp-5-1125-2005.

Stubenrauch, C. J., W. B. Rossow, S. Kinne, S. Ackerman, G. Cesana, H. Chepfer, L. D. Girolamo, B. Getzewich, A. Guignard, A. Heidinger, B. C. Maddux, W. P. Menzel, P. Minnis, C. Pearl, S. Platnick, C. Poulsen, J. Riedi, S. Sun-Mack, A. Walther, D. Winker, S. Zeng, and G. Zhao, 2013: Assessment of Global Cloud Datasets from Satellites: Project and Database Initiated by the GEWEX Radiation Panel. *Bulletin of the American Meteorological Society*, 94 (7), 1031 – 1049, https://doi.org/10.1175/BAMS-D-12-00117.1.

Stuber, N., and P. Forster, 2007: The impact of diurnal variations of air traffic on contrail radiative forcing. *Atmospheric Chemistry and Physics*, 7 (12), 3153–3162, https://doi.org/10.5194/acp-7-3153-2007.

Stuber, N., P. Forster, G. Rädel, and K. Shine, 2006: The importance of the diurnal and annual cycle of air traffic for contrail radiative forcing. *Nature*, 441, 864–7, https://doi.org/10.1038/nature04877.

Stuber, N., R. Sausen, and M. Ponater, 2001: Stratosphere adjusted radiative forcing calculations in a comprehensive climate model. *Theoretical and Applied Climatology*, 68 (3), 125–135, https://doi.org/10.1007/s007040170041.

Sundqvist, H., 1978: A parameterization scheme for non-convective condensation including prediction of cloud water content. *Quarterly Journal of the Royal Meteorological Society*, 104 (441), 677–690, https://doi.org/10.1002/qj.49710444110.

Szopa, S., V. Naik, B. Adhikary, P. Artaxo, T. Berntsen, W. Collins, S. Fuzzi, L. Gallardo, A. Kiendler Scharr, Z. Klimont, H. Liao, N. Unger, and P. Zanis, 2021: *Short-Lived Climate Forcers*, book section 6. Cambridge University Press.

Taylor, J. W., S. L. Haslett, K. Bower, M. Flynn, I. Crawford, J. Dorsey, T. Choularton, P. J. Connolly, V. Hahn, C. Voigt, D. Sauer, R. Dupuy, J. Brito, A. Schwarzenboeck, T. Bourriane, C. Denjean, P. Rosenberg, C. Flamant, J. D. Lee, A. R. Vaughan, P. G. Hill, B. Brooks, V. Catoire, P. Knippertz, and H. Coe, 2019: Aerosol influences on low-level clouds in the West African monsoon. *Atmospheric Chemistry and Physics*, 19 (13), 8503–8522, https://doi.org/10.5194/acp-19-8503-2019.

Teoh, R., U. Schumann, A. Majumdar, and M. E. J. Stettler, 2020: Mitigating the Climate Forcing of Aircraft Contrails by Small-Scale Diversions and Technology Adoption. *Environmental Science & Technology*, 54 (5), 2941–2950, https://doi.org/10.1021/acs.est.9b05608.

Unterstrasser, S., K. Gierens, I. Sölch, and M. Lainer, 2017: Numerical simulations of homogeneously nucleated natural cirrus and contrail-cirrus. Part 1: How different are they? *Meteorologische Zeitschrift*, 26 (6), 621–642, https://doi.org/10.1127/metz/2016/0777.

Vázquez-Navarro, M., H. Mannstein, and S. Kox, 2015: Contrail life cycle and properties from 1 year of MSG/SEVIRI rapid-scan images. *Atmospheric Chemistry and Physics*, 15 (15), 8739–8749, https://doi.org/10.5194/acp-15-8739-2015.

Vazquez-Navarro, M., H. Mannstein, and B. Mayer, 2010: An automatic contrail tracking algorithm. *Atmospheric Measurement Techniques*, 3 (4), 1089–1101, https://doi.org/10.5194/amt-3-1089-2010.

Vial, J., J.-L. Dufresne, and S. Bony, 2013: On the interpretation of inter-model spread in CMIP5 climate sensitivity estimates. *Climate Dynamics*, 41 (11), 3339–3362, https://doi.org/10.1007/s00382-013-1725-9.

Voigt, C., U. Schumann, T. Jurkat, D. Schäuble, H. Schlager, A. Petzold, J.-F. Gayet, M. Krämer, J. Schneider, S. Borrmann, J. Schmale, P. Jessberger, T. Hamburger, M. Lichtenstern, M. Scheibe, C. Gourbeyre, J. Meyer, M. Kübbeler, W. Frey, H. Kalesse, T. Butler, M. G. Lawrence, F. Holzäpfel, F. Arnold, M. Wendisch, A. Döpelheuer, K. Gottschaldt, R. Baumann, M. Zöger, I. Sölch, M. Rautenhaus, and A. Dörnbrack, 2010: In-situ observations of young contrails ? overview and selected results from the CONCERT campaign. *Atmospheric Chemistry and Physics*, 10 (18), 9039–9056, https://doi.org/10.5194/acp-10-9039-2010.

Voigt, C., U. Schumann, A. Minikin, A. Abdelmonem, A. Afchine, S. Borrmann, M. Boettcher, B. Buchholz, L. Bugliaro, A. Costa, J. Curtius, M. Dollner, A. Dörnbrack, V. Dreiling, V. Ebert, A. Ehrlich, A. Fix, L. Forster, F. Frank, D. Fütterer, A. Giez, K. Graf, J.-U. Grooß, S. Groß, K. Heimerl, B. Heinold, T. Hüneke, E. Järvinen, T. Jurkat, S. Kaufmann, M. Kenntner, M. Klingebiel, T. Klimach, R. Kohl, M. Krämer, T. C. Krisna, A. Luebke, B. Mayer, S. Mertes, S. Molleker, A. Petzold, K. Pfeilsticker, M. Port, M. Rapp, P. Reutter, C. Rolf, D. Rose, D. Sauer, A. Schäfler, R. Schlage, M. Schnaiter, J. Schneider, N. Spelten, P. Spichtinger, P. Stock, A. Walser, R. Weigel, B. Weinzierl, M. Wendisch, F. Werner, H. Wernli, M. Wirth, A. Zahn, H. Ziereis, and M. Zöger, 2017: ML-CIRRUS: The Airborne Experiment on Natural Cirrus and Contrail Cirrus with the High-Altitude Long-Range Research Aircraft HALO. *Bulletin of the American Meteorological Society*, 98 (2), 271 – 288, https://doi.org/10.1175/BAMS-D-15-00213.1.

Vonder Haar, T. H., J. L. Bytheway, and J. M. Forsythe, 2012: Weather and climate analyses using improved global water vapor observations. *Geophysical Research Letters*, 39 (15), https://doi.org/10.1029/2012GL052094.

Wien, W., 1893: Eine neue Beziehung der Strahlung schwarzer Körper zum zweiten Hauptsatz der Wärmetheorie. *Verlag der Königlichen Akademie der Wissenschaften, Berlin*, Erster Halbband.

Wild, M., D. Folini, C. Schär, N. Loeb, E. G. Dutton, and G. König-Langlo, 2013: The global energy balance from a surface perspective. *Climate Dynamics*, 40 (11), 3107–3134, https://doi.org/10.1007/s00382-012-1569-8.

Wilhelm, L., K. Gierens, and S. Rohs, 2021: Weather Variability Induced Uncertainty of Contrail Radiative Forcing. *Aerospace*, 8 (11), https://doi.org/10.3390/aerospace8110332.

Wilkerson, J. T., M. Z. Jacobson, A. Malwitz, S. Balasubramanian, R. Wayson, G. Fleming, A. D. Naiman, and S. K. Lele, 2010: Analysis of emission data from global commercial aviation: 2004 and 2006. *Atmospheric Chemistry and Physics*, 10 (13), 6391–6408, https://doi.org/10.5194/acp-10-6391-2010.

Yamashita, H., F. Yin, V. Grewe, P. Jöckel, S. Matthes, B. Kern, K. Dahlmann, and C. Frömming, 2020: Newly developed aircraft routing options for air traffic simulation in the chemistry–climate model EMAC 2.53: AirTraf 2.0. *Geoscientific Model Development*, 13 (10), 4869–4890, https://doi.org/10.5194/gmd-13-4869-2020.

Zelinka, M. D., S. A. Klein, and D. L. Hartmann, 2012: Computing and Partitioning Cloud Feedbacks Using Cloud Property Histograms. Part I: Cloud Radiative Kernels. *Journal of Climate*, 25 (11), 3715 – 3735, https://doi.org/10.1175/JCLI-D-11-00248.1.

Zelinka, M. D., S. A. Klein, K. E. Taylor, T. Andrews, M. J. Webb, J. M. Gregory, and P. M. Forster, 2013: Contributions of Different Cloud Types to Feedbacks and Rapid Adjustments in CMIP5. *Journal of Climate*, 26 (14), 5007 – 5027, https://doi.org/10.1175/JCLI-D-12-00555.1.

Danksagung

An erster Stelle möchte ich mich bei meinem Betreuer Dr. Michael Ponater bedanken, der mir zu jeder Zeit fachlich als auch menschlich zur Seite stand. Sein enormes Fachwissen auf allen Gebieten der Klimawissenschaften war eine unschätzbare Hilfe und hat viel zum Gelingen dieser Arbeit beigetragen.

Mein ganz besonderer Dank gilt meinem Doktorvater Prof. Dr. Robert Sausen für das starke Interesse an meiner Arbeit, seine wertvollen Ratschläge und die stetige Unterstützung während des gesamten Projekts, insbesondere für die hilfreichen Diskussionen zur Statistik.

Des Weiteren möchte ich mich bei Prof. Dr. Mark Wenig für die Übernahme des Zweitgutachtens bedanken.

Meinem Mentor Dr. Simon Unterstrasser danke ich für seine Empfehlungen und die Begleitung meiner Arbeit.

Vielen Dank an Dr. Lisa Bock und Dr. Ulrike Burkhardt – ohne euch wäre ich vermutlich in den Tiefen von CCMod versunken. Ein großer Dank gilt außerdem Dr. Mattia Righi und Dr. Patrick Jöckel, die mir bei technischen Fragen zu EMAC immer weiterhelfen konnten. Vielen Dank an Dr. Johannes Hendricks für die unzähligen Tipps und konstruktiven Gespräche bezüglich der Wolkenparametrisierung. Ein besonderer Dank gilt Dr. Klaus Gierens für den intensiven Meinungsaustausch zur Statistik und Dr. Vanessa Rieger für die sehr hilfreichen Erläuterungen zur Feedbackanalyse.

Für die angenehme Arbeitsatmosphäre bedanke ich mich bei allen Kolleginnen und Kollegen des Instituts für Physik der Atmosphäre, insbesondere bei der Abteilung Erdsystem Modellierung. Hervorzuheben sind hier alle Mitbewohner des Kinderzimmers für das produktive Arbeitsklima und die allzeit super Stimmung. Danke an Anna für die unvergesslichen Tetrisduelle, an Laura für die spannenden Vergleiche unserer Feedbackanalysen und an Sheena, die mir bei sprachlichen Fragen stets erfolgreich weitergeholfen hat. Ein herzliches Dankeschön auch an Pooja für das Korrekturlesen meiner Arbeit und an Andreas für die unterhaltsamen Mittagspausen.

Ich danke allen meinen Freunden für ihren Rückhalt und die Aufmunterung durch viel gute Laune, sowie meinem Lieblingsverein, der mich immer wieder erfolgreich geerdet hat.

Ganz besonders möchte ich mich bei meiner Familie für die unendliche Unterstützung und Motivation bedanken – nicht zuletzt bei Pudel Fridolin für den seelischen Beistand zu jeder Stunde.